Master Thesis
Applied Physics, TU Delft

Studying the nanostructure of a-Si:H solar cell absorber layers using positron annihilation and neutron reflectometry

Probing open volume defects and hydrogen behaviour to better understand the Staebler-Wronski effect

Awital Mannheim

July 12th, 2013

Supervisor: Dr. S.W.H. Eijt
Co-supervisor: Ir. J. Melskens

MSc committee:
Dr. S.W.H. Eijt
Dr. A.H.M. Smets
Prof. Dr. E. Brück

Abstract

Hydrogenated Amorphous Silicon (a-Si:H) is a very promising solar cell material with a good potential to use in many applications, as it is cheap to produce, light-weight and flexible. However, upon prolonged exposure to light, the layers suffer from both metastable and irreversible changes (the Staebler-Wronski effect) that have a bad effect on the photoconductivity. Annealing the material up to 150-200^{o}C removes the metastable changes. The Staebler-Wronski effect has been studied for over 35 years, but the mechanisms behind it are not fully understood yet.

In this project an attempt is made to increase the understanding by examining the nanostructure of rf-PECVD produced a-Si:H samples, in particular the nanostructural evolution, as a function of annealing temperature (up to 800^{o}C) and hydrogen dilution. Positron Annihilation Spectroscopy techniques, sensitive to even the smallest vacancies, are used to study the electron environment of the open volume defects. These techniques include Doppler broadening positron annihilation spectroscopy, two-dimensional angular correlation of annihilation radiation and coincidence Doppler broadening (DB-PAS, 2D-ACAR and CDB). Neutron Reflectometry is used to study the hydrogen content as a function of film depth. Raman spectroscopy is used in addition to the annealing experiment to detect the presence of molecular hydrogen.

Clear evidence is found that dilution with hydrogen causes a broadening of the electron momentum distribution. DB-PAS and 2D-ACAR results strongly indicate that this broadening is due to a decrease in the average size of the open volume defects.

DB-PAS annealing studies clearly indicate that 3 different processes take place during annealing. Evidence has been found in this study that these processes are: (1) vacancy agglomeration, (2) H-effusion in combination with the release of vacancies at the surface and (3) crystallization of the layer.
The experiments indicated that different vacancy sizes occur. Divacancies up to multivacancies were measured upon increasing the annealing temperature up to 400^{o}C, depending on the type of sample. Some different behaviour was observed for an additional sample produced in a different manner, under high pressure conditions. For that sample, process (2) seems to run differently, and bigger maximum open spaces of up to nanosized voids ($\geqslant$1nm) were measured.

Proof for the agglomeration of vacancies is also found from the positron-electron autocorrelation function $B^{2\gamma}$ extracted from 2D-ACAR.

It is known that after the Si-H bonds start to break, between 300^{o}C and 500^{o}C, hydrogen effuses out of the sample. It is unclear what happens to the remaining H/H_2. No molecular hydrogen was found with Raman spectroscopy at 300^{o}C, 500^{o}C or 800^{o}C.

Neutron reflectometry resulted in accurate quantitative determination of hydrogen concentrations, showing that NR is a good tool to for studying a-Si:H samples, also in combination with FTIR.

The Research Centre for Photovoltaic Technologies, AIST, Tsukuba, Japan has provided “diode/triode”-samples, produced with a low deposition rate, which show a direct relation between the nanostructure parameters S&W and the external solar cell parameters, indicating that the open volume defects probed with PAS are responsible for the degree of stability of the material. A correlation has been found between the S&W parameter and the deposition rate.

This study leads to the following main recommendations. $B^{2\gamma}$ ab-initio calculations are recommended, combined with experimental determination of $B^{2\gamma}$, to get a better description of the atomic and geometrical structure of the defects. With lifetime spectroscopy the sizes of each occurring open volume defects (and perhaps their concentrations) can be determined. Together these procedures could lead to a detailed understanding of the structure of each types of open volume defect occurring in a-Si:H.

A combined NR and DB-PAS annealing studies can lead to a more detailed description of the observed 3 processes taking place during annealing. A Raman annealing study in the range of $500^{o}C \leqslant T \leqslant 750^{o}C$ is also recommended to find the temperature dependence of the breaking of Si-H bonds and crystallization, and compare this with the previous DB-PAS results.

Furthermore, a series of DB-PAS annealing experiments on several high pressure samples is desirable to study which processes are a trend for these samples, to gain a better insight in the nanostructure.

This master thesis is part of the Master Applied Physics at the faculty of Applied Sciences of the Delft University of Technology. The project was conducted at the group FAME, Fundamental Aspects of Materials and Energy, which is part of the Radiation Science and Technology Department, member of the faculty of Applied Sciences. A close collaboration was kept with the group PVMD, Photovoltaic Materials and devices, which is part of the department Sustainable Electrical Energy, member of the faculty of Electrical Engineering, Mathematics and Computer Science. The supervisor was Dr. S.W.H. Eijt (FAME), and J. Melskens has taken the role of co-supervisor.

Cover photograph: http://www.library.tudelft.nl/

Acknowledgments

Many thanks to my supervisors Stephan Eijt and Jimmy Melskens for their excellent help during this project. Both of you have been so enthusiastic and eager to help! Stephan, thank you for your encouragement throughout the project, for the elaborate discussions, for always making time for me, for your punctuality, for being patient and kind, for your detailed criticisms on the writing, next report I will surely write much better. Jimmy, thank you for providing the samples and for all your technical support, for reading through my report in the making, for sharing the broader context of this research with me, and for your surprisingly quick replies to any e-mails, in between your always busy schedule.

Many experiments were conducted during this project, taking place at many different setups. Fortunately there were a lot of people to provide technical support. Henk Schut, Ad van Well, Martijn de Boer and Charles de Boer are sincerely thanked for their dedication.

It was a pleasure to be a part of the group FAME. Memorable lunches, cake and coffee, Cluedo dinner. Thanks everyone for the gezelligheid!

I am very grateful to my parents for all the support, for thinking along with me and supporting me financially, making it possible to intensely enjoy my study time.

And my boyfriend Robbert, thank you for being so supportive and understanding during this past year!

Table of Contents

1 Introduction

Solar cells are a renewable energy technology with attractive physical properties to generate electricity in a sustainable manner in the future. The PV market is growing, but so far the fossil energy market is growing faster and the world is not getting more sustainable. Research is required in order to further reduce the production costs of solar cells and increase their efficiency.

1.1 Development of the solar cell market[1]

The solar cell types are commonly divided into three main categories, called the first, second and third generation.

All c-Si solar cell devices based on silicon wafers are termed first-generation. These are well-established types of solar cells that reach good conversion efficiencies of 20% in modules, but that are relatively expensive to produce, because the c-Si absorber layer needs to be very pure, which is achieved with the Czochralski process. During this process the silicon is melted. The melting point lies at 1414^{o}C, making the production a costly process. Currently c-Si solar cells dominate the photovoltaic market, with a market share of 80-90% in 2011.

Almost all the rest of the PV-market is made up by the thin film solar cell technologies, which is a second-generation technology. The main types are CdTe (cadmium telluride), CIGS (copper indium gallium selenide) and a-Si:H (hydrogenated amorphous silicon), named after the absorber materials used in these cells. These devices are cheaper in production and can be used in more applications, because of their light weight and flexibility. However, the conversion efficiencies currently obtained are not as high as those for c-Si leading to less electro power/m^2 of solar cells. Another example of a second-generation technology is a solar concentrator, where solar light is concentrated on a high-efficiency solar cell surface using optics.

The second-generation technologies are single junctions, meaning that they contain one absorber layer, and multijunctions, with multiple absorber layers on top of each other. The a-Si:H absorber layer is mostly used in a triple junction, on top of two µc-Si:H-layers (microcrystalline silicon). The theoretical maximum efficiencies for a single junction solar cell is limited to 33% (see section 2.1). The first generation devices are close to their maximum for laboratory samples, and for the second generation this is not the case. With the promise of cheapness and high efficiency in mind the second generation is researched intensively.

Smart, third generation, technologies are not ready to be on the market yet. In general, the aim with these cells is to circumvent the maximum efficiency problem, most of the time by increasing the quantum efficiency of the cell (the generation of multiple electron-hole pairs from one incoming photon). Some other third generation solar cell types include non-semiconductor solar cells (such as organic cells and biomimetic solar cells) and quantum dot solar cells (which have tuneable bandgaps).

1.2 a-Si:H absorber layers

1.2.1 c-Si versus a-Si:H

As the name says, a-Si:H is an amorphous solid consisting of silicon atoms, that is hydrogenated. The long-range order lacks and the material is not in its minimum energy configuration. The Si-Si bond lengths vary throughout the solid, and there are intrinsic defects called dangling bonds (a threefold coordinated Si-atom) and floating bonds (a fivefold coordinated Si-atom).[2] The dangling bonds are known to act as trapping centres for photoexcited electrons and holes. The hydrogen atoms can passivate many of the natural defects, thereby reducing the intrinsic dangling bond density from $10^{20}cm^{-3}$ to around 10^{15}-$10^{16}cm^{-3}$.[3]

Figure 1-1 shows the schematic representation of the atomic structure of c-Si, and a-Si:H, illustrating the defects and varying bond lengths. This variable bond length makes that the energy gap $\Delta E = E_c - E_v$ between the conduction and valence band is less well defined, causing tail states. Therefore a-Si has a direct band gap, which leads to a high absorption coefficient, reducing the required thickness for the absorber layer tremendously from 400µm for c-Si to 400nm for a-Si.

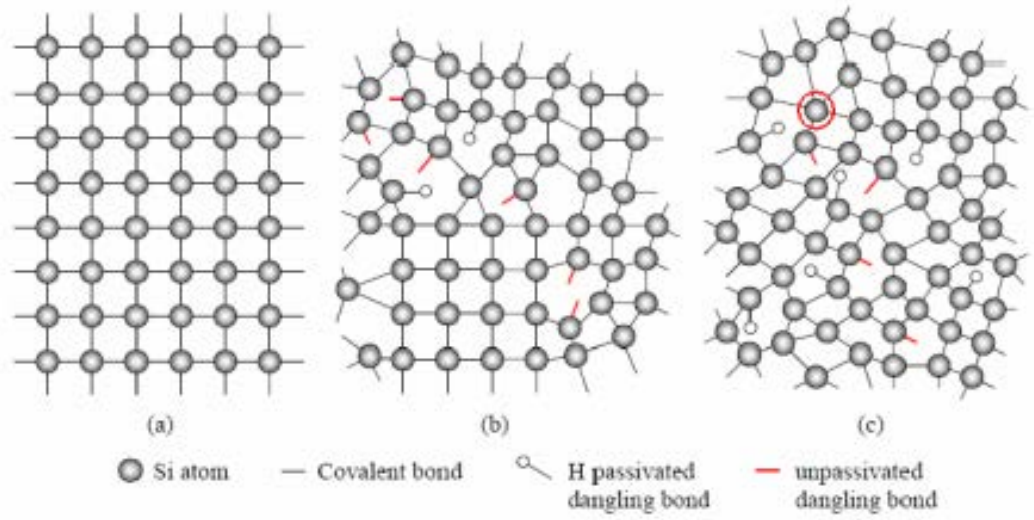

Figure 1-1.[4] 2D-schematic atomic configurations of (a) single crystal silicon, (b) microcrystalline silicon, (c) hydrogenated amorphous silicon.

1.2.2 Promises and issues of a-Si:H[4]

In principle a-Si:H is a very promising solar cell material. The layers are much cheaper in production, little material is needed, they can be produced in large areas and their thicknesses allows for more applications (light-weight and flexible). However there are some issues that are performance and production related. The following issues can be mentioned:[4]

With respect to the absorber layer:

1. Increasing the conversion efficiency of the solar light.
2. Reducing the light-induced degradation, called the Staebler-Wronski effect
3. Increase of the deposition speed to 6.0 nm/min, while avoiding an worsening of the SWE.

With respect to the other solar cell components

4. The choice of mass production technology, such that both the deposition of the absorber layer and the other production steps can be quick and cheap
5. Lowering of material costs, for example of the substrate

In this study we aim to learn more about the nanostructure of the a-Si:H absorber layer, in order to get a better understanding of the Staebler-Wronski effect, which plays a key role in the second and third issue.

1.3 Models for the a-Si:H nanostructure and the Staebler-Wronski effect[5]

The Staebler-Wronski effect[7] is the degradation of the photoconductivity of the a-Si:H layer as a result of prolonged illumination. The degradation reduces the solar cells efficiency. The effect was found by Staebler and Wronski in 1977[6]. They also discovered that at least part of the photoconductivity decrease is reversible by annealing the material at a temperature of $T \geq 150^{o}C$.

1.3.1 Dangling-bond models

Now, after over 35 years of research, the mechanisms behind the reversible changes are still not fully understood. Several models for explaining the metastable light-induced degradation were proposed, among which the most popular model by Stutzmann et al. in 1985[7]. Their model is referred to as the weak bond-breaking model. We describe their model here.

It is suggested that the dangling bond defects are the main trapping centres where electron-hole recombination occurs. Dangling bonds can occur with three charges: D^{+}, D^{0} and D^{-} are the positive, neutral and negative dangling bond defects.

Some dangling bonds are already created during deposition and due to illumination new dangling bonds are created. According to the model, this happens by recombination of electron-hole pairs in the neighbourhood of a weak Si-Si bond. The recombination delivers the energy to break the bond. Enough energy is left for a hydrogen atom to move in between the Si-atoms and prevent the bond from being renewed.

Some other models were proposed as well, such as the H collision model, by Branz (1999)[8], or the defect-pool model, by Powell and Deane[9]. These models have in common that the explanation is based solely on the creation of dangling bonds. However, extensive evidence has been found that does not agree with models with dangling bonds in a continuous random network, most of which is based on the heterogeneity of a-Si:H:

- There is a lack of spatial correlation between the defects and hydrogen.[10]
- There are ordered regions in the material containing less hydrogen, surrounded by amorphous regions with more hydrogen.[5]
- The light-induced dangling bonds are found to happen at different locations than deposition-related dangling bonds. [5]
- Light exposure not only produces defects, but also produces larger scale structural changes in the Si-network of the material.[5]
- The defect-pool model is proven incorrect.[11]

The numerous proof for the heterogeneous nature of the nanostructure in a-Si:H absorber layers makes it unlikely that only point defects should be taken into account in a model explaining the SWE.

1.3.2 Vacancy defects

All in all it appears that models based on dangling bonds as the dominant defect are a too simple description of the structure of a-Si:H. There may not be a large-scale ordered structure as in crystals, but this does not imply that the network is completely random.[12]

By all means, it seems certain that hydrogen plays a crucial role in the reversibility of the light-induced degradation, given the low annealing temperature of only $T \geq 150^{o}C$, when hydrogen atoms are mobile in a-Si:H. According to several studies, most of the hydrogen bonds in a cluster with 4-7 hydrogen atoms.[13] Divacancies, where two adjacent Si-atoms are missing in the network, have been proposed as a possible configuration fitting with these H-clusters. In Figure 1-2, the schematic structure of a monovacancy and divacancy are shown. Monovacancies do not occur in a-Si:H, since they are not stable at room temperature.

Arguments to use vacancies in the description of the nanostructure are also provided by Zafar and Schiff[14] in 1989. They argued that a reservoir of H-atoms must exist in the material, since annealing to about 200^{o}C restores part of the degradation. They found from ESR (electron spin resonance) measurements that most of the H-atoms are paired. Subsequently, Branz and Zhang[15] proposed that mono- and multivacancies may serve as the reservoir of the electrically inactive paired H-atoms; and moreover that the vacancies serve as the metastability sites in a-Si:H.

Recently it was suggested by Smets et al. that a nanostructural model where not-fully H-passivated divacancies are the dominant defect states in a-Si:H would better suit the experimental findings[13]. It was found from DB-PAS (Doppler broadening positron annihilation spectroscopy) annealing studies that the di-vacancies present in the material agglomerate to larger vacancies with increasing temperature[7]. Furthermore, while three charged defect states are expected for models with only dangling-bond defects, FTPS (Fourier transform photocurrent spectroscopy) measurements give evidence for a fourth defect state.[16] Also, from FTIR (Fourier transform infrared) spectroscopy it was found that for hydrogen concentrations below ~14at.% the dominant open volume deficiency is on average a divacancy, and above ~14at.% it is on average a larger open volume defect, called a nanosized void.[13]

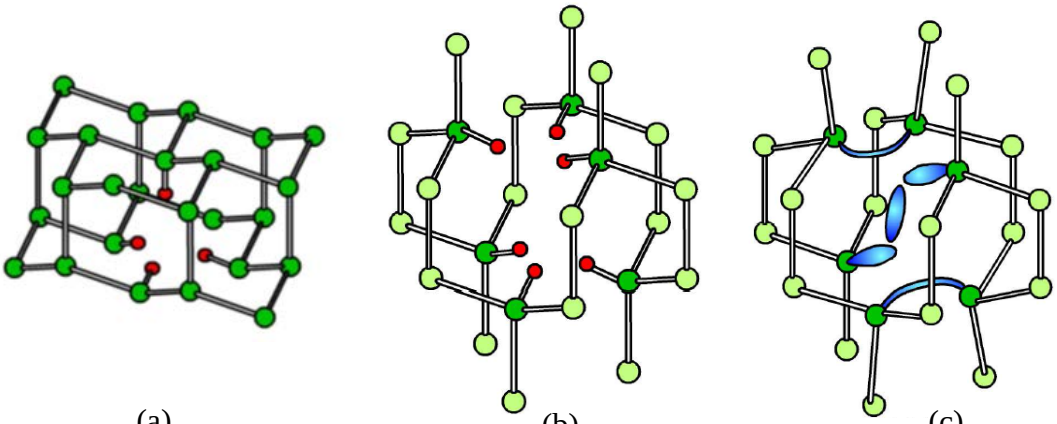

Figure 1-2. Schematic structure (adapted from [17][18]) of a monovacancy, (a), and two divacancies, (b) and (c), for a fourfold-coordinated material. The Si-atoms are green and the hydrogen atoms are red. (a) and (b) show vacancies that are completely hydrogen-passivated. It can also happen that one or more hydrogen atoms are missing. In that case, dangling bonds are left behind, or new covalent bonds are formed. (c) shows a completely unpassivated vacancy.

1.4 The role of hydrogen

1.4.1 Where is hydrogen located inside a-Si:H?

It is clear that hydrogen plays a crucial role in the Staebler-Wronski effect, based on the low required annealing temperature for restoration of the material ($T \geq 150^{o}C$). At this temperature the hydrogen is known to be mobile, while silicon only becomes mobile at temperatures above 1000°C. In order to provide a nanostructural explanation for the SWE, it is important to know in what quantities hydrogen is present in the material and how the hydrogen is bonded.

NMR studies have revealed that on average the hydrogen concentration for good-quality rf-PECVD prepared a-Si:H is about 10 at.%. depending on the hydrogen to silane dilution ratio. About 4 at.% is bonded to silicon in isolated Si-H bonds, and about 1 at.% is bonded as H_2, and is located interstitially or in voids. The rest of the hydrogen forms clusters of about 6-8 Si-H bonds, most likely at the internal surfaces of di- or tri-vacancies.[5] (e.g. Figure 1-2a)

1.4.2 H-effusion measurements

A good tool to find out more about the material structure is by annealing the material and monitoring the changes. For a-Si:H the role of hydrogen has been studied extensively by means of H-effusion experiments. Some main findings are described here. It was found that the microstructure of a-Si:H depends a lot on the deposition technique/conditions used. An example of this is shown in Figure 1-3, which is taken from Beyer[19]. The samples shown are all grown using rf-PECVD, only the substrate temperature was varied. For the lower substrate temperatures, two effusion peaks can be observed: the so-called low temperature (LT) peak at around 400°C and the high temperature (HT) peak at around 600°C.

The low temperature peak is known to only occur for a high hydrogen concentration of more than 15 at.%. The LT peak has been associated with hydrogen moving molecularly through the film[19]. The hydrogen comes from simultaneously breaking of two Si-H bonds (a new Si-Si bond is formed). It is known that the LT peak temperature does not depend on the film thickness, indicating that diffusion through the film is not the rate-limiting process here. The HT peak temperature on the other hand does depend on film thickness, and has been associated with atomic hydrogen movement through the film. The source of the additional hydrogen is not known, but could be molecular hydrogen still present in the layer above 400°C.

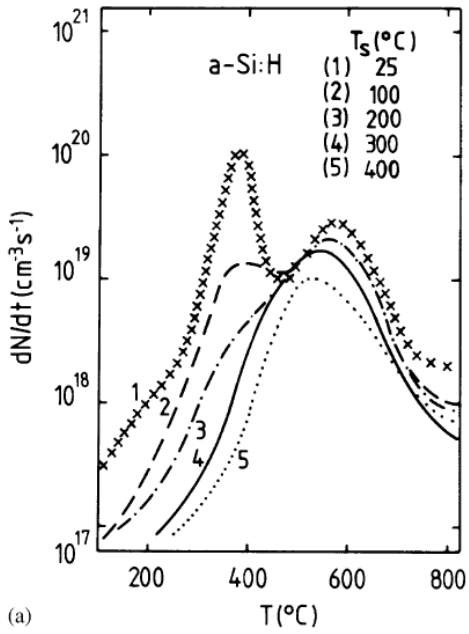

Figure 1-3.[19] H-effusion rate as a function of the annealing temperature. Heating with 20 C/min. a-Si:H samples were rf-plasma grown, various substrate temperatures during deposition.

1.5 Project description

Motivation

With the increasing world energy demand, new resources are necessary. Solar energy has the capability to satisfy all electricity demand, provided that good solar cell technologies become available. a-Si:H absorber layers are cheap to produce and are a good candidate to be used in tandem (multilayer) cells as well as in single junctions.

However these a-Si:H layers suffer from metastable defects due to light-induced degradation. A better knowledge of the nanostructural changes that lay behind the Staebler-Wronski effect is needed in order to reduce this effect. In order to gain better understanding of these nanostructural changes, the nature and depth-dependence of the defects and the distribution and behaviour of hydrogen are studied here by means of positron and neutron material characterization techniques.

Samples

More specifically, the effect of altering the hydrogen dilution for rf-PECVD deposited films, and the effect of stepwise annealing these films, on the nanostructural changes are studied by using the material characterization techniques positron annihilation spectroscopy, neutron reflectometry, and lastly Raman spectroscopy, as an auxiliary technique.

Furthermore, some additional a-Si:H layers that recently proved to have desirable solar cell properties are studied using PAS. There is the rf-PECVD produced high-pressure sample, deposited by Marinus Fischer of the PVMD group of Miro Zeman, that shows a high open-circuit voltage. And there are "diode/triode"-deposited samples produced by Dr. K. Saito and Dr. T. Matsui at AIST, Tsukuba, Japan. These layers showed high initial and stabilized solar cell efficiencies.

PAS techniques

In positron annihilation spectroscopy, positrons are injected into the material, which, depending on their initial energy results in annihilation with an electron at a certain depth, preferably at defect sites that are neutrally or negatively charged. Gamma rays are emitted as a result, which can be detected and used to find out material properties. By measuring the energy (with DB-PAS and coincidence Doppler broadening (CDB)) or the mutual angle (two-dimensional angular correlation of annihilation radiation (2D-ACAR)) of the emitted γ-rays, the electron momenta of the annihilated electrons can be deduced. In this thesis three types of PAS techniques are used to observe the electron momentum distributions, all available at the Reactor Institute Delft. 2D-ACAR has a very high resolution, DB-PAS is fast and therefore allows for depth-sensitive measurements and with CDB a low background is achieved, allowing for studying the core electrons.

Positrons are attractive to use when studying defects, because these particles are attracted to open volumes in the material that are neutral or negatively charged. This makes positrons a sensitive probe for studying the electronic structure near open volume defects, as a function of depth. The implantation depths that can be reached by the positrons make PAS very suitable to study 300 nm layers, the typical a-Si:H layer thickness. The non-destructive nature of PAS allows for multiple measurements on the same sample, enabling in-situ studies as a function of temperature. While TEM (transmission electron microscopy) and SAXS (small angle x-ray scattering) can also be used to study defects, they are only sensitive for defects > 2nm. FTPS is also a complementary technique to study defects, that lacks the capability to directly measure depth-dependencies. FTPS is very suitable to study electrically active defects in the band gap.

Neutron reflectivity and Raman spectroscopy

In neutron reflectivity (NR) a neutron beam is shone onto the material, at a very small angle, upon which reflection occurs from each interface in the material. The reflectivity is very different for different atoms or even isotopes. The contrast between Si atoms and H atoms is very good. This makes NR a suitable non-destructive technique to determine the material contents as a function of depth.

In Raman spectroscopy a laser beam is scattered. This scattering induces molecular and lattice vibrations in a solid material. From the energy loss of the scattered photons to the vibrations, the covalent bonds in the material can be detected, such as in this case Si-Si and Si-H bonds, from the collected spectrum of Raman scattered light.

Experimental goals

DB-PAS is used to study the evolution of the presence and size of open volume defects as a function of depth in the a-Si:H absorber layer and as a function of

temperature, for different hydrogen dilutions and for the high pressure sample and for the dense diode/triode layers. This is done in order to find the effect of the hydrogen dilution on the nanostructure and nanostructure evolution.

2D-ACAR spectroscopy is used to study the change in the defects spatial structure as a function of the hydrogen to silane ratio R during deposition, and also as a function of the annealing temperature T. The latter measurements are combined with CDB measurements to measure the momentum distribution with low background.

With neutron reflectometry we do a first investigation on the possibilities for measuring the hydrogen content of a-Si:H films. The main questions addressed are: are there any differences measurable for different samples, using neutrons? How accurately can the hydrogen concentration be determined? Is the hydrogen distributed homogeneously along the film depth?

Finally, Raman spectroscopy is used for films at various annealing temperatures, mainly to see whether molecular hydrogen is present in the film, and also to determine the degree of crystallinity at various temperatures.

To summarize the main questions:

1. Using positron annihilation, what kind of defects are dominant in the a-Si:H layers? And how does this vary with depth, temperature and deposition condition?
2. What is the role of hydrogen in the material, where does it go, also after increasing the temperature?

In order to address these questions, PAS and NR were used as the main techniques.

Outlook

In chapter 2, the theoretical background is given, along with a short description of the working of the solar cell. Chapter 3 describes the measurement setups and data-handling, and describes the sample sets and what they were used for. In chapter 4 the results are presented and discussed and in chapter 5 the main conclusions and recommendations are given for further studies.

2 Theory

In this chapter the physical principles are described behind the three measurement techniques used. For each technique we also describe how it can be used for studying defects and the presence of hydrogen. In section 2.2 positron annihilation spectroscopy is discussed, in section 2.3 neutron reflectometry and in section 2.4 Raman spectrometry. But first a basic model of the solar cell is introduced in section 2.1, along with some of its important characterization parameters.

2.1 Solar cells

In this section we shortly look at the working principle of the solar cells in subsection 2.1.1. Then, in subsection 2.1.2 some important definitions are given that are generally used to characterize the performance of a solar cell.

2.1.1 Working principle of the a-Si:H solar cell

The a-Si:H solar cell has a p-i-n structure. Incoming solar light is absorbed in the intrinsic layer (the i-layer). Hereby electron-hole pairs are created, caused by the photovoltaic effect. The electron-hole pairs are separated due to the internal electric field that is caused by the p- and n-doped layers in the junction. The electrons drift towards the n-layer and the holes towards the p-layer.

In principle all the free electrons that arrive at the n-layer contribute to the generated current, except for some internal losses at the electric circuit of the solar cell itself. These losses are modelled by two resistances. The series resistance R_S arises from the resistance between the front surface to the electrical contacts and shunt resistance R_{SH} arises from leakage currents, for example at the edges of the devices. A schematic circuit of the solar cell that includes these resistances is shown in Figure 2-1.

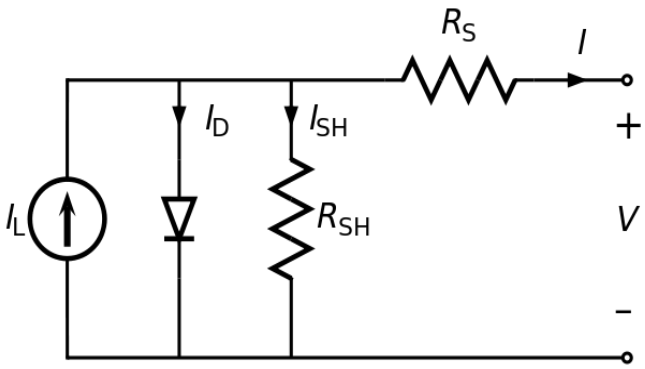

Figure 2-1. Schematic circuit of the solar cell including the internal resistances.[20]

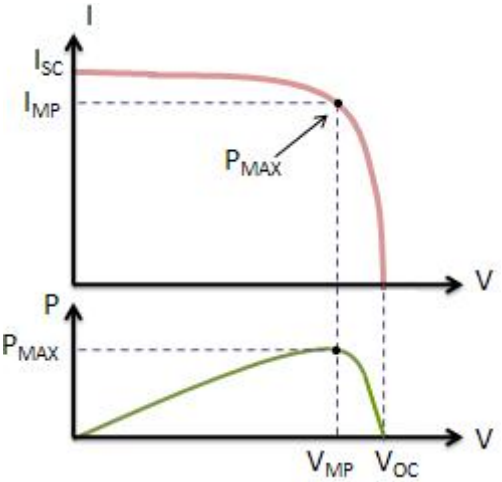

Figure 2-2. A typical solar cell IV-curve, illustrating the definitions of I_{SC}, V_{OC} and P_{max}.[21]

A typical solar cell IV-curve is given in Figure 2-2. In this figure I_{mp} and V_{mp} are the current and the voltage at the maximum power point P_{max}. The intersections with the

I- and V-axes are defined as I_{SC} and V_{OC}. The short-circuit current I_{SC} is the current generated when a perfectly lossless external load is connected and V_{OC} is the open circuit voltage when no external load is connected.

2.1.2 Measuring the performance of solar cells

An important characterization parameter for solar cells is the fill factor. This factor quantifies how much power is lost internally - at the series and shunt resistances. It is defined as:

$$FF = \frac{P_{\max}}{V_{OC} \cdot I_{SC}} \tag{2.1}$$

When FF=1, the IV-curve would be square-shaped. In practice the fill factor lies between 0.50-0.82.

The efficiency of a solar cell is defined as the ratio of the power of the incoming solar light P_{solar} to the power generated by the solar cell, after internal losses:

$$\eta = \frac{P_{\max}}{P_{solar}} \tag{2.2}$$

In the efficiency parameter η it is reflected how good the solar cell works as a whole. The fill factor shows whether or not a big part of the current generated is lost through internal resistances. These characterization parameters are measured under the Standard Test Conditions for solar cells.

Theoretical maximum for the efficiency

Maximum efficiency for any system that converts solar light into work is computed by using

$$\eta_{photoconvert} = \frac{W}{E_{sun}} \cdot \eta_{Carnot} = \frac{\sigma_S T_S^4 - \sigma_S T_C^4}{\sigma_S T_S^4} \cdot (1 - \frac{T_A}{T_C}) \tag{2.3}$$

Here η_{Carnot} is the maximum Carnot efficiency, which is achieved for an isoentropic Carnot engine. σ_S is Stefan's constant, σT^4 is the radiation for a black body, T_A is the

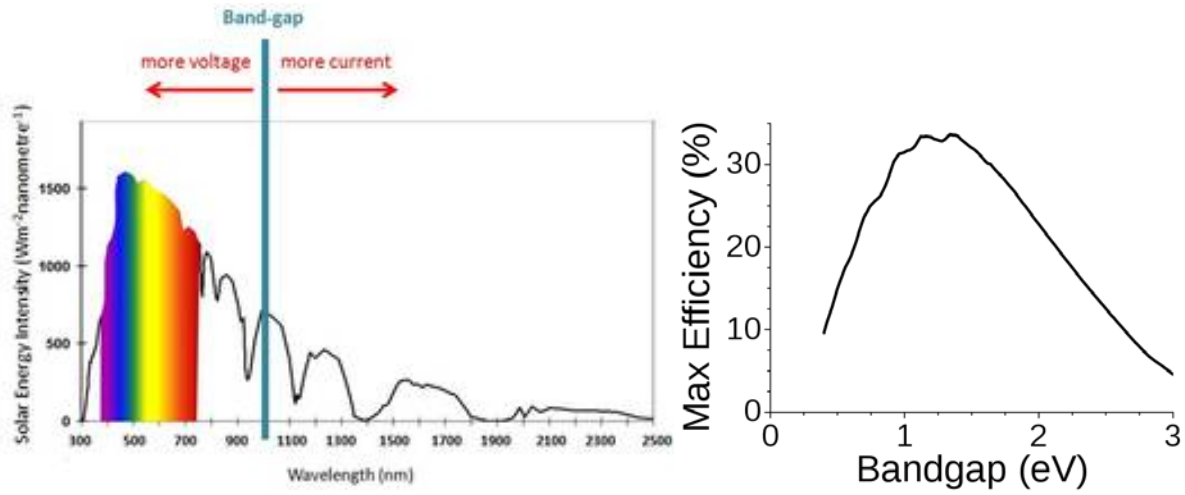

Figure 2-3 (a) The Air Mass 1.5 solar spectrum, illustrating the trade-off between voltage and current for different band gaps.[22] (b) The Shockley-Queisser limit, that is the maximum PV solar cell efficiency as a function of the band gap, calculated for the AM 1.5 spectrum.[23]

ambient temperature, T_C is the systems cell temperature and T_S is the sun temperature at the surface. For a sun temperature of 5760K and an ambient temperature of 300K, $\eta_{photonconvert}$ has a maximum of 85% for a system cell temperature of 2470K (extremely high indeed).

When we use a p-n junction to convert solar light into electrical power, the maximum efficiency is much lower than that. The efficiency is dependent on the band gap of the material. An electron-hole pair is only created when the energy of the incoming photon E_{ph} exceeds the band gap energy E_G. When $E_{ph} \geq E_G$, most photons only donate an energy of E_G to the electrons, and the rest of the energy is dissipated as heat. Therefore, the higher the bandgap is, the larger part of the photon energy can be used, increasing the open circuit voltage V_{OC}. And the smaller the bandgap is, the larger part of the solar spectrum can be used, increasing the short circuit current I_{SC} (Figure 2-3a). Based on the AM 1.5 spectrum the maximum theoretical efficiency is calculated for each bandgap by Shockley and Queisser[24]. The resulting curve is called the Shockley-Queisser limit (Figure 2-3b). For a-Si:H the bandgap is around 1.7 eV. This corresponds to a theoretical maximum efficiency of 31%. To compare, for c-Si, $E_G = 1.1eV$ and $\eta_{\max} = 29\%$. The maximum efficiency for any bandgap is 33.7%.

The Shockley-Queisser limit can be exceeded by using multiple layers on top of each other that have different bandgaps, the highest bandgap material on top. In this manner the solar light can be converted at a higher efficiency, combining the best of all properties. The a-Si:H absorber layer is also a candidate to use in a multilayer solar cell.

2.2 Positron annihilation to study materials

In this section it is explained which interactions take place between a positron and a material that result in a two-photon positron annihilation, take place. Various types of information that are contained in PAS measurements are described here, such as the momentum distribution, the S- and W-parameter and the positron-electron autocorrelation function $B^{2\gamma}$.

2.2.1 Principle of positron annihilation[25],[26]

When an energetic positron enters a dense material, it travels through the material while being slowed down because of inelastic collisions with electrons and phonons.

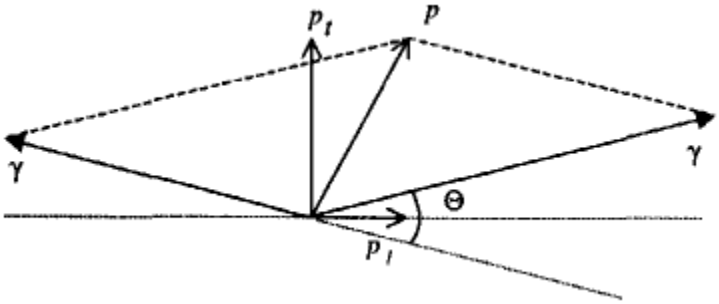

Figure 2-4. Positron annihilation. The relation between angle and momenta in a vector diagram.[2]

After the positron has been thermalized, it diffuses through the material, meanwhile mainly governed by Coulomb interactions with the electrons and ion cores in the material, until it annihilates with an electron. Most of the time, two gamma photons are produced as a result of the annihilation, due to the conservation laws of charge, momentum and energy.
In the simplified case where the positron-electron pair is at rest in the lab-frame at the moment of annihilation, the two photons are emitted in exact opposite directions and with an energy of $m_0c^2 = 511keV$ each. If the positron-electron pair has a momentum $\vec{p}$ relative to the laboratory frame, the two photons are emitted with energies shifted from 511keV due to the Doppler effect for electromagnetic radiation. The angles will also deviate slightly from 180°, because of conservation of momentum and energy, as illustrated in Figure 2-4.
For small momenta $\vec{p}$, the angle shift from 180° is given by:

$$\theta = \frac{p_t}{m_0 c} \tag{2.4}$$

The energy (Doppler) shift ΔE is given by:

$$\Delta E = \frac{cp_l}{2} \tag{2.5}$$

By measuring the angle or the energy shift, the momentum of the positron-electron pair can be retrieved.

Depth profile
The depth that the positron reaches before annihilation takes place, can be described by a probability distribution. This so-called positron implantation profile $P(E,z)$ has been determined from Monte-Carlo calculations[26]. The shape of the implantation profile resembles a Makhovian probability distribution according to

$$P(z,E) = \frac{mz^{m-1}}{z_0^m} e^{[-z/z_0]^m} \tag{2.6}$$

Where E is the energy of the incident positrons, *m* a shape parameter (*m*=2.0±0.1) and z_0 is related to the mean implantation depth $\bar{z}$, which is given below. The mean positron implantation depth $\bar{z}$ is assumed to be dependent on the initial positron energy $E[keV]$ and on the material density $\rho[g/cm^3]$ in the following way:

$$\bar{z} = \frac{\alpha}{\rho} E^n \tag{2.7}$$

Here α and n are usually treated as constants. Their empirical values are n=1.62±0.05 and α =4.0±0.3μg cm^{-2}keV$^{-1.62}$. This property of positrons, where the depth that is reached by the positrons depends on the initial kinetic energy of positrons entering a material, allows for depth-sensitive experiments on the materials to be studied.

After thermalization
There are several places in the material where the positron can end up after thermalization. We describe them here.
Delocalized positron state: The positron can thermalize in a nearly delocalized state. In that case, the positron wave function has a nearly periodic (Bloch-like) shape. The positron then diffuses around until it annihilates with an electron, when their wave functions overlap.

Defect trapping: The positron is trapped in some defect. Now the wave function becomes strongly localized. The positron then stays inside the trap until it annihilates with an electron.
Diffusion back to the surface: When the positron is implanted close to the surface, which mainly happens at low implantation energies, it can diffuse back towards the surface. Once arrived near the surface, there are several states for them to go to, such as trapping in surface or near-surface defects, or re-emission as a free positron or emission while forming a free positronium atom.[47]

Momentum distribution
Due to the energy shift of formula (2.5), the 511 keV spectral line that appears due to annihilation will be broadened and will be a distribution instead, as depicted in figure 8.

Since the positron has already been thermalized, its kinetic energy at the instant of annihilation is negligibly small compared to the electron's kinetic energy. Therefore the electron momentum distribution can be determined by measuring the energy (or angle) of the annihilation photons. Measuring the angle can even give two-dimensional information about the momentum distribution.

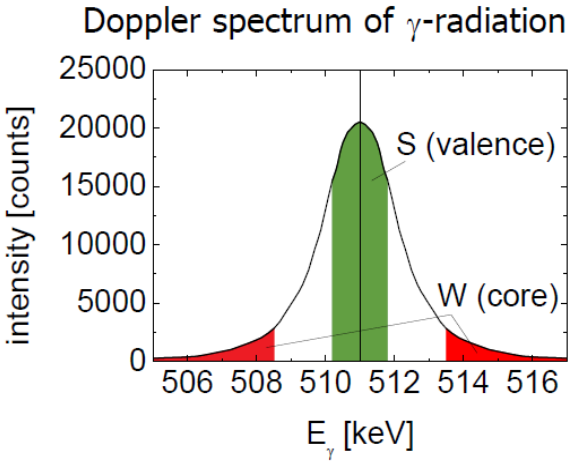

Figure 2-5. Doppler broadened momentum distribution from PAS illustrating the S- and W-parameter which denote the low and high-momentum electrons respectively.[27]

The example in figure 2-5 shows an example of a momentum distribution, together with the energy intervals used to determine the values of the S and W parameters.

What information can be extracted from the momentum distribution?
Due to the absence of positively charged nuclei, the positron is attracted to open volume defects in the material. Therefore the positron will annihilate relatively often after being trapped in a defect. This makes positron annihilation spectroscopy (PAS) a very suitable technique to study these defects. The positron can either annihilate with a core electron, whose wave function is mainly confined in a small area near the nucleus, or with a valence electron, whose wave function is also situated at the outer edges of the atom. The wave functions of the valence electrons near open volumes are affected by and contain information about the nature of the particular defect. The core electron wave functions are hardly affected by the surrounding material structure, therefore they can help identifying the chemical elements in the neighbourhood of the

open volume defects. A trapped positron can annihilate with both a valence or a core electron, but will more likely annihilate with a valence electron, since their wavefunctions have more overlap as they extend further into the open space of the defect (or into the interstitial space). By correctly interpreting the measured electron distribution in principle it should be possible to determine both the nature of the open volume defects, such as their sizes, and the surrounding atoms near the defects. In order to do this most quantitatively, experimental results should be compared to ab-initio calculations of the positron-electron momentum distribution for the defect.

Another measurable parameter is the lifetime of the positron. When the electron density is low, for example near an open volume defect, the electron and positron can form positronium (Ps). The lifetime of the positron increases with the size of the open volume, up to a size of 5Å, due to the lack of electron density in the bigger volumes.[28]

S&W parameter: definitions[29]

Positron annihilation can take place with all electrons inside the material, core electrons as well as valence electrons. A common way to describe the measured momentum distribution is by summarizing it into two parameters, namely the line shape parameter S and the wing parameter W (Figure 2-5).

Their definitions are given by:

$$S = \frac{1}{T}\int_{E_0-E_S}^{E_0+E_S} N \cdot dE \tag{2.8}$$

$$W = \frac{1}{T}\int_{E_0-E_2}^{E_0-E_1} N \cdot dE + \frac{1}{T}\int_{E_0+E_1}^{E_0+E_2} N \cdot dE \tag{2.9}$$

Where in our case, $E_S = 0.809keV$, $E_1 = 2.564keV$ and $E_2 = 6.614keV$, corresponding to momenta of $|p_l| \le 3.5 \cdot 10^{-3} m_0 c$ for S and $10 \cdot 10^{-3} m_0 c \le |p_l| \le 26 \cdot 10^{-3} m_0 c$ for W. T is the total number of counts/coincidence events collected.

The statistical errors of S and W are given by error propagation formula's as follows.

$$\Delta S = \sqrt{\frac{S(1-S)}{T}} \tag{2.10}$$

$$\Delta W = \sqrt{\frac{W(1-W)}{T}} \tag{2.11}$$

S&W parameter: interpretation[29],[45]

In Figure 2-5 the areas corresponding to the S- and W-parameter contributions are indicated. The low energy (valence) electrons lead to small energy shifts. They contribute the most to S. The core electrons, which have high energies, lead to high energy shifts from the 511 keV spectral line and contribute most to W. As we saw before, the open volume defects in the material serve as trapping centres for the positrons. Inside these defects a smaller fraction of the positrons annihilate with the core electrons. Instead, relatively more annihilations with the low momentum valence electrons occur. This results in a narrower momentum distribution: S will increase and W will decrease. The S-parameter increases because when the positron is trapped

inside the open volume, there is less overlap between the wave function of the positron and that of the core electron. The bigger the open volume is, the more the overlap decreases, and the higher the S-parameter will be.[31] Inside very large open volume (voids), positronium is formed.[32]

To compare data obtained on different set-ups, the S- and W-values are divided by the values of a c-Si reference sample. The relation between S and the open volume deficiency has been quantified for c-Si/a-Si:H by for example van Veen et. al, in 1995. Based on those results, we use the approximate boundaries for the different types of open volume defects that are given in Table 2-1.

Table 2-1. Approximate boundaries for the different types of open volume defects.

S	Open volume deficiency
~1.030-1.038	Divacancies
1.038-1.061	Multivacancies
>1.061	Voids

However, some care must be taken in interpreting these parameters. The boundaries between different defect types are only indications, and the identification only holds assuming saturated trapping of the positrons. For example, when only 50% of the positrons would trap in multivacancies characterized by S=1.050 and 50% would annihilate in the defect-free material, S would be 1.025 instead of 1.050. A typical defect concentration for saturated trapping inside a-Si:H is on the order of 10^{18} defects/cm^3. (See also section 4.1). Even if saturated trapping occurs, several defect types might be present in the material, making S a number somewhere in between the characteristic numbers for the defect types.

2.2.2 Autocorrelation function[33]

In this subsection the definition of the positron-electron autocorrelation function is given, the shape of the curve is explained, including the positions of the zero crossings. It will be shown why this is a desirable function, and how it can be used to estimate the positron binding energy.

The autocorrelation function $B(\vec{r})$ was first introduced in relation to Compton profiling studies by Benesch in 1971. In Compton scattering γ-rays instead of positrons are used to obtain an electron momentum distribution, therefore $B(r)$ is the electron autocorrelation function. It was realized that the electron momentum density of a crystalline material can be seen as some kind of diffraction pattern and thus can yield spatial information that can be made visible by applying a Fourier transformation on this momentum density.

When using positrons, instead of $B(\vec{r})$, we talk about the positron-electron autocorrelation function $B^{2\gamma}(\vec{r})$, where 2γ stands for the two annihilation photons that result from the coinciding positron and electron. The definition of $B^{2\gamma}(\vec{r})$ is as follows:

$$B^{2\gamma}(\vec{r}) \equiv FT_{-3}\{\rho^{2\gamma}(\vec{p})\} \tag{2.12}$$

Where FT_{-3} is the 3-dimensional Fourier transformation and $\rho^{2\gamma}(\vec{p})$ is the momentum density of the annihilation photons, and is given by

$$\rho^{2\gamma}(\vec{p}) = \sum_{allstates} \left|\psi_{+,j}(\vec{p})\right|^2 = \sum_j \left|FT_{-3}[\psi_{+,j}(\vec{r})]\right|^2 \quad (2.13)$$

Where the summation over all occupied electronic states *j* and where $\psi_{+,j}$ stands for the positron-electron wavefunction, which under the independent particle model approximation, is given by $\psi_{+,j}(\vec{r}) = \psi_+(\vec{r}) \cdot \psi_j(\vec{r})$.

It is not yet feasible to measure $\rho^{2\gamma}(\vec{p})$ directly. In this report we use the 2D-ACAR momentum distribution $N(p_x, p_y) = \int \rho^{2\gamma}(\vec{p}) dp_z$ and the 1D-momentum distribution $N(p_x) = \iint \rho^{2\gamma}(\vec{p}) dp_y dp_z$. The autocorrelation function derived from $N(p_x)$ then becomes[76]

$$B^{2\gamma}(x)\Big|_{y=0,z=0} \sim FT\{N(p_x)\} \quad (2.14)$$

In the rest of this subsection we keep using the full $B^{2\gamma}(\vec{r})$.

Using the convolution theorem, the autocorrelation function can also be rewritten as[35]

$$B^{2\gamma}(\vec{r}) = \sum_j \int \psi^*_{+,j}(\vec{r}+\vec{s}) \cdot \psi_{+,j}(\vec{s}) d\vec{s} \quad (2.15)$$

This form better shows the nature of this function: it is the summation over all electronic states *j* of all the autocorrelates of the positron-electron wavefunction.

Zero crossings

Useful information is contained in the zero crossings of $B^{2\gamma}(\vec{r})$. In this paragraph we explain where the zero crossings occur and what information they contain.

In defect-free material, the electron wavefunction $\psi_j(\vec{r})$ is a periodic (Bloch) function. In this case, $B^{2\gamma}(\vec{r})$ has the property that it undergoes zero crossings when $\vec{r}$ is very close to half-multiples of a lattice vector $\vec{R}$. To see why this happens, $\psi_j(\vec{r})$ can be written in the Bloch form: $\psi_j(\vec{r}) = u_j(\vec{r}) e^{-ik\cdot\vec{r}}$ so that $\psi_{+,j}(\vec{r}) = u_{+,j}(\vec{r}) e^{-ik\cdot\vec{r}}$, with $u_{+,j}(r) = u_j(r)\psi_+(r)$ .Which results in

$$B^{2\gamma}(\vec{r}) = \sum_j e^{-ik\cdot\vec{r}} \int u^*_{+,j}(\vec{r}+\vec{s}) u_{+,j}(\vec{s}) d\vec{s} \quad (2.16)$$

The zero crossing positions can be understood from looking at the phase factor $e^{-ik\cdot\vec{r}}$. For each electronic state *j*, seen in one-dimension, $-\pi/R < k \le \pi/R$ (the 1st Brillouin zone). For example for $r = R/2$, we have for the exponent of the phase factor $-\pi/2 < ik\cdot r \le \pi/2$. In the unit circle this corresponds to the phase factors with $\mathrm{Im}\{e^{-ik\cdot r}\} \ge 0$. Summation over all the phase factors results in $\mathrm{Re}\{\sum_j e^{-ik\cdot r}\} = 0$. Therefore $B^{2\gamma}(r = R/2) = 0$, which is the first zero crossing.

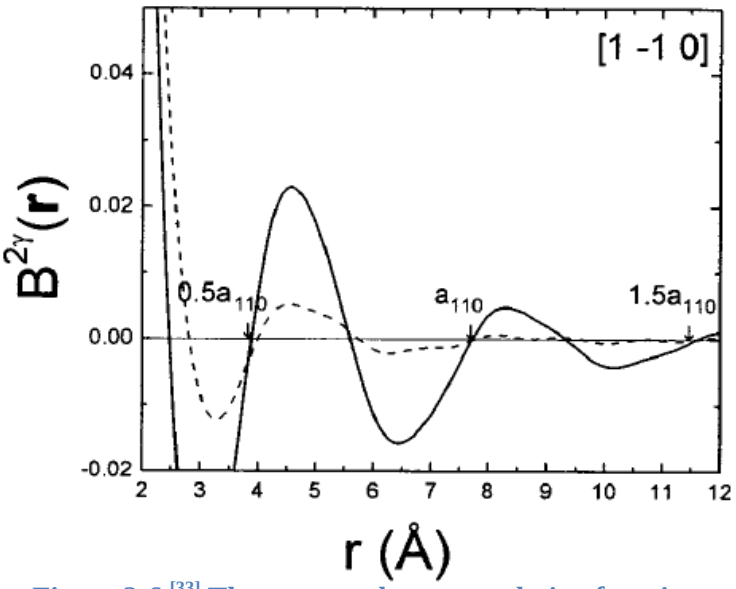

Figure 2-6.[33] The measured autocorrelation functions $B^{2\gamma}(r)$ are shown for bulk P-doped c-Si (solid line) and E-center P-doped c-Si (dashed line).

For $r = R$, $-\pi < ik \cdot r \leq \pi$, which corresponds to a fully used phase diagram. Therefore both $\mathrm{Re}\{\sum_j e^{-ik \cdot r}\} = 0$ and $\mathrm{Im}\{\sum_j e^{-ik \cdot r}\} = 0$. At $B^{2\gamma}(r = R) = 0$ the second zero crossing is found, and so on for all multiples of $R/2$.

It can also be understood from the phase factors that $B^{2\gamma}(r)$ is a damped function. For $r = 5R/4$, the unit circle is used 1+1/4 times. A summation over all phase factors results in cancellation of most factors. Only half of the factors with $\mathrm{Re} \geq 0$ and $\mathrm{Im} \geq 0$ are not cancelled, so that $B^{2\gamma}(r = 5R/4) = 1/5 \cdot B^{2\gamma}(r = 0)$ for a constant integral part in (2.16).

Figure 2-6 shows an example of a $B^{2\gamma}(r)$ function as obtained from 2D-ACAR-measurements. Here Ho et al. measured $B^{2\gamma}(r)$ for P-doped silicon, where the positrons annihilate in the bulk (solid line). Note that the zero crossings for c-Si nearly coincide with the lattice parameters. It has been shown both theoretically and experimentally that in particular the first zero crossing shows an outward shift, of typically 2%. The shift is a result of the correlation between the electron and the positron, which causes slight differences in the amplitudes of the summed phasors.[33,34]

The desired function for studying defects

In the paragraph above we saw that the zero crossings of $B^{2\gamma}(r)$ are a measure for the lattice parameters, when only delocalized positrons and Bloch state electrons in a regular semiconductor crystal are considered. However, we want to use $B^{2\gamma}(r)$ to study the electronic states near the material defects.

Ho et al. also used $B^{2\gamma}(r)$ for this purpose. They studied a specific open volume defect called the E-center, which is a monovacancy defect in doped c-Si. They obtained the dashed line in Figure 2-6. Among other things, a big outward shift in the first zero crossing position can be observed. This time, the shift is due to the increased interatomic distances near the (open volume) annihilation sites. We see that $B^{2\gamma}(r)$ can be used as a direct probe for obtaining spatial information at the defect site.

When applied to material with defects, both localized and delocalized electron orbitals will be measured. Ideally it is desirable to extract the component of $B^{2\gamma}(\vec{r})$ with only localized electron states at the defect site, such as:

$$B_{loc}^{2\gamma}(\vec{r}) = \sum_{j=1}^{n_{loc}} \int \psi_{+loc,j}^{*}(\vec{r}+\vec{s}) \cdot \psi_{+loc,j}(\vec{s}) d\vec{s} \qquad (2.17)$$

When this component of the data would be available, this would help visualizing the spatial structure near the defects. Unfortunately there is no known method yet to isolate the contribution of the electrons defect states. Therefore certainly in a crystalline material, there is always a large contribution from the delocalized electron states in $B^{2\gamma}(r)$, even for saturated trapping at induced defects in the material, as was the case for Ho. For amorphous materials with defects, the contribution from delocalized electrons is expected to be smaller because of the lack of large order structure.

Positron binding energy

Ho et al.[35] have also used $B^{2\gamma}(\vec{r})$ to say something about the positron binding energy. This was done using the relation derived by Kobayasi[36] between the positron-electron autocorrelation function $B^{2\gamma}(\vec{r})$ and the electron autocorrelation function

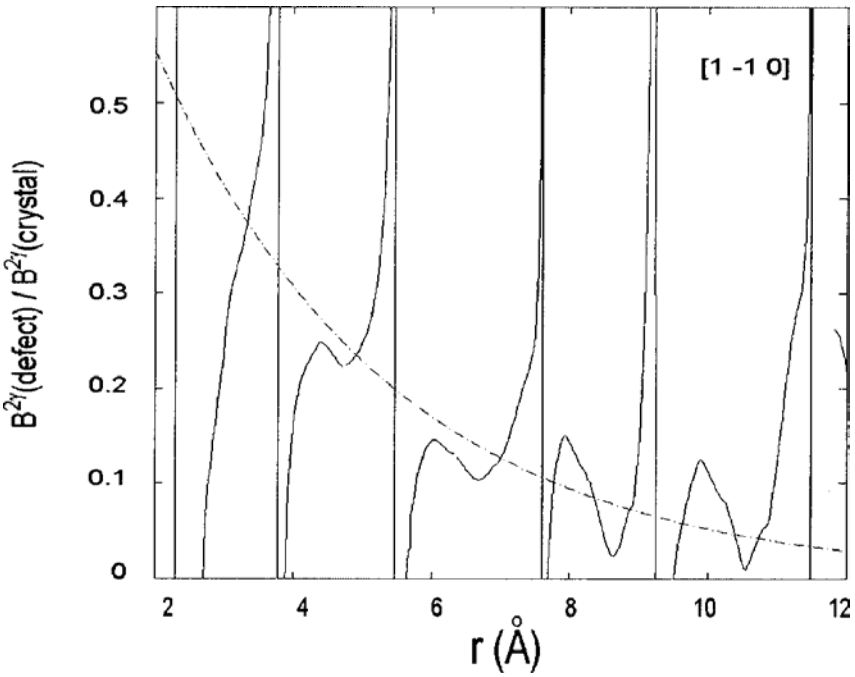

Figure 2-7. Estimating the positron binding energy from the exponential decay of $B_{defect}^{2\gamma}(r) / B_{crystal}^{2\gamma}(r)$ as a function of r. Figure taken from Ho et al.[35]

$B(\vec{r})$ as obtained in Compton profile measurements:

$$B^{2\gamma}(\vec{r}) = \overline{P(\vec{r})}B(\vec{r}) \tag{2.18}$$

Here $\overline{P(r)}$ is called the averaged positron autocorrelation function.

Assuming that the vacancy defect can be modelled as a square well trap for the positron, Ho approximated $\overline{P(r)}$ as:

$$\overline{P}(r) = e^{-\alpha|r|} \tag{2.19}$$

In this case the positron-electron autocorrelation function $B^{2\gamma}$ instead of the electron autocorrelation function B was used, because the two functions were considered to be almost the same. By plotting the ratio $B^{2\gamma}_{defect}(\mathbf{r})/B^{2\gamma}(\mathbf{r})$ the parameter α can be estimated by fitting a decaying exponent through all of the graph except for the infinity areas near the zero crossings (as was done in figure 2-7). α is related to the positron binding energy according to

$$\alpha = \frac{1}{\hbar c}\sqrt{2mc^2 E_B} \tag{2.20}$$

in which m is the positron effective mass.

2.3 Neutron reflectometry

In this section the principle behind neutron reflectivity is explained, and Ad van Well's model for computing the hydrogen concentration based on parameters from the neutron reflectivity profiles is described.

2.3.1 Principle of neutron reflection[37],[38]

In this subsection, first the principles of neutron reflectivity is explained and then it is made clear what information can be extracted from these measurements.

An incident plane wave of neutrons $\psi = e^{ikz}$ comes in under a small angle with the surface of the material of interest. Neutrons have interactions with nuclei in the material. As a result, a spherically symmetric neutron wave $\psi = -\frac{b}{L}e^{ikL}$ is reflected from the atom a neutron interacts with. The waves of the different neutrons interfere with each other. b is the scattering-length parameter, which varies strongly for different nuclei. This makes neutron reflectometry a useful technique to identify which atoms and isotopes are present inside a material. L is the distance from the neutron-material interaction.

Computing the reflectivity

Depending on the material structure, it is possible to calculate what the propagation of the neutron wave will be. The interaction of the neutron with the material can be described with the Schrödinger equation, by using the expression for the optical potential $V(z)$

$$V(z) = \frac{\hbar^2}{m_n} 2\pi \left\langle N(b_c(z) - ib_a(z)) \right\rangle \tag{2.21}$$

Where z is the distance from the film surface in nm, N is the atomic-number density, m_n the neutron mass, b_c the coherent-scattering length averaged for all isotopes the material contains in nm^{-2}, and b_a a measure for the absorption and incoherent scattering of the neutrons in the material, also in nm^{-2}. The Schrodinger equation can be reduced to

$$\frac{\partial^2 \Phi}{\partial z^2} + \{q^2 - \Gamma(z)\}\Phi(z) = 0 \tag{2.22}$$

Where $q = k_\perp$, the perpendicular component of the wavevector in vacuum, and where $\Gamma(z)$ is the scattering-length density in nm^{-2}, that is defined as

$$\Gamma \equiv 2m_n V / \hbar^2 \tag{2.23}$$

Note that this means

$$\Gamma(z) = 4\pi \left\langle N b_n(z) \right\rangle \tag{2.24}$$

where b_n is the nuclear scattering length in nm^{-2}. We will use this relation to determine the hydrogen content in the film (in section 4.3), by making use of the fact that the b_n takes very different values for different atoms/isotopes (see section 3.2).

In the neutron reflectivity experiments, the reflectivity $R = |r|^2$ is measured, where r is the amplitude of the scattered wavefunction $\Phi(z)$. q is also determined, from

$$q = \frac{2\pi}{\lambda}\sin(\theta_0) \tag{2.25}$$

by measuring the angle of reflection θ_0 and the neutron wavelength λ in nm. The measured reflectivity profile $R(q)$ is used to find the scattering-length density profile $\Gamma(z)$ by means of (2.22). In the next paragraphs, some special cases for the solution for the Schrodinger equation will be discussed, namely the reflectivity at a perfect surface, at a rough surface and for multiple layers.

Reflection at a perfect surface

Reflection at a perfect interface, that is between two materials or between vacuum and a material. With perfect interface, we mean perfectly flat, isotropic and homogeneous material.

The measuring quantity is $R(q)$, the reflectivity as a function of the perpendicular component q of the wave vector. The reflectivity can be calculated for each composition. It follows from the theory of neutron reflectivity that the formula for the reflectivity is just Fresnel's formula

$$R = \left|\frac{q_1 - q}{q_1 + q}\right|^2 \tag{2.26}$$

Where $q_1 = \sqrt{q^2 - \Gamma}$. An example of a reflectivity profile is shown in Figure 2-8a.

Reflectivity of multiple layers

In case of a varying scattering-length density it is more difficult or even impossible to find an analytic solution of (2.22). Therefore, the approximation is made where the material consists of multiple thin layers.

In case of several interfaces, the reflectivity of each layer can be computed recursively (for details, see De Haan[37]). As soon as there are at least two interfaces, the reflectivity profile contains a periodic component, as shown in Figure 2-8. The periodicity is due to interference of the reflectivity from top and bottom of one layer. For large q the period is given by $\Delta q = \pi/d$, with d the thickness of the layer.

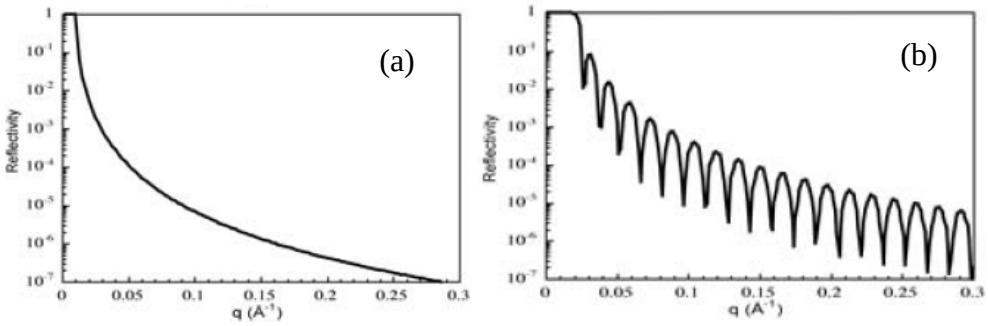

Figure 2-8. Neutron reflectivity from a perfect surface and from a two-layer material.

Rough surfaces

In practice the reflectance surfaces will not be perfectly flat. Using a roughness parameter that describes the thickness of the interface, it is possible to approximate the reflectivity profile. This can for example be done by describing the reflectivity at rough interfaces as the destructive interference of all wavefunctions created at interfaces positioned at different film depths.

Fitting procedure

The experimental results of neutron reflectometry were fitted using the least square method. That is, using the recursion relation, the weighted mean-squared deviation of the model reflectivity, called χ^2, is computed.

$$\chi^2 = (n-p)^{-1}\sum_{i=1}^{n}\left(\frac{R_i - M_i}{\sigma_{R_i}}\right)^2 \tag{2.27}$$

Here R_i is the measured reflectivity, M_i is the modelled reflectivity, n is the number of data points and p the number of fitting parameters of the model.

For each layer, the thickness, the scattering-length density and the interfacial roughness can be fitted.

2.3.2 Model for the hydrogen concentration

A model for computing the hydrogen concentration as a function of the scattering-length density for each layer is presented here. The model assumes that in case of a monovacancy, 1 Si atom is replaced by 4 H atoms, or in case of a divacancy, 2 Si atoms is replaced by 6 H atoms. It is assumed that hydrogen resides only in mono- or divacancies in the material, and that these vacancies do not change the material density appreciatively. (For details, see Appendix A3-1) . The following relation between hydrogen concentration c_H and the scattering length density ζ_n was derived.

$$c_H = \frac{N_{Si}b_{n,Si} - \zeta_n}{N_{Si}(b_{n,Si} - b_{n,H}) - \gamma\zeta_n} \tag{2.28}$$

Here c_H is the atomic hydrogen concentration of one layer assuming $Si_{1-c_H}H_{c_H}$, N_{Si} is the number of Si atoms in a volume of 1 nm^3, $b_{n,Si}$ is the neutron scattering-length density of silicon, $b_{n,H}$ is the neutron scattering-length density of hydrogen, $\gamma = 3/4$

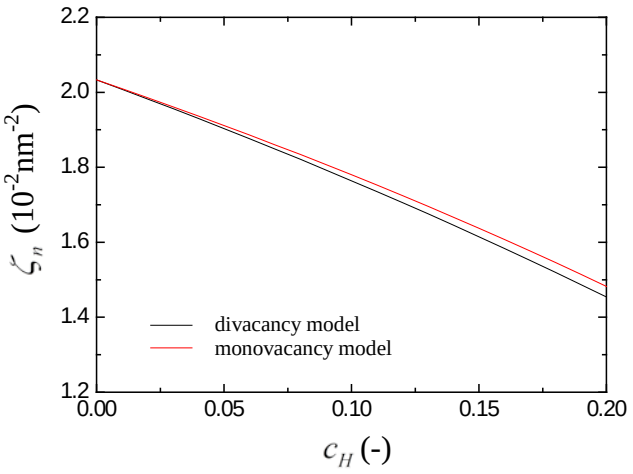

Figure 2-9. The variation of the neutron scattering-length density as a function of the hydrogen concentration for the mono- and divacancy model.

(monovacancy model) or $2/3$ (divacancy model) and $\zeta_n = \Gamma_n / 4\pi$ is the fitted neutron scattering-length density for the particular layer. ζ_n is the weighted average of the neutron scattering-length densities for Si and H. In Figure 2-9 the predicted variation of the neutron scattering-length density ζ_n with the hydrogen concentration c_H is shown.

2.4 Principle of Raman spectroscopy[39]

The principle behind Raman spectroscopy is explained in this section.

When a beam of monochromatic light is shone onto a solid state material, a fraction of the incident radiation is scattered, either elastically or inelastically, as illustrated in figure 13. The inelastic scattering causes emission of photons with energies that are mostly lower, but can be higher, than the energy of the incident photons. The photons with the lower energy are the photons of interest for the Raman experiment.

The difference in energy ΔE between the incident and the scattered photon is given by

$$\Delta E = \frac{hc}{\lambda_0} - \frac{hc}{\lambda_R} \tag{2.29}$$

where λ_0 is the wavelength of the incident photon and λ_R the wavelength of the Raman scattered photon. The loss in energy goes into the excitation of the nucleus/molecule into a higher vibrational level. The Raman spectrum is usually given in terms of the "Raman shift", which is the shift in wavenumber

$$\Delta\tilde{\nu} = \frac{1}{\lambda_0} - \frac{1}{\lambda_R} \tag{2.30}$$

where $\Delta\tilde{\nu}$ is the wavenumber shift in cm^{-1}. For certain bending, wagging and stretching vibrational modes, Raman peaks characteristic for the covalent bonds in the studied material can be observed, depending on the polarizability of the bonds. Detection of these vibrational modes can provide a lot of information about the material structure, such as its composition, chemical environment and degree of crystallinity.

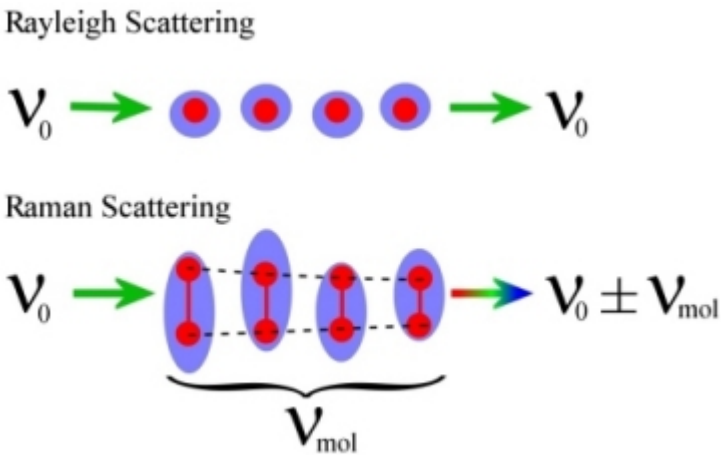

Figure 13.[40] Illustration of the elastic (Rayleigh) and inelastic (Raman) scattering process for a photon incident on a solid state material.

3 Experimental methods

In this chapter the experimental setups are described, followed by a description of the tested samples. Positron annihilation makes up the largest part of this study, therefore we start by discussing those setups. We proceed with the neutron setup, shortly talk about Raman spectroscopy, to finish with the description of all samples used.

3.1 Positron set-ups

In this study two positron beams have been used, named VEP "variable energy positron beam" and POSH "positrons from the HOR (Hoger Onderwijs Reactor)". Three measurement setups are currently installed on those beams, namely DB-PAS, 2D-ACAR and CDB-PAS. In the subsections below all those measurement systems will be described.

3.1.1 2D-ACAR setup

The POSH setup is used for 2D-ACAR measurements (Angular Correlation of Annihilation Radiation). An overview picture is shown in Figure 3-1. The mutual angle between the two annihilation photons is measured, in a plane. On either side of the sample, two NaI(TI) scintillator detectors are placed perpendicular to the direction of the positrons when they enter the material, at distances of 10.875 m and 12.180 m from the sample (Figure 3-2). The detectors are placed at unequal distances in order to avoid problems during data analysis, as explained in 3.1.1.1.

Figure 3-1. Overview of the 2D-ACAR set-up. The positron beam is guided through the vacuum tube that is enclosed by stainless steel and copper, ending with a curve of 90°, entering the sample chamber that is situated near the lead blocks. At the left of the picture one of the detectors is shown from behind.

The different measurement parameters (energy or angle) determined the choices for the positron sources: in the case of 2D-ACAR a very intense positron beam is needed. This is so because only small angle annihilation photons can be used in the results, because of the small angle of aperture. Also, only two photons that are coincidentally detected contribute to the count rate, since the mutual angle between these photons is what we want to measure.

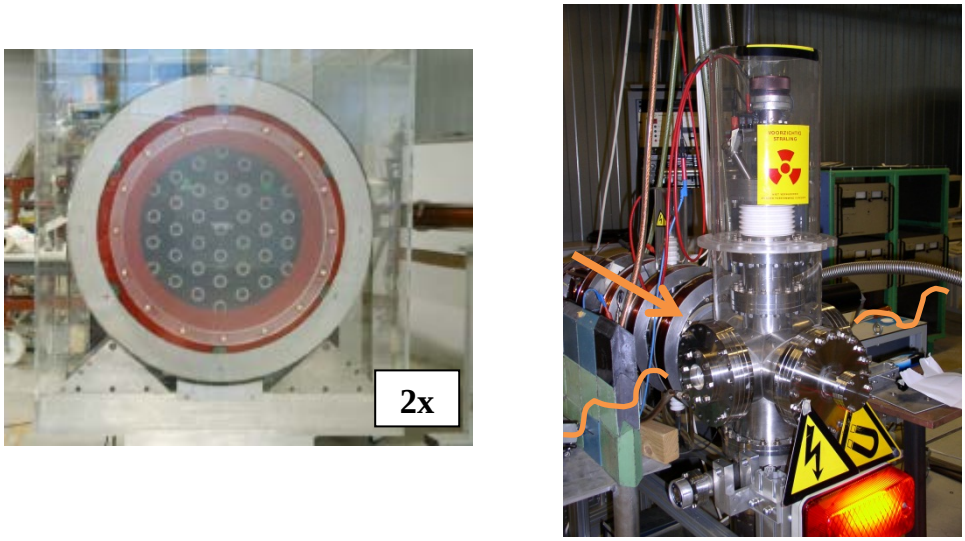

Figure 3-2. Close-ups of the 2D-ACAR set-up. At the right, the sample chamber is shown. The positrons enter the material from the back of the picture, the gamma rays emitted (almost) perpendicular to that direction are being captured by two NaI(Tl)-detectors. One of the detectors is shown in the left picture. These detectors are placed at distances of 10.875m and 12.180 m from the sample.

The source for the POSH beam creates 10^{11} positrons/s. After moderation and transport of the positrons, a strong magnet of 1.37 T, which is placed in line behind the sample, focuses the positron for a final diameter of 6 mm shining on the sample. The maximum intensity of the POSH beam upon entering the material is $2 \cdot 10^{8}$ positrons/s. The energy of the positron beam can be tuned between 1.2 keV and 20 keV using an electric field for additional acceleration.

2D-ACAR spectroscopy is used because of the very good resolution that can be obtained with this technique, which allows a better knowledge of the shape of the momentum distribution. The resolution of this setup is determined by two main factors. The beam spot creates an uncertainty on the angle of the annihilation photons, because the origin of the photons is not precisely known. To minimize this uncertainty, the detectors are placed far away from the sample. Secondly, the resolution of the detectors themselves partly determines the final resolution. For this setup, a resolution of $1.3 \cdot 10^{-3} m_o c$ x $1.1 \cdot 10^{-3} m_o c$ is obtained in x- and y-direction respectively, which is four times as good as the resolution of the DB-PAS setup.

The count rates at the single detectors are of the order of 10^{4} positrons/s, and the coincidence count is typically on the order of 10^{2} positrons/s at a positron energy of 3.7 keV – which is an energy typically used in this study. To obtain a full spectrum, typically 10^{7} counts are needed, which translates into 2-3 days measurement time.

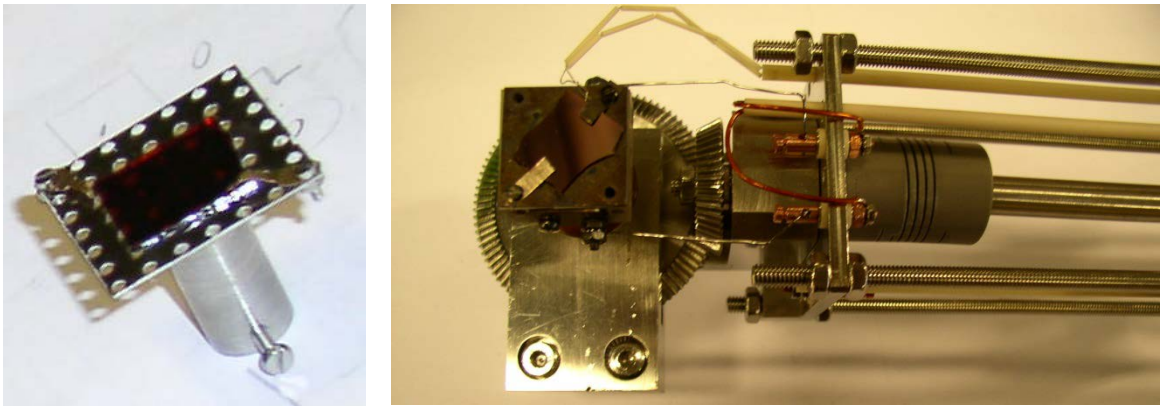

Figure 3-3. POSH sample holders. At the right the sample holder with heater, at the left, the normal sample holder.

The POSH sample holders are shown in Figure 3-3. In normal configuration, the sample is held in place by two tweezers that at the same time serve as metal contacts that prevent the sample from charging. The sample holder with heater enables heating the sample while keeping it in the vacuum chamber. The heater plate underneath the sample works by means of a resistance that is heated by driving a current through it. The thermocouple is clamped between one of the tweezers and the oven's surface, so that the temperature measured is mostly that of the heater plate.

3.1.1.1 Analysis of the 2D-ACAR distribution $N_m(p_x, p_y)$ [29],[41]

The measured distribution $N_m(p_x, p_y)$ obtained from the 2D-ACAR measurements is corrected for geometric effects by an already existing Matlab routine available at the RID.

First the data is corrected using the momentum sampling function that is calculated from the data of the single detectors. This function corrects for the specific measurement conditions in the particular setup. Most importantly, due to the finite detector (angle) aperture, high-momentum photons have a smaller probability to be detected. This is so because chances are high that one of the two high-momentum photons falls outside the window for detection. Another condition to correct for is the sample itself, which forms an obstruction for the annihilation gamma-rays to reach the detector, since many of them are scattered. Since each sample is different the momentum sampling function needs to be recalculated for each new measurement condition. The corrected momentum distribution is calculated by dividing the measured function by the momentum sampling function.

$$N_t(p_x, p_y) = N_m(p_x, p_y) / c(p_x, p_y) \tag{3.1}$$

Where $N_t(p_x, p_y)$ is the corrected momentum distribution and $c(p_x, p_y)$ is the momentum sampling function. The obtained momentum distribution is normalized to $\iint N(p_x, p_y)dp_x dp_y = 1$.

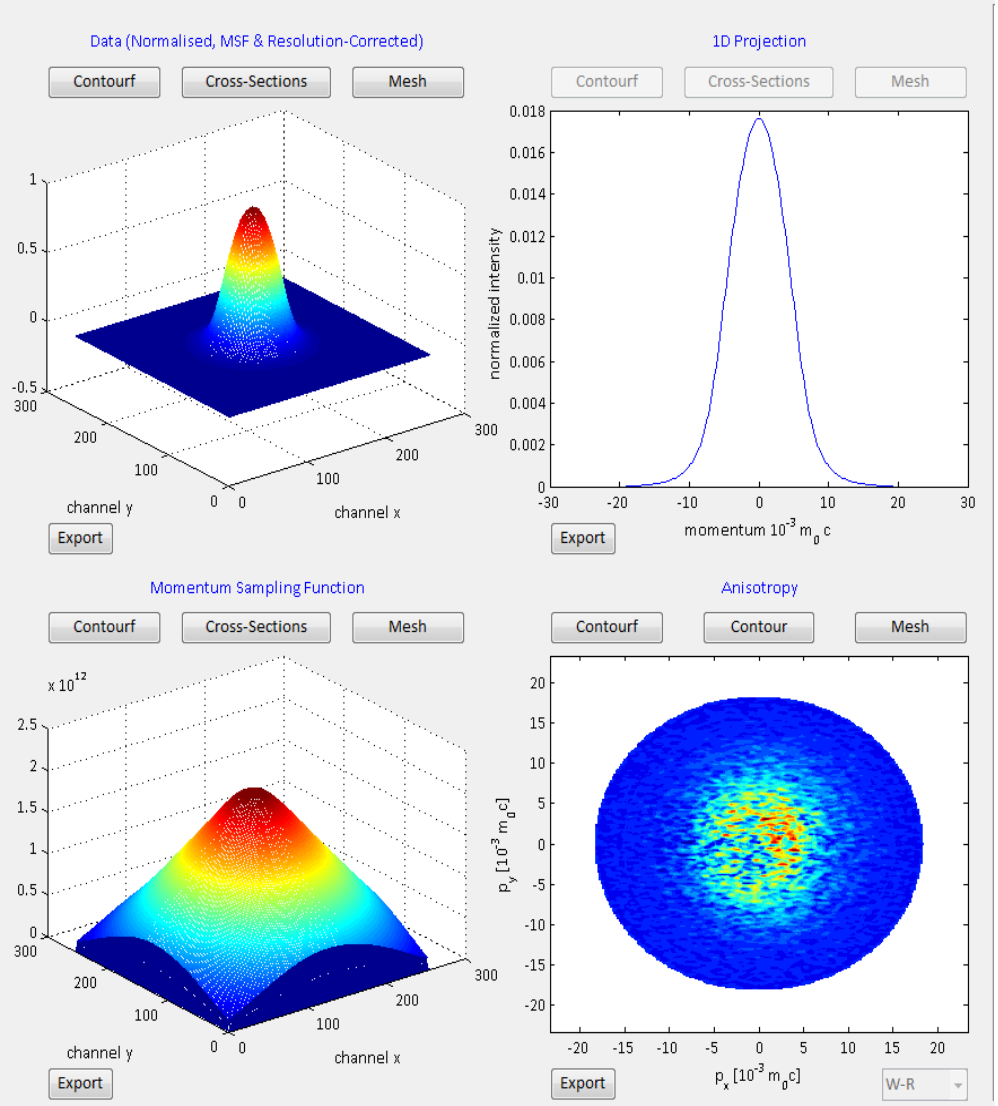

Figure 3-4. Example of a 2D-ACAR measurement after data analysis, where the obtained momentum distribution is (nearly) isotropic. The corresponding Momentum Sampling Function and a 1D-projection of the data along the y-axis are also shown.

Next the centre of the distribution is determined, and the data is shifted such that the centre coincides with channel (128,128) out of (255,255). After that, a resolution correction is applied in order to obtain the same effective resolution along p_x and p_y. These resolutions are different due to the resolution contribution of the beam spot, which has a diameter of ~6 mm in y- and z-direction, but as seen from the detectors, the thickness in the x-direction is $<1\mu m$, since all the annihilations take place within the thickness of the sample. This difference in resolution has to be corrected for. This is done by worsening the resolution in the direction with the best resolution, by convoluting the momentum distribution with a two-dimensional Gaussian function.[41]

The anisotropy of the momentum distribution is calculated next, by subtracting the isotropic function from the distribution. The isotropic function is in this case defined as the minimum values in the momentum distribution $N(p_x, p_y)$ found on circles $p^2 = p_x^2 + p_y^2$.
From the isotropic part of the 2D-ACAR distribution, the 1D-projection of 2D-electron-positron momentum distribution $N(p_x, p_y)$ is calculated by the Matlab routine. This is done by integrating $N(p_x, p_y)$ along the y-axis. For our a-Si:H samples the momentum distribution appears to be isotropic, statistical fluctuations aside.

An example of the result of the data analysis is shown in Figure 3-4. Note the flat top of the sampling momentum function. Suppose the two detectors were placed at equal distances, then the sampling function would be much at the top. Any misalignment of the centre would then translate in errors in the momentum distribution.

3.1.1.2 Analysis of the 1D-ACAR distribution $N(p)$

Part I: S & W Parameter
The acquired 1D-projection consists of 253 data points with a domain reaching from -23.51 to 23.51 mrad. Using Origin, a spline interpolation function of 10.000 points is created from these data points. This projected momentum distribution is then used to calculate the S- and W-parameter. The S- and W-parameters are calculated using $|p_l| \leq 3.5 \cdot 10^{-3} m_0 c$ for S and $10 \cdot 10^{-3} m_0 c \leq |p_l| \leq 26 \cdot 10^{-3} m_0 c$ for W.

Part II: Autocorrelation function
$N(\mathbf{p})$ is also used to calculate the positron-electron autocorrelation function $B^{2\gamma}$ and its zero crossings. $B^{2\gamma}$ is calculated by applying the Fast Fourier Transform of Matlab.[2]

The corresponding x-values are centred around x=0 and can be calculated as follows.

$$d\mathbf{k} = \frac{d\mathbf{p}}{\lambda} \cdot 10^{-13} \tag{3.2}$$

Where $d\mathbf{p}$ is in mrad and $d\mathbf{k}$ is in Å^{-1}.
The spacing between two consecutive x-values is then given by

$$d\mathbf{x} = \frac{2\pi}{253 \cdot d\mathbf{k}} \tag{3.3}$$

The x-values for the 253 FT points increase from x ≈ -64.74Å to x ≈ 64.74Å.

Part III: zero crossings

[2] In Matlab the FFT can be calculated using the following command sequence on the matrix containing all the momentum distribution intensities: “ifftshift”, “realfft”, “fftshift”.

Just like the 1D-momentum distribution, the acquired autocorrelation function consists of 253 data points. In order to find the 1st zero crossing of this function, the autocorrelation function is first spline interpolated with 10.000 points. The first positive zero crossing of the autocorrelation function is read out by zooming in and reading out by eye.

3.1.2 DB-PAS setup[2]

The VEP setup is used to perform DB-PAS (Doppler Broadening positron annihilation spectroscopy) measurements. The working of this method is based on determining the Doppler shift in energy of the annihilation photons as a function of implantation depth of the low energy positrons.

For Doppler broadening measurements, an intensity of 10^4 low energy positrons/s at the sample position suffices, because here a larger part of the annihilation photons can be used in detection. This is so because in this setup only the photon energy is measured. Therefore it is possible to place the detector close to the sample, which makes it possible to have a big (photon) angle of aperture. The lower required positron intensity makes it possible to use a commercial ^{22}Na-source.

Also in this case the positrons need to be moderated. The final positron beam can attain energies from 0.1 keV up to 30 keV. The diameter of this beam is 10 mm. A solid state Germanium detector is used. The solid state Ge-detector has its 4096 channels set such that energies between 0 and 555 keV are measured. For a typical measurement of $1 \cdot 10^6$ counts in the 511 keV peak region, measuring 5 minutes at one energy suffices. This makes the setup suitable for measuring at many energies, resulting in depth profiles. The resolution of the setup is around $6 \cdot 10^{-3} m_o c$. Because of the limited resolution, two parameters, S and W, are extracted from the Doppler broadened 511keV photo peak to characterize the 1D-momentum distribution (see also Figure 2-5)

Figure 3-5. Samples can be heated inside the VEP setup, using the cylindrical ceramic oven as shown here. The sample holder is grounded and the temperature is measured using a thermo couple.

Oven setup of DB-PAS

A cylindrical shaped ceramic oven is designed to enable annealing experiments on the DB-PAS setup. The oven is shown in figure 3-5. By applying current, the oven is heated using a resistance. Through radiation transport, the sample is heated all the

way around. The current is regulated manually and is monitored using multimeters. The oven can be used for heating up to at least 1400°C. The thermo couple is situated at the centre of the sample as much as possible and touches the sample at the back of the glass substrate.

3.1.2.1 Data analysis VEPFIT

The DB-PAS measurements result in two depth profiles as a function of the mean positron implantation energy E, namely $S(E)$ and $W(E)$. Using the fitting program VEPFIT it is possible to create a simulation that fits the measured depth profiles, by assuming that the material consists of stacked layers of different materials, density, positron diffusion length and thickness of each layer.

The program assumes that the implantation profile of the entering positrons is Makhovian-shaped. The equation for implantation of positrons and diffusion of thermal positrons, in combination with trapping at defects, is solved iteratively. The annihilated photons that make up the depth profile can either originate from surface states of the positron, annihilation at defects or in the bulk of the film, or from annihilation in the substrate. Together these fractions determine the S (or W)-parameter as a function of the positron incident energy for each implantation energy E according to

$$S(E) = \sum_{i=1}^{n} f_i(E) S_i + f_{surface}(E) S_{surface} + f_{substrate}(E) S_{substrate} \qquad (3.4)$$

Here $f_i(E)$ is the fraction of the positrons that annihilate in film layer i at a positron implantation energy E. S_i is the value of the S-parameter in the same film layer i and is the weighted average of annihilations in defects and in bulk of the film. $f_{surface}(E)$ and $f_{substrate}(E)$ are the positron fractions that, at an energy E, annihilate from surface or substrate states. $S_{surface}$ and $S_{substrate}$ are the S-parameters at the surface and at the substrate.

In this thesis the depth profiles are fitted assuming one or two a-Si:H layers of densities 2.2 g/cm^3 and 2.25 g/cm^3 on top of a glass substrate of 2.312 g/cm^3. The density is one of the parameters that cannot be fitted, since it is part of the assumed

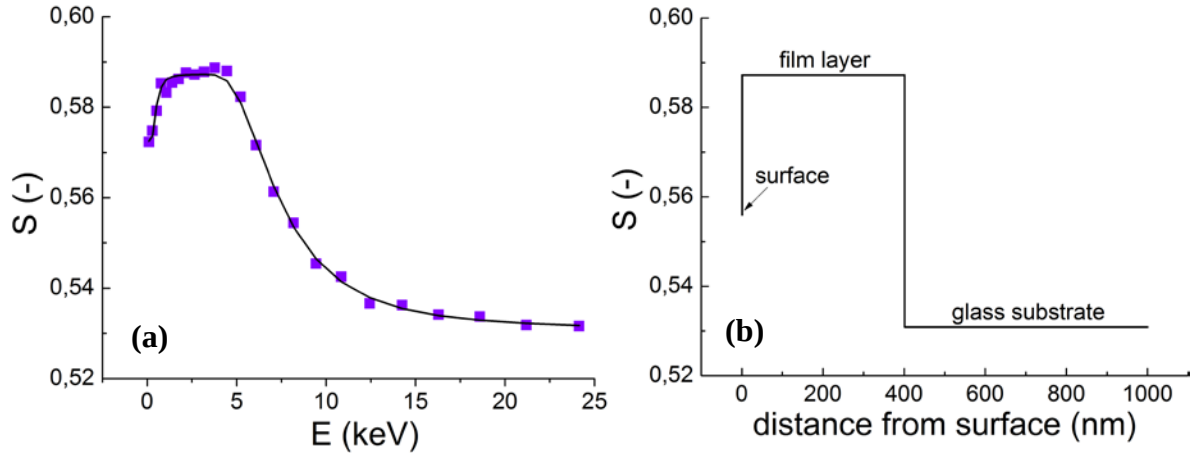

Figure 3-6. Example of a DB-PAS depth profile. (a) measured and fitted S(E) depth profile for an a-Si:H sample deposited in triode configuration, using VEPFIT, assuming the one-layer structure as shown in (b).

implantation profile. For the annealing experiments the surface S- and W-parameters are kept fixed, which is in line with the previous (related) annealing experiments performed. This fixation has the advantage that there is little variation in the fitting errors for the different fits in the annealing experiment series. During fitting of the W-profile the fitted thicknesses that were calculated for the S-profile are used.

The diffusion length of all the a-Si:H layers is kept fixed at 3 nm to vary the fitting conditions as similarly as possible. In c-Si the positron diffusion length can be two orders of magnitude bigger. The density of c-Si was taken 2.33 g/cm^3.

Figure 3-6 shows an example of a fit performed using VEPFIT. Here, one layer was used to model the film.

3.1.3 CDB setup[29]

At the POSH setup, apart from the 2D-ACAR setup, there is also room for a second setup. Two Ge solid state detectors have been placed under a different angle to allow for coincidence Doppler Broadening measurements at the same time as the ACAR measurements. Thanks to the coincidence measurements the resolution is improved with a factor $\sqrt{2}$ relative to conventional Doppler broadening using a single Ge-detector. A very important fact is that the peak to background ratio is reduced by a factor of 100. Together, the energies of the two photons needs to be 1022 keV, with a margin of 1.3 keV (cutting out most of the background). The resolution of the system then becomes 1.3 keV / $\sqrt{2}$ = 0.9 keV, or $3.5 \cdot 10^{-3} m_o c$. Due to the low background, CDB is well suited for measurements in the high momentum regime.

Data analysis CDB

Figure 3-7 shows an example of a two-dimensional photon spectrum obtained with Coincidence Doppler Broadening. The colours provide an idea of the intensity distribution. The central peak is caused by events where two photons with small Doppler shifts are detected. The horizontal and vertical bands are coincidence events of one 511 keV photon and one background photon, which can for example be a Compton scattered photon. From the CDB spectrum we extract the counts on the diagonal $E_1 + E_2 = 1022 keV$ line with a small margin of 1.3 keV around it. The event counts of the small margin are projected onto the 1022keV line in order to obtain a one-dimensional momentum distribution. In this way the background is reduced 100 times.

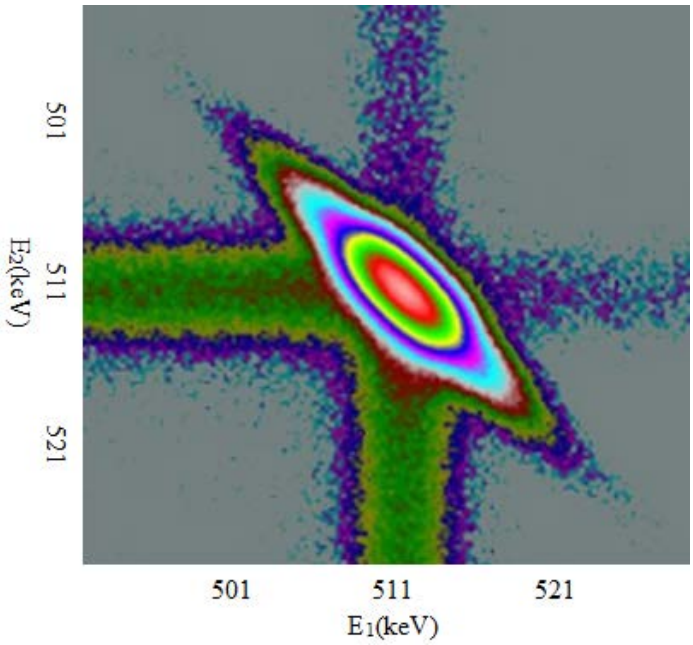

Figure 3-7. Example of a Coincidence Doppler Broadening spectrum.[42]

3.2 Neutron reflectometry set-up

In this section we explain how the neutron reflection measurements were performed and also how the obtained reflection profile can be fitted.

3.2.1 ROG setup

For the neutron reflectometry experiments, the ROG setup "Reflectometer voor oppervlakte- en grenslaagonderzoek", shown in Figure 3-8, was used. The neutron beam consists of products of the fission reactor source at the RID. The thermal neutrons travel in a direct line towards the setup. Some gamma rays are also contained in the neutron beam, but their intensity is reduced as much as possible using some tricks such as shielding them using lead blocks.

Since each sample has a different thickness, the setup needs to be calibrated prior to the measurement. Below we will describe the different components of the setup, including the calibration.

Neutron beam

The width and the angular spread of the incoming neutron beam is regulated using two diaphragms that are situated 3 m apart. The beam needs to be calibrated before each measurement. A smaller beam spot increases the resolution and decreases the angular spread, but also increases the measurement time due to the decreased intensity.

Neutron wavelength

The reflectivity profile R(q) is measured, with the goal of determining the scattering-length density depth profile. Remember that q is the component of the wavevector perpendicular to the surface of the sample.

$$q = \frac{2\pi \sin(\theta)}{\lambda} \tag{3.5}$$

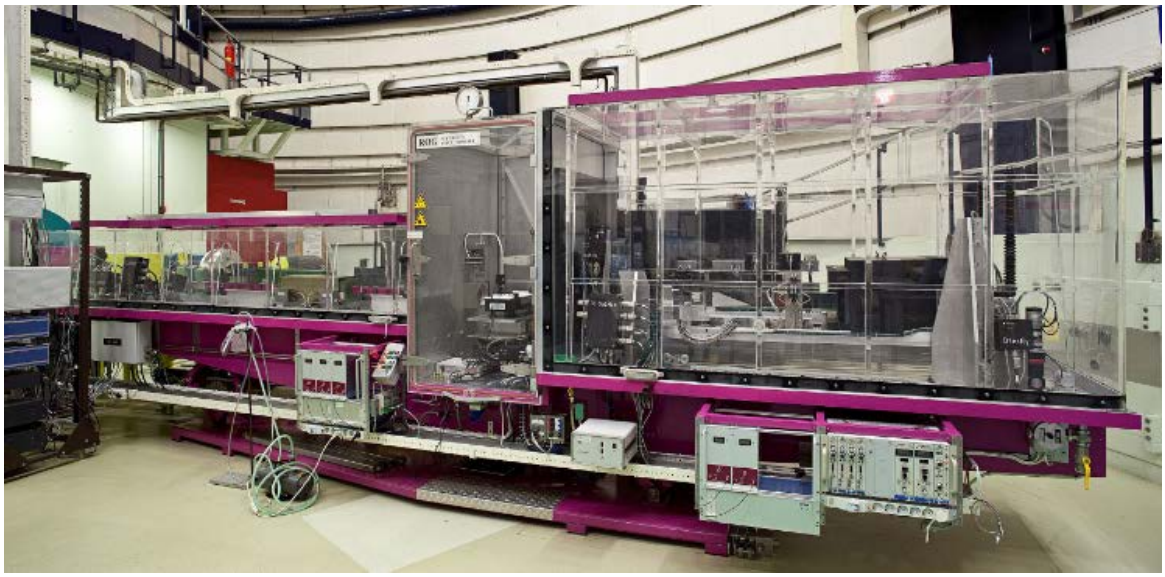

Figure 3-8. The neutron reflectometry setup "ROG" consists of 3 chambers. Both the left chamber (that contains diaphragms and monitors) and right chamber (that also contains the detector) including all their components can be tilted under the desired angle. The chamber in the middle contains the sample.

In this setup, q is varied by varying the wavelength λ and keeping the angle of incidence θ constant.

The final intensity of the incoming neutron beam is wavelength dependent and varies between 10^6 $s^{-1}cm^{-2}nm^{-1}$ at λ = 0.8 nm and $2 \cdot 10^8$ $s^{-1}cm^{-2}nm^{-1}$ at λ = 0.16 nm. Wavelengths between 0.08-0.8 nm can be used. The intensity is measured using a monitor, which is a device that leaves most neutrons undisturbed, but absorbs and measures a small percentage of them. The wavelength is varied by using the Time-Of-Flight method: a double-disk chopper prevents all neutrons from passing through, except for neutrons in a certain speed frame.

Samples

The desired neutron sample size is much bigger than the size that can be used in the positron experiment. For the neutron reflectometry study, 10x10 cm^2 samples were deposited on thick quartz substrates to ensure a sufficiently flat surface. Their characteristics are listed in section 3.4.2.5. The neutron beam was adjusted such that the maximum spot size matched the sample size.

In a-Si:H there are Si-atoms and H-atoms. Since the samples have spent some time in the air, an small oxygen layer is expected on top as well.
The difference in scattering lengths is big, leading to a good contrast, see Table 3-1:

Table 3-1. Neutron scattering lengths for H, Si and O respectively.

	b_n (fm)
H	-3.739
Si	4.149
O	5.803

The good contrast is helpful when determining the H-concentration and distribution in the a-Si:H film.

Detection

A single detector of type XERAM 30NH15 filled with He-3 was used for detection of the reflected neutron beam.

3.2.2 Data analysis

Some data correction calculations need to be performed before the obtained data can be fitted with the Gustar program. In particular, corrections for dead time, background and efficiency need to be performed.

Once that is handled, the reflection profile is ready for fitting. There are quite a few parameters that can be learned about by fitting the data correctly. The most important parameter here is the scattering-length density depth profile, which contains the information about how the elements are distributed along the sample. Also, as discussed already in the theory, the period of the oscillations contains information about the thickness of the sample layers.

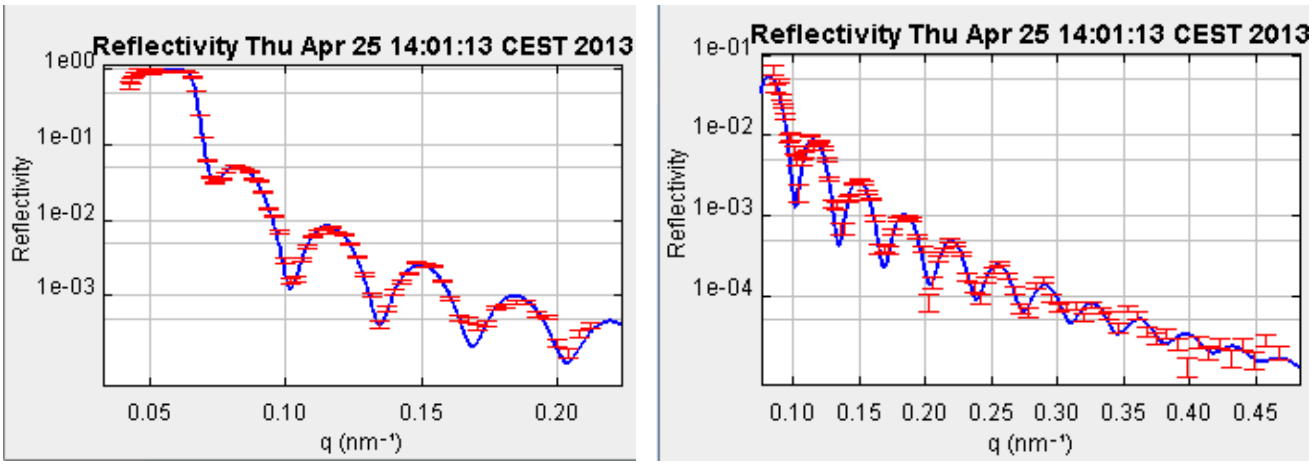

Figure 3-9. Neutron reflectometry measurement at two different angle domains, fitted using Gustar.

The thickness and the SLD need to be fitted. There is a large number of parameters that can also be fitted. An important one is the roughness of the interfaces. Also we always have the ambient layer and the substrate, both of which also have SLDs. Resolution, normalization and background also need to be taken into account, as fit parameter.

In Figure 3-9, an example of a fitting result for one of the samples (a-Si:H deposited from undiluted silane gas) is shown. Two measurements were performed on the same sample, where q was varied under two constant incident angles. Gustar has the option to simultaneously fit the resulting depth profiles to both reflectometry spectra.
In Figure 3-10 the fitted scattering-length density is shown as a function of depth. The ambient layer and substrate are included. The roughnesses of the interfaces can also be observed.

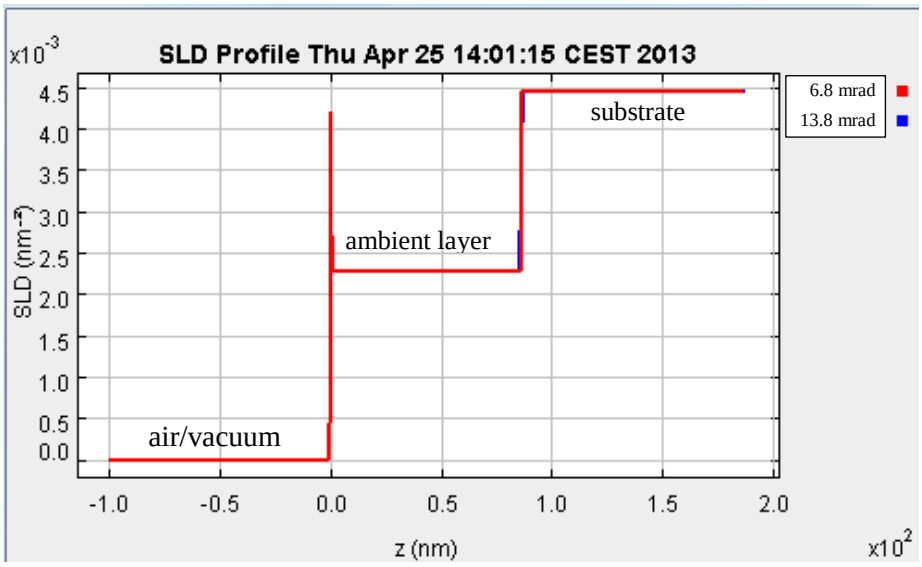

Figure 3-10. Example of an SLD(z) model that can be fitted on the measurement data using Gustar. The model is used to simultaneously fit the data taken at both the incident angles, here 6.8 mrad and 13.8 mrad.

3.3 Other characterization methods

3.3.1 Raman spectroscopy

The Renishaw inVia Reflex confocal Spectrometer setup situated at the Kavli Nanolab is used for Raman spectral analysis. Monochromatic laser light of 514 nm Ar^+-laser is shone onto the samples, causing molecular vibrations. The light that is scattered back mostly results from elastic scattering, keeping the same wavelength. A small part of the light is scattered inelastically and undergoes a change in wavelength (i.e. change in energy of the photon). It is this part of the light we wish to analyse, since it contains information about the molecular bonds within the material, in particular its frequency $\omega = \frac{\Delta E}{\hbar}$.

The 514 nm light is filtered out of the scattered light. In the Kavli Nanolab a Notch filter can be chosen for this, allowing a wavelength spectrum of 100-5000 cm^{-1} to be detected. The setup contains a Renishaw RenCam CCD array detector with 1024x256 pixels.

Figure 3-11. A Renishaw Raman setup.[43]

3.4 Samples

3.4.1 Deposition of a-Si:H films

All a-Si:H films are deposited on Corning Eagle XG glass substrates using radio frequency Plasma Enhanced Chemical Vapor Deposition (rf-PECVD). Silane gas (SiH_4) is used as the reaction gas. It is diluted in different quantities with hydrogen gas. With this deposition technique the growth can be varied by changing the following parameters: the gas pressure, substrate temperature, gas flow ratio $R = [H_2]/[SiH_4]$ and the rf-frequency.

The samples used for positron measurements were produced on Corning Eagle XG glass substrates of 2.5x10 cm, and were cut smaller from the larger film using a scratch pen to make them fit inside the PAS setups. Some examples can be seen in Figure 3-12.

Most neutron samples were produced on the maximum substrate size of 10x10 cm and some were produced on slightly smaller substrates of 3.5x3.5 inch (~ 8.9 cm). The neutron reflectometry quartz substrates of 0.635 cm in thickness were used, that have been polished by the manufacturer in order to ensure that the deposited film is as flat as possible.

The glass substrate has a thickness of 0.7 mm.

By using big hydrogen dilutions during PECVD, microcrystalline material is formed instead of amorphous silicon, as we already saw in the introductory chapter.

3.4.2 Sample sets

3.4.2.1 R-series

An important sample set for this study is the set with different hydrogen dilutions. It has been found that the light-induced degradation is less when the hydrogen dilution is higher and we want to find the explanation for it at a nanostructural level. The sample set is listed in Table 3-2.

Table 3-2. Hydrogen diluted samples, together referred to as the 'R-series'. The thicknesses[44] listed are measured optically and have a fitting error of ~1nm.

Sample name	Hydrogen ratio R (-)	Thickness (nm)
M1580	0	433
M1582	2.5	403
M1584	5	414
M1586	7.5	419
M1588	10	392

The a-Si:H layer thicknesses of all samples have been optically determined and are around 400 nm. These samples have been studied before by bachelor student Albert Vullers[44] using DB-PAS. Some interesting trends in S and W were found as a function of R, which forms the reason to perform additional positron experiments on this series, namely 2D-ACAR measurements.

To learn more about these materials, a 2D-ACAR measurement was performed on each sample at an initial positron energy of 3.7 keV, ensuring that we measure at the right depth, i.e. in the bulk of the a-Si:H layer.

3.4.2.2 Extended R series

Some additional hydrogen diluted samples were studied, that were produced in the same way as the R-series. They are described in Table 3-3.

Table 3-3. Some notes about extended R-series samples.

Sample name	R	Remarks
M1583	2.5	Same as M1584, but twice as thin, only 233.5 nm (RT)
M3459	2.5	Resembles M1584, new batch. Unexpected results for the shape of the momentum distribution on 2D-ACAR for M1584 gave rise to measuring again with a new sample.
M3056	0	Trying to find extension of the (S,W) trend found for R=0 t/m 10.
M3058	10	
M3060	12.5	

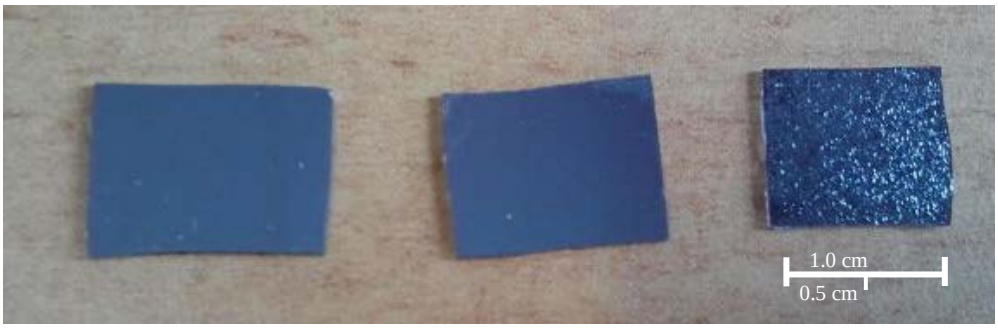

Figure 3-12. Samples M3056 M3058 and M3060 respectively. At the right, peeling of the R=12.5 film is clearly visible. The R=10 film also shows some peeling at the edges. The R=0 film at the left does not show peeling off. The photograph was taken a few months after deposition, but the peeling off at the R=12.5 film was visible from the start.

All samples were measured with DB-PAS, except for sample M1583, which was for an annealing experiment on the POSH beam. Coincidence Doppler measurements and 2D-ACAR measurements were performed at the same time at the POSH beam. After each annealing step, the depth profile was also measured again using one of the Ge-detectors. The data acquired for this sample M1583 is referred to as the 'T-series'.

Sample M3459 was measured using both DB-PAS and 2D-ACAR.

Samples M3056, M3058 and M3060 were produced to find an extension for the (S,W) trend found for R=0 up to R=10. Higher-R samples were produced as well, but those films did not stick to the substrate: the stress in the material appears to be too high for the film to stay as the top layer. (Figure 3-12) Inside solar cells it is possible to use higher R absorber layers.

3.4.2.2 High pressure sample

Recently, very good solar cell characteristics have been obtained for a solar cell with an absorber layer produced under high pressure[96]. The sample has a rather high V_{OC} and is called A4932.

To see what the effect of the different deposition condition is on the nanostructure of the film, a DB-PAS depth profile and annealing experiment is performed on this sample too.

3.4.2.3 Diode/triode samples

Samples from the Japanese research group AIST in Tsukuba are measured with DB-PAS. The samples were produced by Dr. T. Matsui and Dr. K. Saito from the Research Center for Photovoltaic Technologies, AIST, Tsukuba. We refer to the samples as diode/triode samples. The solar cells corresponding to these samples have excellent initial and light-soaked efficiencies as shown in Table 3-4. Three of the samples have been deposited using the normal diode rf-PECVD configuration and three samples have been deposited using a third mesh electrode in between the parallel plates. This electrode contains holes and by putting a voltage on it, the radicals that arrive at the substrate can be selected. The triode configuration automatically has a lower deposition rate as well, as also shown in the table.

Table 3-4. Summary of the diode and triode sample characteristics. Their hydrogen dilution, deposition rate, initial- and light-soaked efficiency, relative degradation of the fill factor and relative degradation of the fill factor are all listed.

Sample	R	Deposition rate (nm/min)	Initial Efficiency (%)	Light-soaked efficiency (%)	Rel. deg. fill factor (%)	Deposition method
T09_5	1	1.62	9.7	9.0	7.1	Triode configuration
T10_2	7	0.96	8.8	8.3	6.5	
T11_1	0	1.68	9.8	8.8	9.6	
D15_1	1	10.92	9.7	8.1	12.0	Diode configuration
D15_3	7	3.18	9.1	7.1	16.2	
D15_5	0	11.28	9.5	7.7	12.6	

3.4.2.4 c-Si reference samples

FZ-Si samples are used as reference samples for the DB-PAS depth profile and annealing experiments. It was noticed that the oven influences the observed values for the S- and W-parameter (this will be discussed in the R&D section), therefore depending on the experiment, the reference sample is measured either in the oven or in the normal setup. In the DB-PAS annealing series on R=0 (M1096) and R=10 (M1588) Cz-Si was used as a reference sample. FZ-Si and Cz-Si are measured to have the same S- and W-parameters without oven, even though they differ in defect and impurity density, therefore both can be used to obtain the normalized S- and W-values.

Table 3-5. S- and W-values of all c-Si reference measurements.

c-Si reference sample used for experiment	Sample holder	S	W
R=5 (oven)	Oven	0.5597	0.0329
High pressure sample (oven)		0.5633	0.0321
Extended R-serie samples	Normal	0.5714	0.0284
Diode/triode		0.5712	0.0281

3.4.2.5 Neutron series

One of the important questions concerning the nanostructure of a-Si:H is: where does the hydrogen go? This has proved to be a difficult question to answer. Neutron reflectometry is a non-destructive technique that can help to determine the distribution of elements as a function of the film thickness. This study is a first investigation to see whether the technique is sensitive enough to distinguish hydrogen concentrations between different samples. It is also a question with how many layers the a-Si:H film should be modelled, how many interfaces there are.

Reasons for wanting to know the hydrogen concentration is to learn about its influence on the behaviour of the material.

The a-Si:H films used for the neutron reflectometry experiments are thinner than the thicknesses of 150-300 nm that are typically used in commercial solar cells. This is a necessity in order to obtain resolvable reflectivity profiles. It is therefore possible that the nanostructure of these films differs somewhat from thicker samples that have the same R, since the growth can depend on the thickness of the layers on the substrate.

Four samples with large mutual differences were used for this first investigation to explore the sensitivity of neutron reflectometry to the variations in film properties. All are listed in Table 3-6. Samples M2671 and M2676 can be compared to the beginning and end of the R series which was central in the positron studies. Sample A6443 resembles the high pressure sample. In addition, a nc-Si:H sample A6437 was studied.

Table 3-6. Neutron reflectometry is performed on a wide variety of samples. The thicknesses have been determined from RT and ellipsometry measurements and the estimated hydrogen concentrations were determined from FTIR measurements.

Sample name	R (-)	[H] (at. %)	Phase	Thickness (nm)
M2671	0	9	a-Si:H	85 ± 0.5
M2676	10	11	a-Si:H	186 ± 1.0
A6443	50	12	a-Si:H	70 ± 1.5
A6437	250	4-6	nc-Si	65 ± 1.0

4 Results and discussion

The results of the experiments are presented in this chapter, where each result is followed by a discussion. The positron annihilation experiments that we used to study the open volume defects in the a-Si:H absorber layers make up the largest part of this thesis and are discussed first. Then the hydrogen distribution in some of these layers is studied using neutron reflectometry.

Part I: Positron Annihilation Spectroscopy

4.1 DB-PAS experiments

4.1.1 R-series: as deposited

In this subsection, the results from the DB-PAS measurements performed by BSc. Student A.S. Vullers on samples R=0 up to R=10 of the R-series that is described in section 3.4.2 are given. The resulting S(E) and W(E) depth profiles were fitted using VEPFIT assuming a one-layer structure (a-Si:H layer and Corning XG glass substrate). The fitting procedure is explained in section 3.1. The fitted S- and W-parameters were normalized by also measuring a depth profile of the c-Si sample in the same setup, and using $S_{normalized} = S / S_{c-Si}$. The resulting S- and W-parameters for each film layer are shown in Figure 4-1.

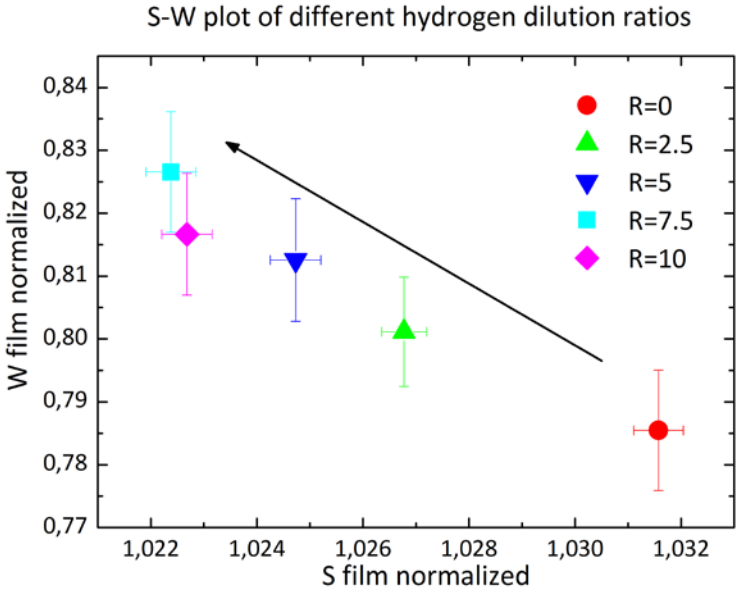

Figure 4-1.[44] (S,W) plot of the normalized S- and W-parameters for the R-series as obtained by fitting DB-PAS experimental results.

Momentum distribution broadening

A clear trend can be observed in this figure. As the H-dilution increases, the S-parameter of the a-Si:H layer decreases and the W-parameter increases. In other words: the momentum distribution seems to broaden. This broadening is consistent with previous experiments performed on similar samples[45]. It is also known that an increased hydrogen dilution during deposition leads to an increased hydrogen concentration in the deposited sample.[46] It seems that the increase in hydrogen is

somehow responsible for the broadening of the momentum distribution. In Eijt et al.[45], two explanations are given. Either the hydrogen causes the electron orbitals of the valence electrons in the material to be more localized in space, which translates into a broadening of the momentum. This can be understood since position and momentum are related by a Fourier Transformation. Alternatively, it could be explained by a decrease in defect concentration with increasing hydrogen content, since it is known that vacancy-related defects sharpen the momentum distribution. This latter explanation does not apply when all annihilating positrons are already trapped in defects (saturated trapping). When the defect density is large enough, the chance for a positron to be trapped in a defect increases, since enough defects will fall into the action radius of the diffusing positron.

Saturation of positron trapping
From previous depth profile fits with VEPFIT is known that the positron diffusion length inside the a-Si:H layers is somewhere between 3-10 nm. Saturated trapping then requires a minimum of $2 \cdot 10^{17}$-$9 \cdot 10^{18}$defects/cm^3. The expected neutral divacancy density in a-Si:H with 10 at.% hydrogen is $8 \cdot 10^{20}$defects/cm^3 [47] , which is well above the minimum value. Therefore it seems reasonable to expect saturated trapping in PAS studies.

Defect size
A third explanation for the broadening of the momentum distribution has been given in chapter 2 and involves the dependence of the S-parameter on the defect size. A decrease in the S-parameter could correspond to a decrease in average dominant open volume defect, which creates a broadening in the momentum distribution. The decrease of the open volume size with increasing R could be either due to a decrease in the average number of silicon atoms missing in one defect, or it could be that the number of missing silicon atoms stays the same but the vacancy is party filled with hydrogen atoms.

In the remainder of this report, when it is stated that the average open volume increases, this implies that either a bigger number of Si-atoms is missing per vacancy, for example through agglomeration of smaller vacancies, or (also) that hydrogen atoms are released near the vacancies - or that in some other way the average open volume per missing Si-atom changes. The other way around, when it is stated that the open volume decreases, this could also mean that more hydrogen is added in the neighbourhood of the vacancies.

The S-values obtained for the R-series fall in the range typical for a divacancy as the dominant vacancy size.

4.1.2 Annealing studies on R=5 and the high pressure sample
An isochronous DB-PAS annealing experiment has been performed on the sample R=5 of the R-series and on the high pressure sample in addition to the earlier annealing experiments on the R=0 (Melskens[16]) and R=10 (Vullers[44]) samples. During the annealing experiment, the sample was kept at the annealing temperature for an hour, allowed to cool down until it was below 50^{o}C, and measured afterwards. The annealing temperature was stepwise increased from 50^{o}C to 800^{o}C in steps of 50 ^{o}C.

The annealing studies were carried out in order to investigate whether the change in the a-Si:H nanostructure can be observed from the variations in the S- and W-parameters as a function of temperature.

Fitting model

The fitted S- and W-depth profiles at all annealing temperatures are shown for both the R=5 sample and the high pressure sample in Figures 4-2 and 4-3. We first discuss the shape of the observed depth profiles and their fitting analysis.

In all the depth profiles, between 0.1-1 keV the near-surface behaviour of the

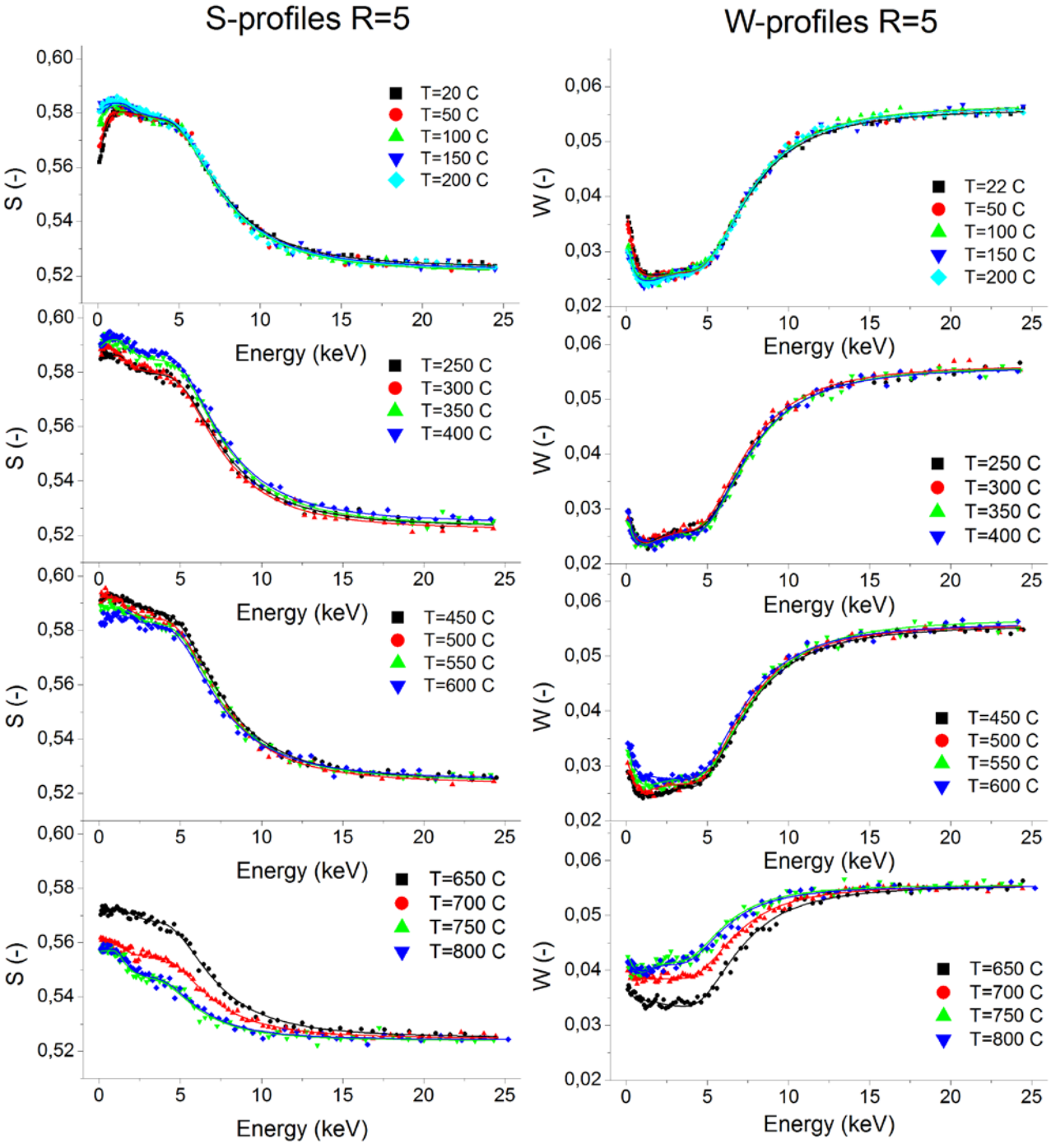

Figure 4-2. Individual S- and W-parameter depth profiles from the annealing DB-PAS experiment on the R=5 sample.

positrons can be observed. From 1-5 keV a plateau is seen, which is caused by the presence of the a-Si:H layer of around 400 nm in thickness (see Figure 3-6b for a picture of the model with film and glass layer). The glass layer region can clearly be distinguished from 20 keV.

For both samples the a-Si:H plateau is not always flat. For example for R=5 the plateau starts out quite flat at 20°C, but at 250°C the first part of the plateau, at energies of 1-2 keV, clearly reaches a higher S-parameter than the second part of 2-5 keV, indicating a change in nanostructure with depth. In case of the high pressure

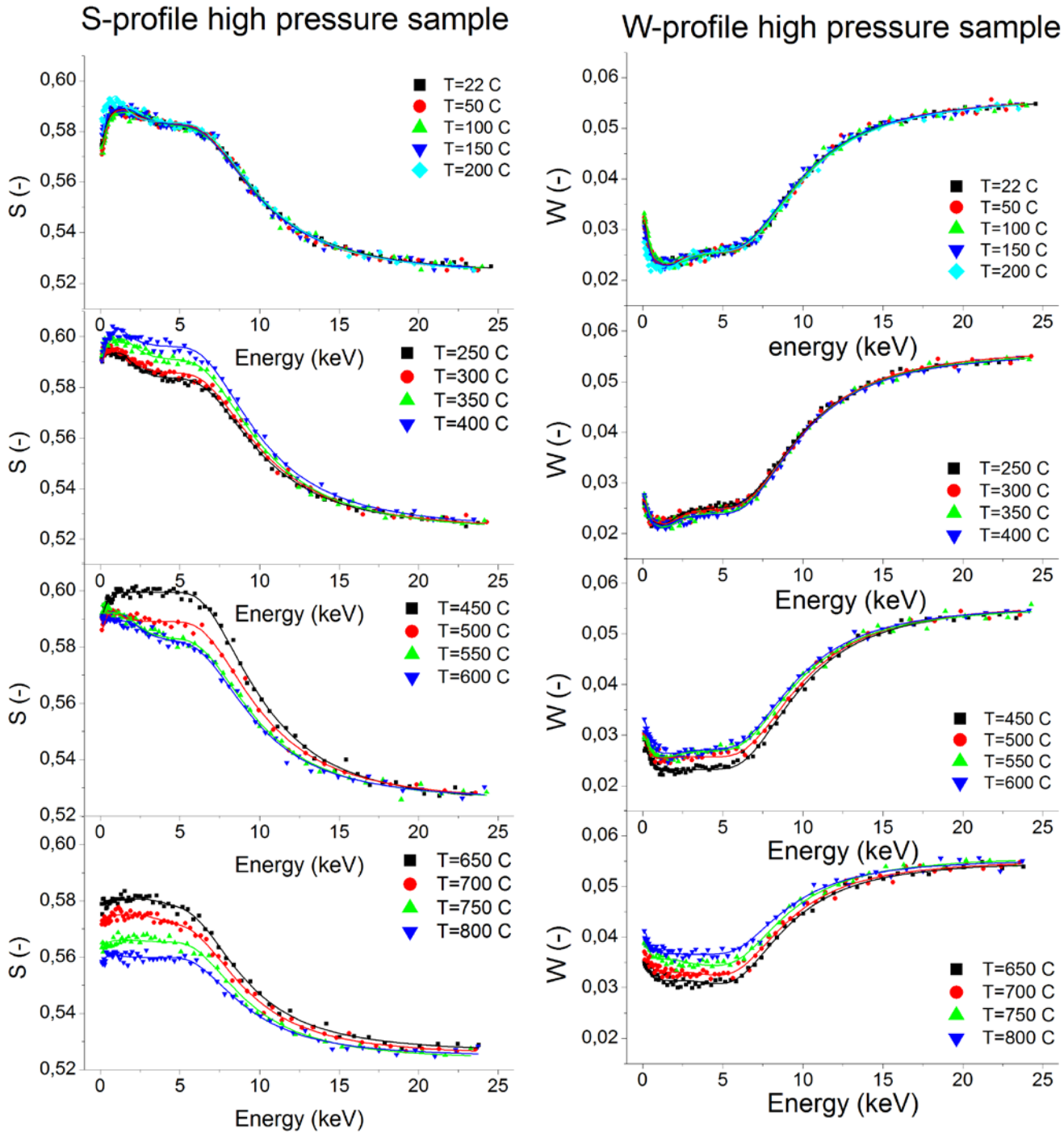

Figure 4-3. Individual S- and W-parameter depth profiles from the annealing DB-PAS experiment on the high pressure sample.

sample, already at room temperature the a-Si:H layer does not show homogeneous S- and W-profiles. These observations have resulted in the choice to carry out all the fits assuming the a-Si:H layer consists out of a top layer and a bulk layer. This is the most simple model for fitting the depth dependence and results in a good description for the obtained Doppler depth profiles. However, at least part of the double layer feature turned out to be caused by the use of the oven, as we will discuss below.

To check whether the depth profiles measured inside and outside the oven give comparable results, both profiles are plotted for each sample (Figure 4-4). It is observed that the plateau corresponding to the film does not have the same shape for the two different measuring conditions. For energies > 3keV there seems to be a

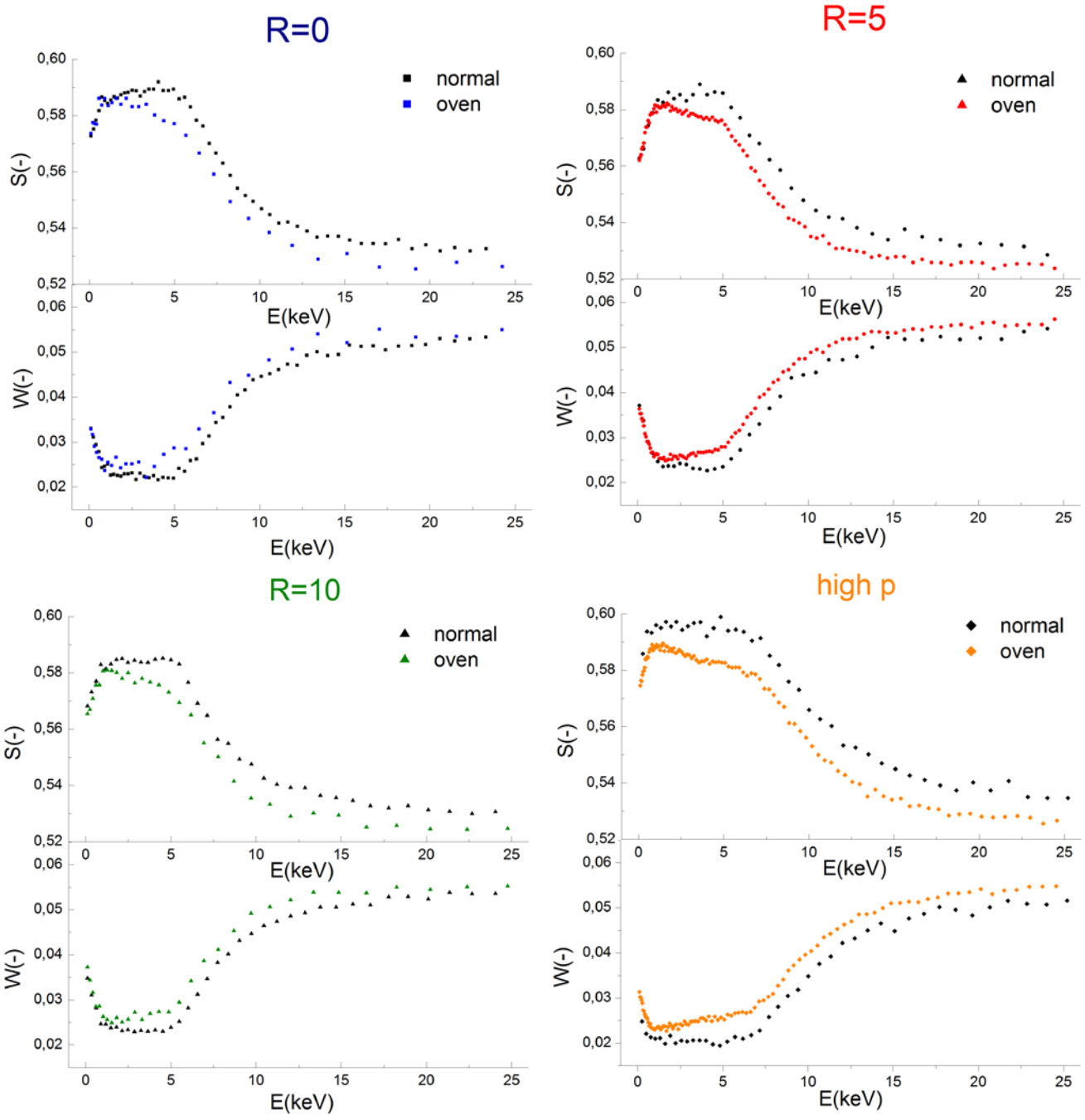

Figure 4-4. Comparison of DB-PAS depth profiles for samples R=0, 5, 10 and the high pressure sample, measured inside and outside of the oven.

constant shift in both the S&W-profiles. Therefore the focus in the analysis will be on the obtained bulk parameters which, after normalization with the c-Si reference S&W parameters, gives the best indication for the S- and W-parameters of the film layer. S and W obtained for the top layer will also be studied to observe the trends upon annealing. These top-layer trends seem to be reliable since the observed differences in Figure 4-4 are similar for each of the samples. Possible explanations for the different depth profiles in the normal and oven settings include the Compton effect and backscattering effects, as will be explained in more detail in Appendix A2-1.

Turning back to Figure 4-2 and 4-3, an interpretation will now be given. At temperatures up to 200^{o}C very little happens to the bulk and glass layers of both samples. A slight difference in shape of the top layer is observed. This could mean that the vacancies or the hydrogen start to become mobile.

Comparison of all DB-PAS annealing studies on R=0,5,10 and the high pressure sample

The S- and W-parameters for the top- and bulk-layers of the R=5 and high pressure sample are compared to the results of earlier annealing experiments that were performed on R=0 and R=10 samples. These annealing experiments were performed by Jimmy Melskens and Albert Vullers, respectively. The latter sample is also part of the R-series of section 3.4; the R=0 sample is from an older batch (M1096), but was deposited in a similar manner. The normalized S- and W-values of the top and bulk layer are shown in Figure 4-5a and 4-5b respectively.

In Melskens[16], three processes were identified: vacancy agglomeration, hydrogen effusion and crystallization. For each of these processes we will see whether or not the earlier observations for R=0 are similar to by the new DB-PAS annealing results. Furthermore, we will see whether differences in behaviour can be observed for the samples that have different hydrogen dilutions but otherwise strongly resemble each other.

Process I: Vacancy agglomeration

For all four samples, a gradual increase of the S-parameter is observed to occur at least up to 400 - 450 ^{o}C. The increase is observed for both the top and the bulk layer and is accompanied by a decrease in the W-parameter. The increase in S and decrease in W is associated with an increase of the average open volume size. The size of the open volume can grow when vacancies already present in the material become mobile and agglomerate. Together all the observed trends described above form a strong case for the occurrence of vacancy agglomeration.

In the theory chapter some approximate relations are given for typical values for S-parameter and the corresponding type of open volume defect. These numbers form the basis for the coloured regions displayed in Figure 4-5.

In Table 4-1 some indications are given for the defect sizes of the annealed samples, both in the as-deposited state and after annealing, when the defects are the biggest. For the high pressure sample, nanosized voids seem to be created during the annealing process.

Table 4-1. Indication of the size of the dominant defects at the bulk of the film based on the evolution of the S-parameter during the DB-PAS annealing experiment for all four samples R=0,5,10 and the high pressure sample.

	Initial dominant defect	Max. dominant defect after annealing
High p	Divacancies	Nanosized voids
R=0		Multivacancies
R=5		
R=10		

For all samples the S-parameter first increases in the range up to 400°C and eventually S decreases, along with opposite behaviour of the W-parameter. The decrease starts to take place from T=400°C for most samples, and from T=550°C for the R=10 material. If S decreases, one cause could be that the average vacancy size decreases. This can happen by release of large vacancies at the surface. This release must happen at a faster rate than the agglomeration of smaller vacancies, since that process would cause a further increase in S.

For sample R=10, a plateau can be observed for the S- and W-values from 400°C - 550°C for both the top and the bulk layer. This plateau is not present for the other samples. The average open volume size seems to stay constant among this temperature range, while for the other samples the average size already decreases. This could mean that the vacancies in the R=10 material are less mobile, and more energy is needed to move the vacancies to the surface. Or it could mean that somehow the balance between the disappearance of vacancies and renewed vacancy agglomeration is maintained longer. In those cases the release of the vacancies at the surface then must be happening slower than for the other samples, in other words, the plateau could indicate that the R=10 material is more stable than the other samples are.

Process II: Hydrogen effusion

From FTIR experiments it was concluded that the hydrogen effuses out of sample R=0 starting from T= 300°C up to temperatures of ~500°C[16]. From T = 400°C, the effect of H-effusion is also visible from the DB-PAS annealing graphs: at T = 400°C and T = 600°C the R=0 sample has an increasing W while S stays constant. This means that the average open volume size stays constant while the probability for annihilation with a core electron increases.[48] For R=5 and R=10 we also observe an increase in W from T=400°C. The S-parameter at the same time stays almost constant. For R=5 for example in the bulk layer the S-parameter goes up at T=400°C and then down again at 450 °C. This indicates that the hydrogen effusion takes place for R=5 and R=10 at around T=400°C as well.

The high pressure sample shows behaviour that differs from the other samples at around 400-450°C. First S increases (along with a decrease of W), up to 400°C for the top layer and up to 450°C for the bulk layer. This is directly followed by a sharp decrease of S and increase of W. From Figure 4-7 it is also clear that the processes taking place in the high pressure sample are different: for the other samples the (S,W) curves are a bit round, but for the high pressure sample the curve is sharp. For the samples with R=5 and R=10 (and possibly also R=0) three processes can be identified

from these (S,W) curves based on the trends observed for both the top- and the bulk layer. For the high pressure sample it could be either two or three processes, but in any case we see that the line segment in Figure 4-7, that starts at around T=400^{o}C, has a very different direction, when compared to the line segments of the other curves for process II.

The FTIR measurements on R=0 also show that at T=500^{o}C all the Si-H bonds in the material are broken. However according to H-effusion measurements performed by Beyer on a similar sample series there is still hydrogen present in the material at this temperature, seeing has he finds two broad effusion peaks, one at around 400^{o}C and one at around 600^{o}C. The hydrogen needs some time/energy to reach the surface and be released. In the meantime, the hydrogen may be found inside the vacancies in the form of molecular hydrogen, or it may travel through the material interstitial. The presence of molecular hydrogen in small vacancy clusters will have influence on the S parameter and on the size of the open volume defect found.

Process III: Crystallization

From 600^{o}C up to 750^{o}C we observe a strong decrease in S and increase in W with an almost constant steepness. The steepness seems to increase with increasing hydrogen dilution both for the top- and the bulk-layer, implying that the steepness is characteristic for the hydrogen dilution of the sample. The high pressure sample also shows a constant steepness in the same temperature range. The influence of hydrogen on the behaviour of the sample is therefore still found visible at these high temperatures and it appears that not all hydrogen has left the sample yet. This is consistent with information from hydrogen effusion measurements on similar samples. For example, in Beyer[19], two peaks of H-effusion are measured, one at around 400^{o}C and one at around 600^{o}C.

For R=5 and R=10 we see that at T$\geq$750^{o}C values of S<1 and W>1 are reached while $S \geq 1$ and $W \leq 1$ characteristic for c-Si with small concentrations of vacancies would be expected, seeing as the samples have crystallized. This effect has been attributed to oxygen-related defects[49]. In the present case, the oxygen can come from a small oxide layer that was there on top of the sample, or from the glass substrate. S can also decrease due to a gas filling of the voids in the material, but not below 1. A gas pressure on the order of a few 100 kbar results in S=1.[2]

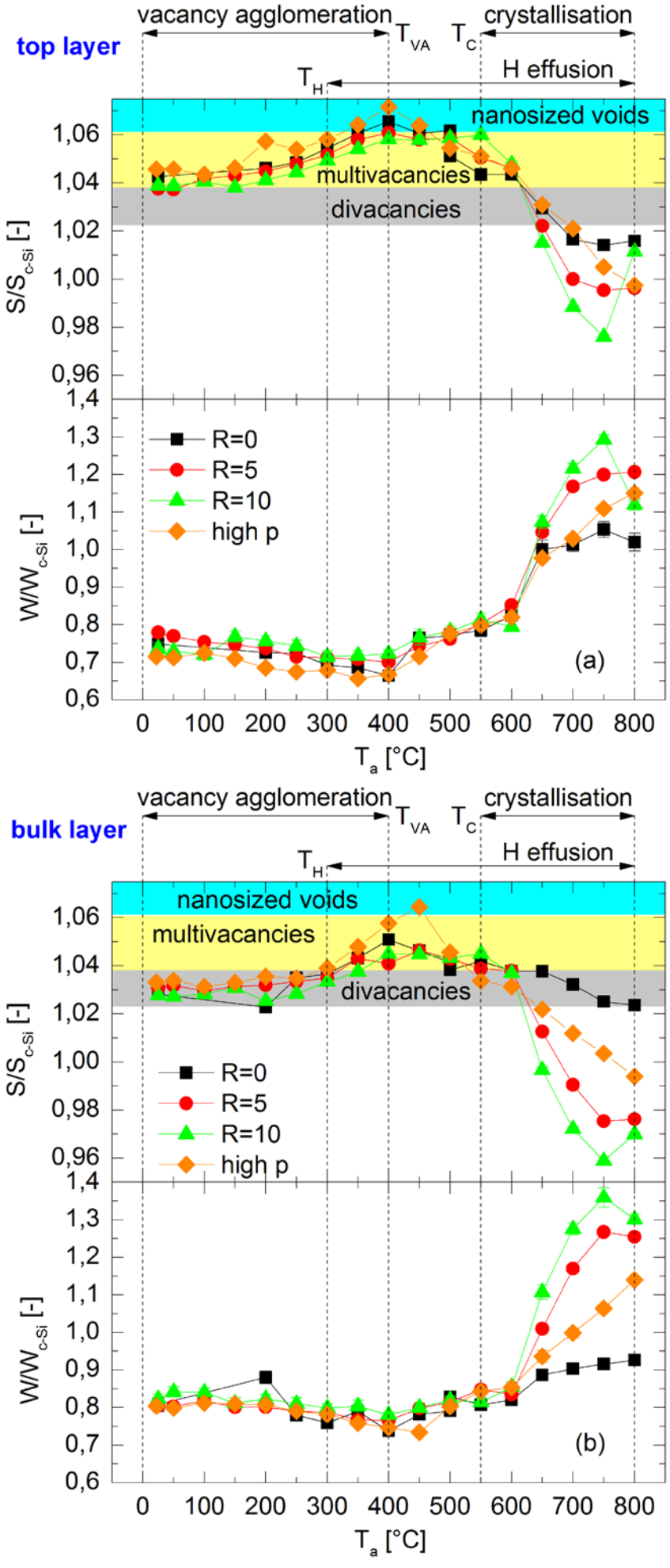

Figure 4-5:
(a) top- and (b) bulk-values for the normalized S- and W-parameters as fitted for the top and bulk layer for each temperature step of the annealing experiment, compared for all four samples R=0,R=5 and R=10 and the high pressure sample. The error bars shown are the fitting errors.

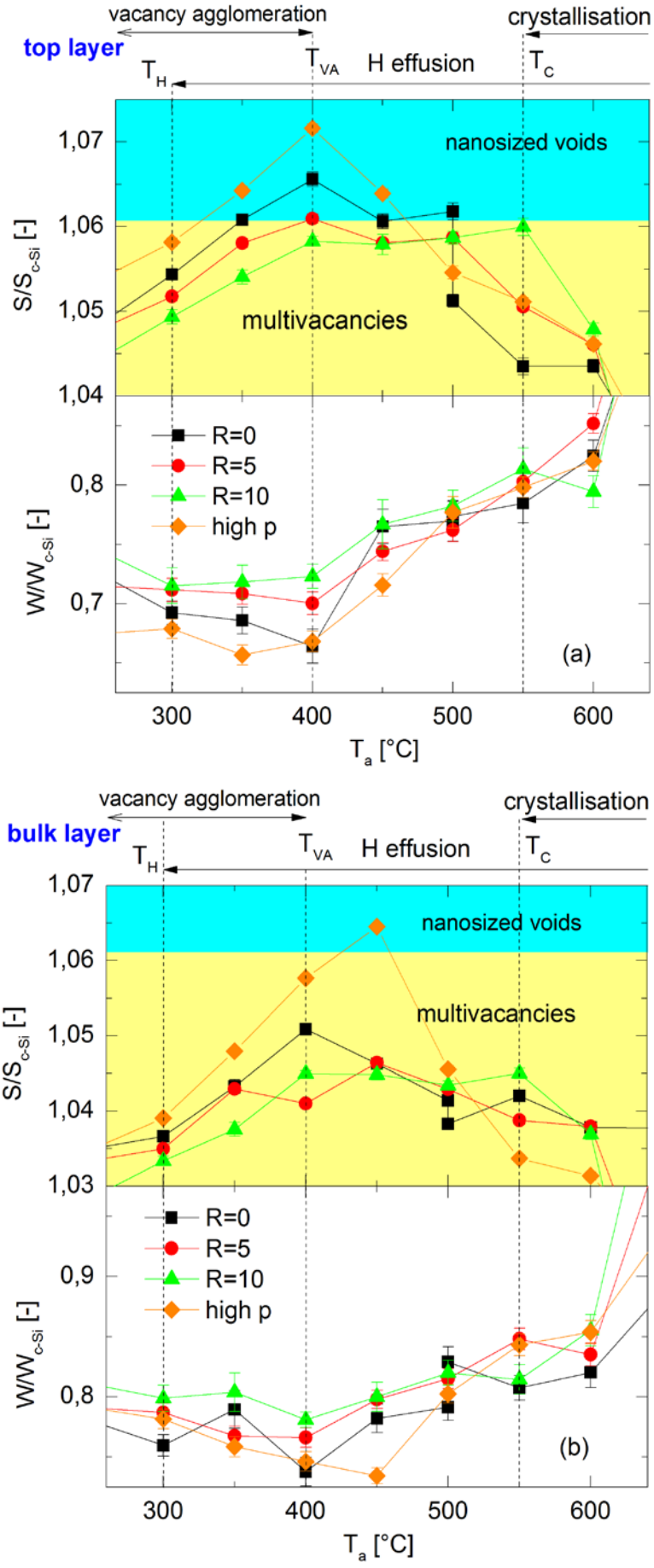

Figure 4-6. Zoom-in on the previous figure, for (a) the top-layer and (b) the bulk layer.

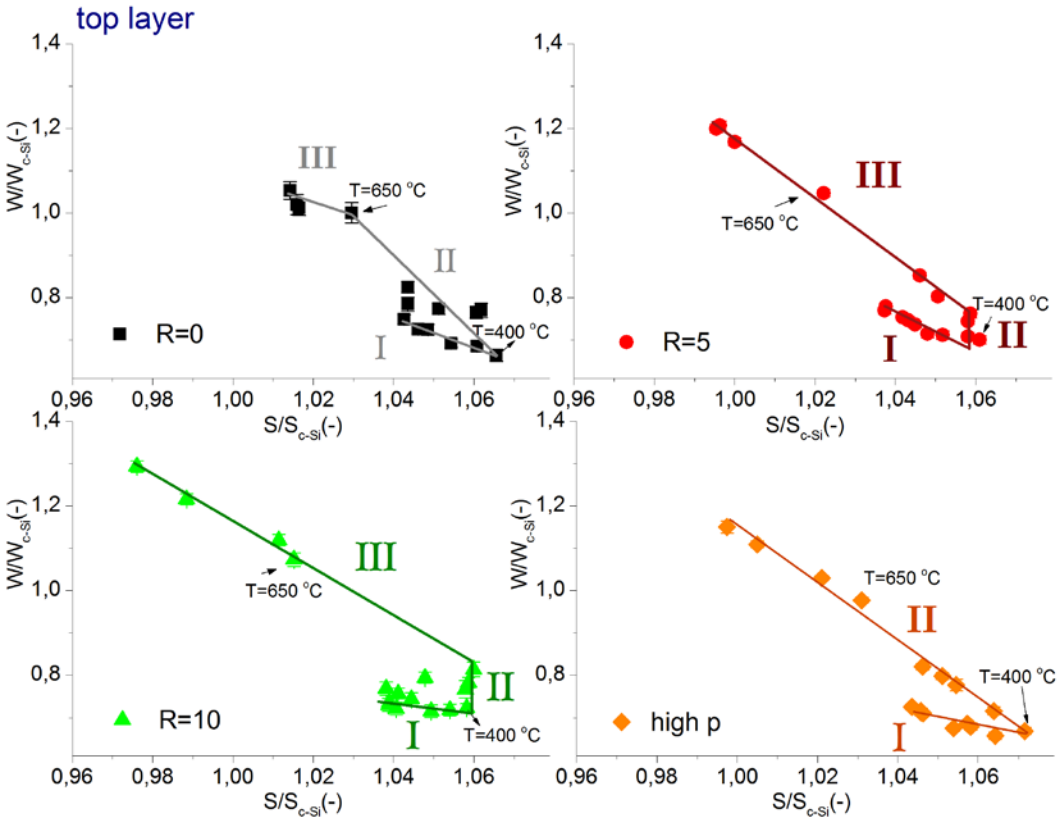

Figure 4-7a. (S,W) plot for the top layers for R=0,5,10 and the high pressure sample, as a function of the annealing temperature T_a

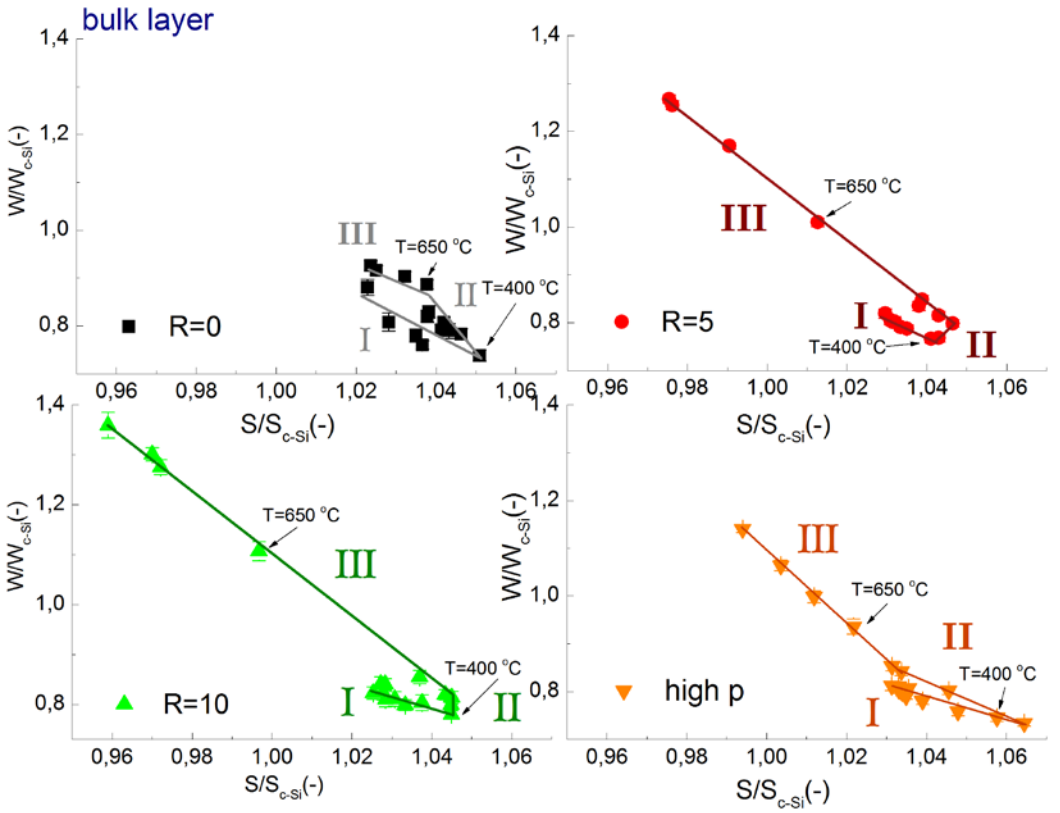

Figure 4-7b. (S,W) plot for the bulk layers for R=0,5,10 and the high pressure sample, as a function of the annealing temperature T_a.

DB-PAS on diode/triode samples

DB-PAS measurements are performed on the diode/triode series, which is a sample series that consists of a-Si:H absorber layers fabricated in Japan using an adjusted deposition method as described in the experimental introduction, that has shown promising properties when used in solar cells. The depth profiles are measured and compared to the external solar cell parameters in order to find out whether there is a relation between the nanostructural parameters S and W and good solar cell material properties, in particular the stability against light soaking.

In section 3.4 we already saw that the triode-deposited solar cells show the best efficiencies. One-layer fits of the depth profiles were performed using VEPFIT with good results (see Appendix A2-2). As an example, the fit of sample T09_5 is also the example depicted in Figure 3-6a. The resulting normalized S- and W-parameters are shown in Figure 4-8. The (S,W)-plot looks linear. The triode samples have a lower S-parameter and higher W-parameter than the diode samples. For both series, the R=7 samples shows the lowest S and highest W.

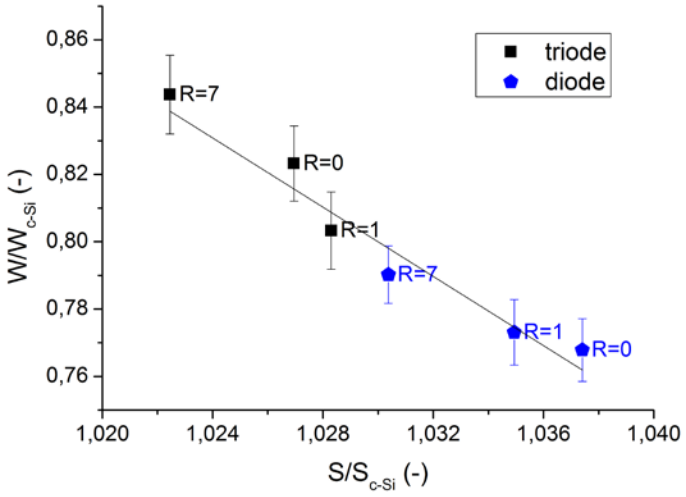

Figure 4-8 (S,W)-plot as measured and fitted using DB-PAS for the diode/triode samples. The line is a guide to the eye.

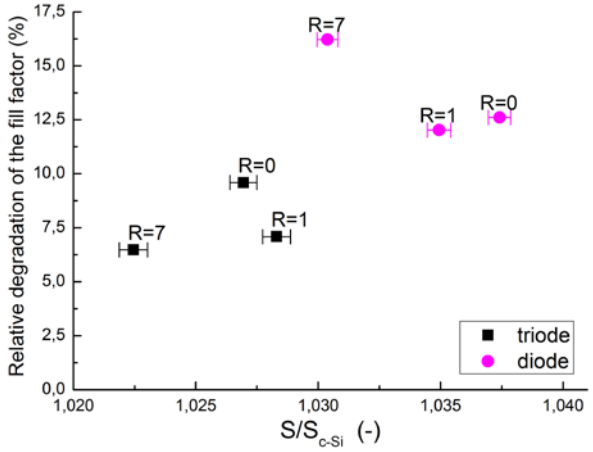

Figure 4-9. Relative degradation of the fill factor due to light-soaking of the solar cell, as a function of S.

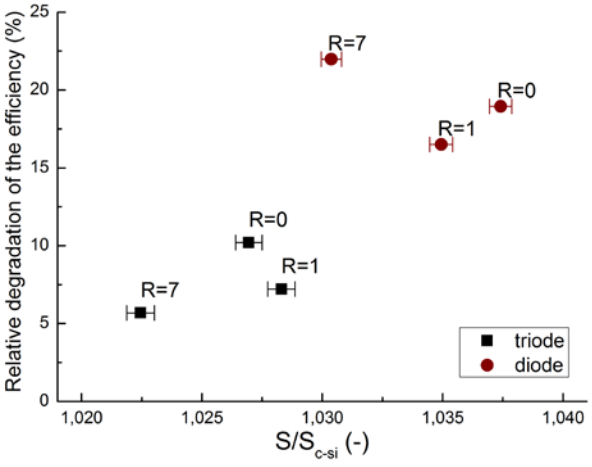

Figure 4-10. Relative degradation of the efficiency of the solar cell as a function of S, due to light-soaking.

In general, it appears that there exists a relation between the suitability of the a-Si:H layers for use in solar cells and the nanostructure parameters; now we want to see which properties of the layers and solar cells show the most correlation with these parameters. In particular, we investigated the correlation between stability against light-soaking versus the Doppler S-parameter.

Figure 4-9 shows the comparison of the extracted S-parameter and the relative degradation of the fill factor, and Figure 4-10 shows the same for the relative degradation of the efficiency.

From Figure 4-9, there seems to be a correlation between a low S-parameter of the absorber layers and a low fill factor degradation of the corresponding solar cells. It seems that the degradation of the fill factor is less for materials with smaller open volumes.

When we compare the fill factor graph with the efficiency graph, some small differences can be observed. The fill factor contains information about the internal resistances in the solar cell and the efficiency parameter reflects the total solar cell's performance. The observed differences between the efficiency and fill factor degradation means that the a-Si:H layer is not the only spot where degradation takes place in the solar cell.

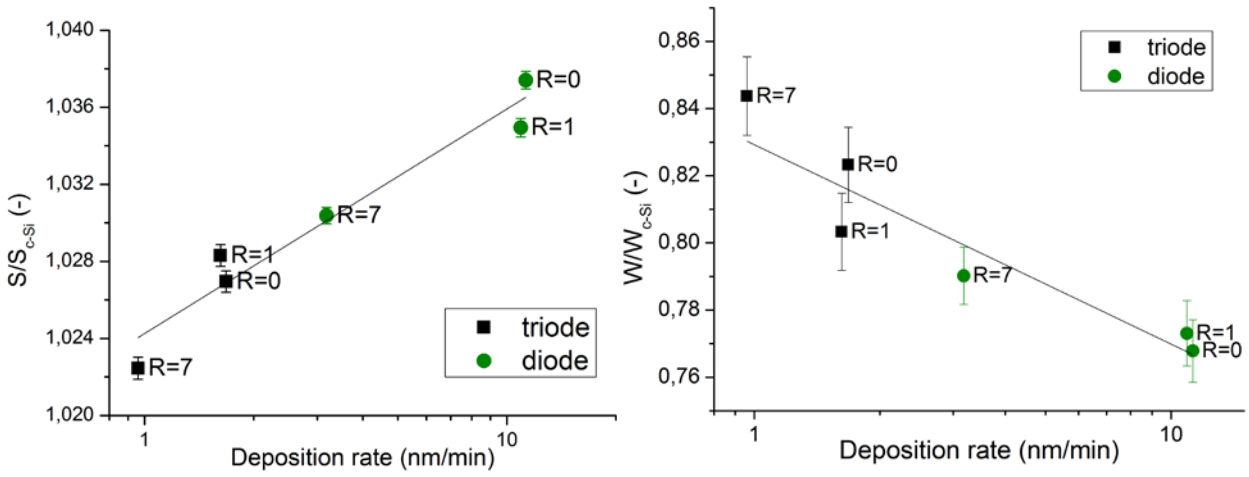

Figure 4-11. Dependence of S- (left) and W- (right) parameter on the deposition rate of the a-Si:H film. The lines are guides to the eye.

Figure 4-11 shows the fitted S- and W-parameters of the absorber layers, versus the deposition rates of these layers. There seems to be an logarithmic dependence between the deposition rate and the nanostructural parameters. It therefore appears that the lower S- and higher W-parameters can mainly be attributed to the lower deposition rates. A lower S and higher W could be caused by a decrease in the average defect size or in the defect density, which could be a result of the lower deposition rate. When the deposition rate is high, the atoms do not always have the time to find their equilibrium spots within the lattice. Thereby defects can more easily occur, and the open volume sizes can be bigger even when the number of vacancies is the same, because some of the deposited atoms induce more stress in the a-Si:H matrix. It could even be that for low deposition rates, the only open volume defects

that occur are divacancies, whereas for higher deposition rates, tri- tetra- and multivacancies also occur.

Sample thickness and density

Table 4-2. Diode/triode sample thicknesses as determined from RT and DB-PAS measurements, including their fitting errors.

Sample	Thickness (nm) RT measurements	Thickness (nm) VEPFIT	Error (nm) VEPFIT
Triode R=1	391.7	399	1
Triode R=7	390.2	373	5
Triode R=0	444	464	6
Diode R=1	289	310	3
Diode R=7	552.1	576	5
Diode R=0	363.6	376	3

The thicknesses of diode/triode samples have been determined using RT-measurements and also by fitting the DB-PAS results in VEPFIT. The results are shown in Table 4-2. The VEPFIT thicknesses have been determined assuming $\rho_{film} = 2.20 g/cm^3$. The thicknesses obtained from VEPFIT analysis are similar to those obtained from the RT-measurements.

4.2 2D-ACAR and CDB measurements

In this subsection the dependence of the momentum distribution $N(p_x)$ on the hydrogen to silane ratio R and the annealing temperature T is studied using 2D-ACAR measurements. Their momentum distributions and autocorrelation functions are analysed, where the latter are used to acquire direct spatial information on the a-Si:H nanostructure. The 2D-ACAR measurement on the annealing series is also combined with coincidence Doppler broadening measurements (CDB) in order to further study the S- and W-parameter dependence.

4.2.1 2D-ACAR on the R-series

Following the DB-PAS experiment on the samples with R=0 up to R=10 the shape of the electron momentum distributions of the same samples is studied in more detail. We do this using 2D-ACAR measurements, which have a better resolution. The momentum distributions of the R-series are measured using an initial positron energy of 3.7 keV to ensure that the positrons annihilate in the bulk of the layer. The sample R=10 is also measured after annealing to 800°C. Raman and XRD measurements have shown that this sample has completely crystallized after annealing. However, from the data analysis as explained in section 3.1, the 2D-momentum distribution still appears to be isotropic, and so are all the 2D-momentum distributions for R=0 up to R=10. The 1D-projections of the resulting distribution functions are calculated as described in section 3.1, and are shown in Figure 4-12. The count rates for each measurement is given in Appendix A1-1.

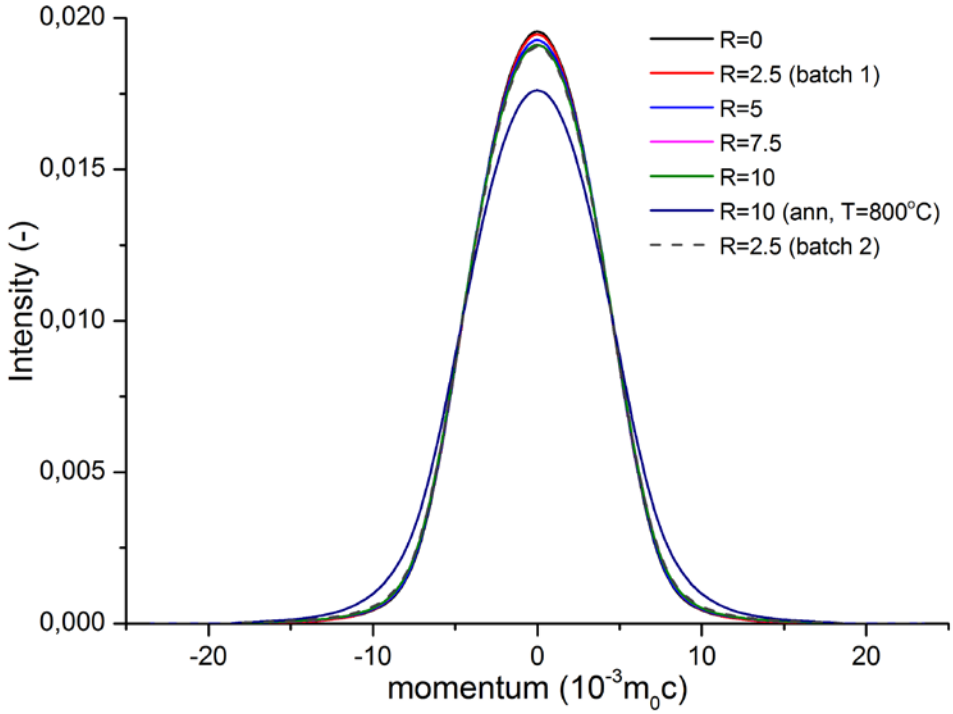

Figure 4-12. 1D-projection of the 2D-ACAR electron momentum distribution for a-Si:H samples with various hydrogen dilutions. Initial positron energy of 3.7 keV.

Already from this figure, some slight differences in shape between the samples are visible. The peak height seems to decrease with increasing R. The annealed sample shows a clear broadening of the momentum distribution. To observe the trends in the high-momentum regime, the distribution functions are normalized with respect to the 1D-ACAR distribution of the R=0 sample, as shown in Figure 4-13. With increasing

R we observe an increase in the high momentum intensity. The R=2.5-sample from batch 1 deviates from this trend: for $|p| > 12 \cdot 10^{-3} m_0 c$ the intensity becomes lower than that of the R=0 sample. Another R=2.5 sample from a different batch was also measured using 2D-ACAR. It is found that the high-momentum intensity gets higher, even beyond the intensity of the 1D-ACAR distribution of R=10. Based on this result it seems that samples produced in different batches, measured a few months in between, cannot always be compared so well.

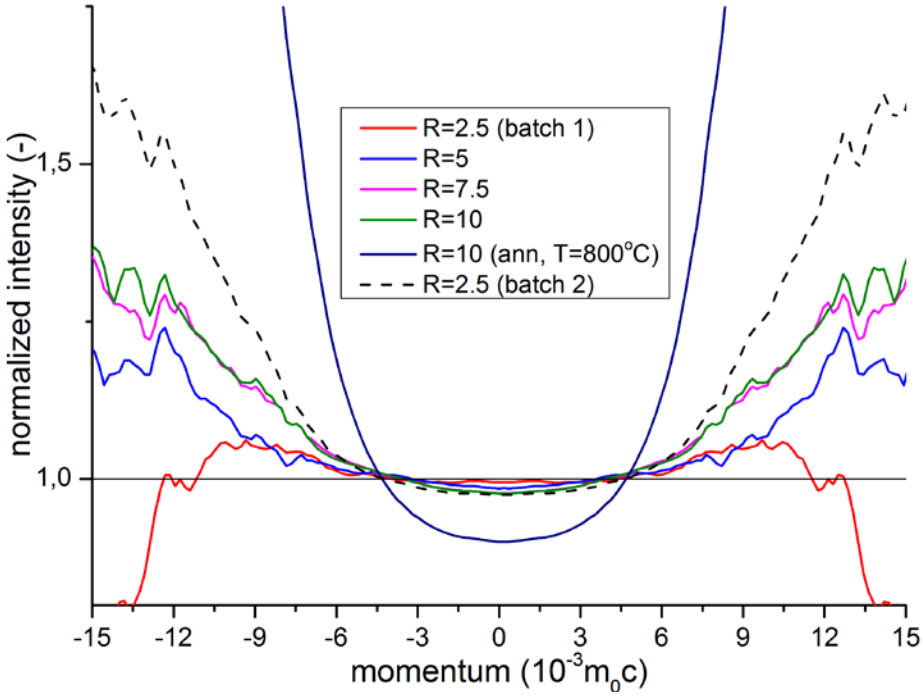

Figure 4-13. The electron momentum distributions, normalized on the R=0 distribution in order to be able to observe their mutual differences better.

In Figure 4-14 the (S,W) plot corresponding to the 2D-ACAR measurements is shown. The general trends observed with DB-PAS for S and W as a function of hydrogen dilution, indicating a broadening of the momentum distribution, are confirmed here.

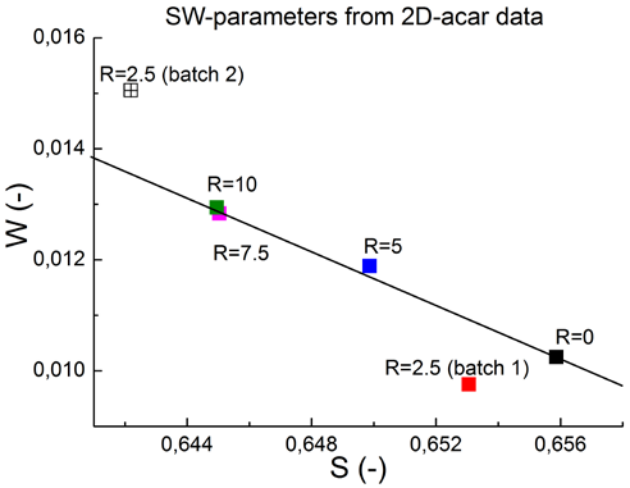

Figure 4-14. (S,W)-plot as computed from the 2D-ACAR data. The line is a guide to the eye. Statistical errors are on the order of 10^{-4} for S and 10^{-5} for W.

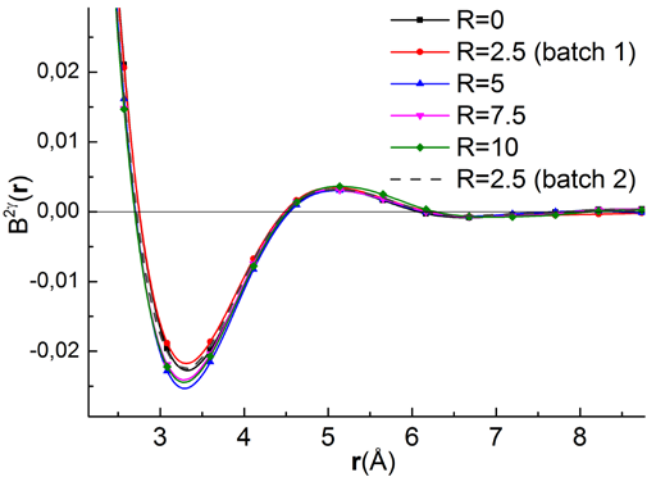

Figure 4-15. Positron-electron autocorrelation functions as computed from the 1D-projection of the 2D-ACAR data.

The positron-electron autocorrelation functions $B^{2\gamma}(r)$ corresponding to the momentum distributions $N(p)$ are calculated as described in section 3.1 and the results for 2Å< r < 9Å including spline interpolation between the data points are shown in figure 13. The differences between the functions are observed to be small. However, some useful information is contained in the first zero crossings of these $B^{2\gamma}(r)$ functions, as we have seen in chapter 2.

Zero crossing

In chapter 2 it was explained that the 1st zero crossing distance contains information about the defect's spatial structure (the distance says something about the average distance between two nuclei near the annihilation event). This fact will now be used to study the dependence of the spatial structure on the hydrogen dilution by determining the 1st zero crossing of each autocorrelation function of Figure 4-15. The zero crossings are determined as described in chapter 3. The results are shown in Figure 4-16, including error bars, which will be discussed in more detail in the next paragraph. The zero crossing of the batch 2 R=2.5 sample is not shown in this figure, since it's S/W values deviate strongly from the general trend, indicating a difference in production method for this sample.

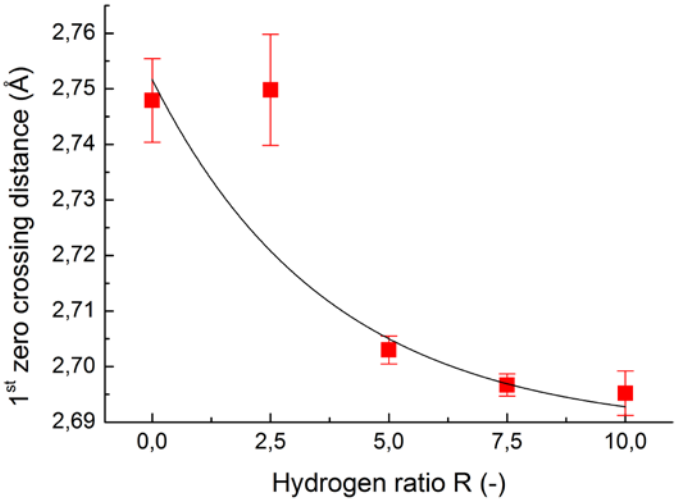

Figure 4-16. The 1st zero crossing distances for the ACF as a function of samples hydrogen to silane flow ratio during deposition. The line is a guide to the eye.

The calculated zero crossings agree with what was found by Britton et al.[50] who reported 2.75Å for the first zero crossing distance for their hot-wire chemical vapour deposition (HWCVD)-deposited a-Si:H sample. Ho et al.[35] found values for the zero-crossings in the range of 2.5-3Å for defect-free Si and P-doped Si (used to study the E-center defects) for 2D-ACAR measurements depending on the crystal orientation/ lattice plane.

From Figure 4-16 a decrease in the 1st zero crossing with increasing hydrogen dilution is observed. This result strongly indicates that the average defect size decreases with increasing dilution. This is in line with what was inferred from DB-PAS on the same series (in section 4.1.1). There a decrease in S and increase in W with increasing R were found, implying a broadening of the momentum distribution as the hydrogen dilution increases. A broadening of the momentum distribution could correspond to a decrease of the average vacancy size.

More support for a decrease in open volume size can be found by looking back at Figure 4-15. It appears that the $B^{2\gamma}(r)$ curves of R=0 and R=2.5 are more damped than the curves for the higher dilutions. This is most clearly visible from the minima of $B^{2\gamma}(r)$ near 3.3Å. An increased damping in $B^{2\gamma}(r)$ indicates that the positron and electron wavefunctions have less overlap, which is expected for bigger open volume trapping centres.

Error analysis on the zero crossings

The error on the 1st zero crossings is expected to be different for each sample measurement, since the counting statistics differ quite a lot from sample to sample. We address the error analysis as follows. The data collected for one sample is divided into two equal parts, called A and B. For each part $B^{2\gamma}(r)$ is calculated and spline-interpolated. To avoid effects due to changes in the setup with time, the data files collected in odd hours are assigned to $B^{2\gamma}(r)$ part A and those in even hours are assigned to $B^{2\gamma}(r)$ part B. Subsequently the interpolated $B^{2\gamma}(r)$ part B is divided by $B^{2\gamma}(r)$ part A, resulting in the curves of Figure 4-17, which give an impression of the measurement error. Deviations from the quotient of 1.0 in this figure are a measure

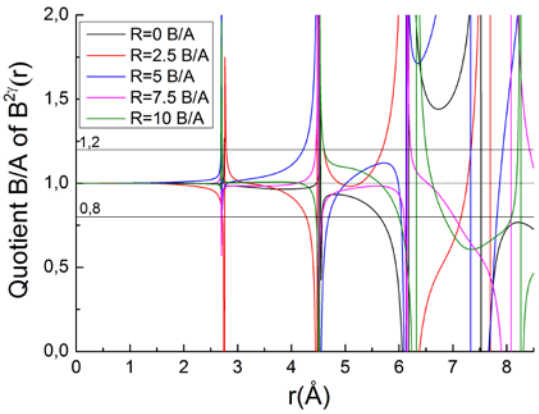

Figure 4-17. Research the accurateness of $B^{2\gamma}(r)$. Figure shows the ratio of the $B^{2\gamma}(r)$ computed from the two halves of the data. All R are from the same batch.

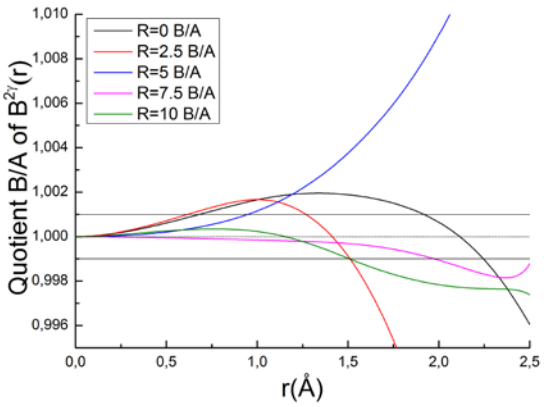

Figure 4-18. Zoom in of figure 15.

for the relative inaccuracies of the full $B^{2\gamma}(r)$ for each sample. The inaccuracy increases with the distance *r*. In the distance range prior to the 1st zero crossing at around 2.7Å, the inaccuracy is as low as 0.2% as can also be seen from Figure 4-18. Beyond the 2nd zero crossing at around 4.5Å, the deviation is on the order of 20% or larger so that the $B^{2\gamma}(r)$ data from that point on cannot be reliably used.

Based on this information on the relative error, it was decided to only use the 1st zero crossing to gain insight in the dependence of the size of the open volume defect with R and temperature. In order to estimate the error, the zero crossings of all three autocorrelation functions $B^{2\gamma}(r)$ are determined (part A, part B and the full function) and their mutual differences are calculated. The differences are used to estimate the error in the value for each 1st zero crossing. The results of this methodology are shown in Table 4-3.

Table 4-3. Error estimation on the first zero crossings for samples R=0 up to R=10. For each of the three autocorrelation functions (A, B and the full function) the 1st zero crossings and the mutual differences are listed.

sample	**Which $B^{2\gamma}(r)$?**	**R=0**	**R=2.5**	**R=5**	**R=7.5**	**R=10**
units		Å	Å	Å	Å	Å
1st zero crossing	A	2.7527	2.7550	2.7015	2.6969	2.6984
	B	2.7530	2.7476	2.7035	2.6980	2.6972
	Full ACF	2.7479	2.7498	2.7030	2.6967	2.6952
Difference between all the zero crossings	A-B	-0.0003	0.0074	-0.0020	-0.0011	0.0012
	B-Full ACF	0.0051	-0.0022	0.0005	0.0013	0.0020
	Full ACF-A	-0.0048	-0.0052	0.0015	-0.0002	-0.0032
Error estimate		0.0075	0.01	0.0025	0.002	0.004

4.2.2 2D-ACAR on the T-series

A 2D-ACAR isochronous annealing series was measured in-situ on an R=5 sample (M1583 in this case) in order to find the momentum distributions and autocorrelation functions at a constant positron implantation energy of 4.1 keV, to monitor the nanostructural changes in the bulk of the film. During the annealing experiment, the sample was kept at the annealing temperature for an hour, allowed to cool down, and measured afterwards. We want to exploit the higher resolution of these measurements to calculate the autocorrelation functions and look at the shift in their 1st zero crossings, just as was done for the R-series, in order to look more directly at the temperature evolution of the defect size. Also, we want to see whether the S- and W-trends that are found with DB-PAS can be confirmed using ACAR-measurement. A confirmation would make a stronger case for vacancy agglomeration theory. The S- and W-parameters are determined both from the momentum distributions and also from simultaneous coincidence Doppler Broadening measurements (CDB).

The 1D-momentum distributions are shown in Figure 4-19a, along with the normalized momentum distributions w.r.t. the as-deposited momentum distribution in Figure 4-19b. The count rates for each measurement are given in Appendix A1-2. A comparison of Figures 4-12 and 4-13 to Figure 4-19 clearly shows that the differences between the T-measurements are smaller. This is also visible from the scale of the normalized momentum distributions. The momentum distribution clearly narrows,

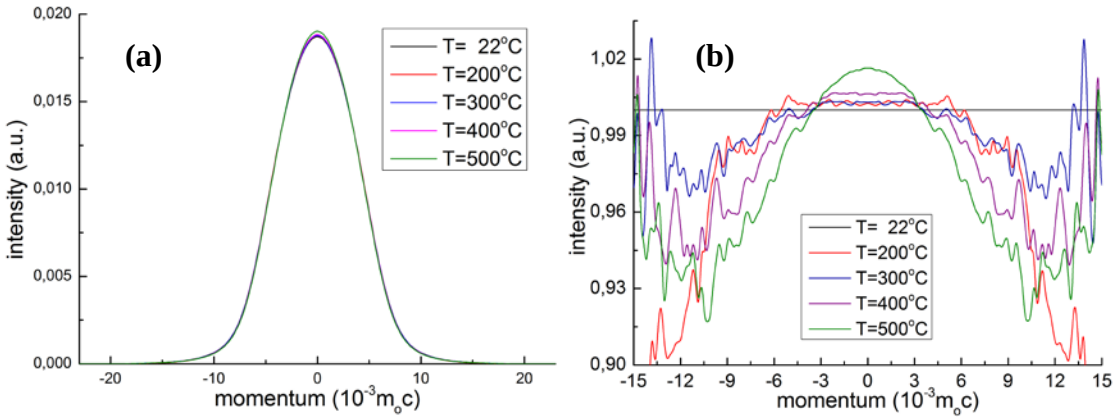

Figure 4-19. (a) Temperature dependent-momentum distribution of R=5 (sample M1583) and (b) normalized momentum distribution as measured on the ACAR using the POSH beam. Positron implantation energy of the positrons 4.1 keV.

which could indicate an increase in the average open volume.

For the normalized momentum distribution of T=500°C the narrowing is extra clear: in the low momentum regime of $|p| < 3 \cdot 10^{-3} m_o c$ a peak is still visible after having divided by the room temperature momentum distribution, indicating a sharper peak for the T=500°C distribution. For the other temperatures, 200, 300 and 400°C, judging from the flat curves for low momenta in Figure 4-19b, it appears that only the intensity of the peak changed with temperature and not the shape.

Figure 4-20 shows the spline interpolated positron-electron autocorrelation functions $B^{2\gamma}(r)$, and in Figure 4-21 the corresponding 1st zero crossings and their estimated errors are depicted. These errors are estimated in the same way as was done for the R-series. Figures showing the quotient graphs of the ACFs Part A and B can be found in the appendix. In Figure 4-21 we see that the 1st zero crossing distance increases with the annealing temperature. For T=500°C the increase is very clear, while at the lower temperatures there is the suggestion of a trend, surrounded by error bars that are too wide to be conclusive.

An increase in 1st zero crossing distance is associated with an increase of the atomic distances near open volume defects. The observed increase suggests that the average open volume size increases with temperature, indicative of vacancy agglomeration or the release of hydrogen near vacancies. This is also in line with the observed increase in the S parameter and decrease in W parameter that were found in the R=5 DB-PAS annealing experiment for similar temperatures.

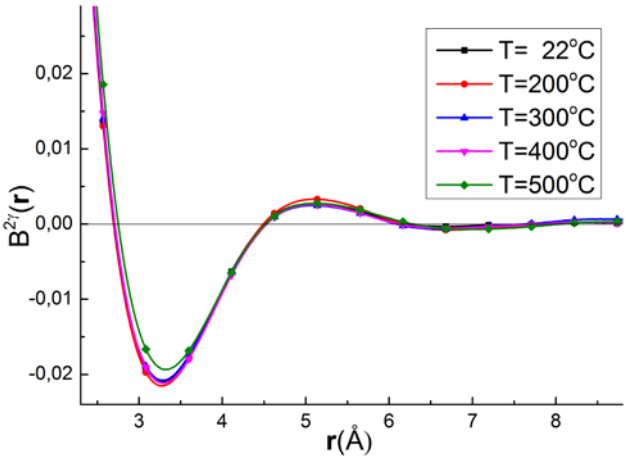

Figure 4-20. $B^{2\gamma}(r)$ extracted from the ACAR electron momentum distribution, obtained by spline interpolation.

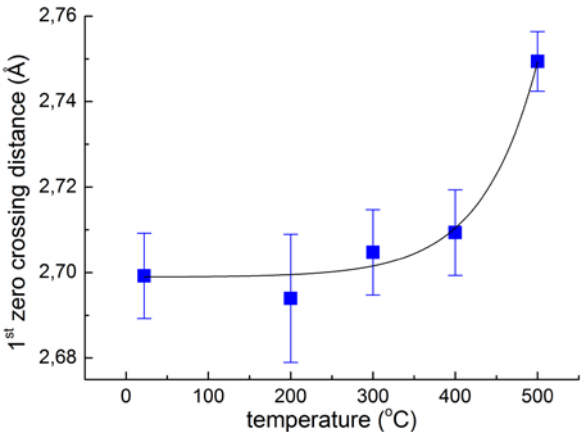

Figure 4-21. First zero crossings of $B^{2\gamma}(r)$ as a function of the annealing temperature. The line is a guide to the eye.

From Figure 4-20 it is visible that $B^{2\gamma}(r)$ for 500°C is more damped than for the other curves. This is most clearly seen from the more shallow minimum of the curve near 3.3 Å. The increased damping is indicative that the positron and electron wave functions have less overlap. This observation supports the conclusion of an increased average open volume.

Figure 4-22 presents the S- and W-parameters determined from the Coincidence Doppler and 2D-ACAR measurements, including their statistical errors. The S and W parameters extracted from the CDB measurements were determined using the same

boundaries as usual. For both methods, an increase in S and decrease in W was observed with increased temperature. These findings are consistent with the DB-PAS

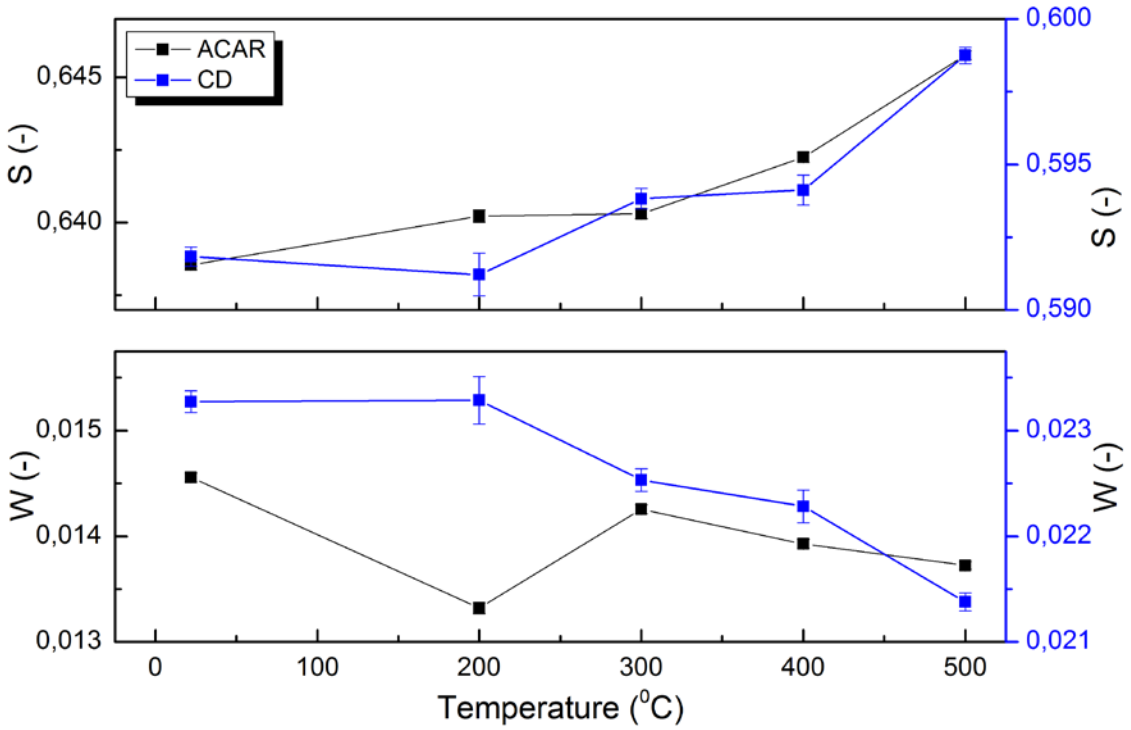

Figure 4-22. Comparison of (S,T) and (W,T) trends as computed from the coincidence Doppler data and ACAR data. Errors shown are the statistical errors.

results.

It is important to see that W decreases for the CD-measurements as with this technique we have less background noise in the high momentum area than in the momentum distributions collected by 2D-ACAR and DB-PAS.

The increase in the 1st zero crossing position for 2D-ACAR along with the S- and W-trends for 2D-ACAR, CDB and DB-PAS all indicate that the average size of the open volumes inside a-Si:H increases with temperature, at least in the regime up to 400-500°C. This is an indication that the vacancies inside the material become mobile and agglomerate to form larger vacancies as a consequence of the annealing treatment.

Calculating the positron binding energy from $B^{2\gamma}(r)$

In chapter 2 we described how Ho et al.[35] used the ACF $B^{2\gamma}(r)$ to estimate the positron binding energy to the defect. They did this by dividing the ACF for the E-center defect by the ACF for defect-free Si, since theoretically it is expected that $B^{2\gamma}_{E-center}(r)/B^{2\gamma}_{c-Si}(r) = e^{-\alpha|r|}$. This division of the experimentally determined $B^{2\gamma}(r)$ functions resulted for them in a graph that is mostly exponentially decaying, except near the zero crossings. By determining the decay coefficient of the graph, the positron binding energy can be extracted, since

$$\alpha = \frac{1}{\hbar c}\sqrt{2mc^2 E_B} \tag{4.1}$$

This same procedure is now used, with the adaptation that the $B^{2\gamma}(r)$ of the annealed sample states are divided by the $B^{2\gamma}(r)$ of the as-deposited state in order to look at the *change* in (average) positron binding energy E_B upon the observed increase of the average open volume size.

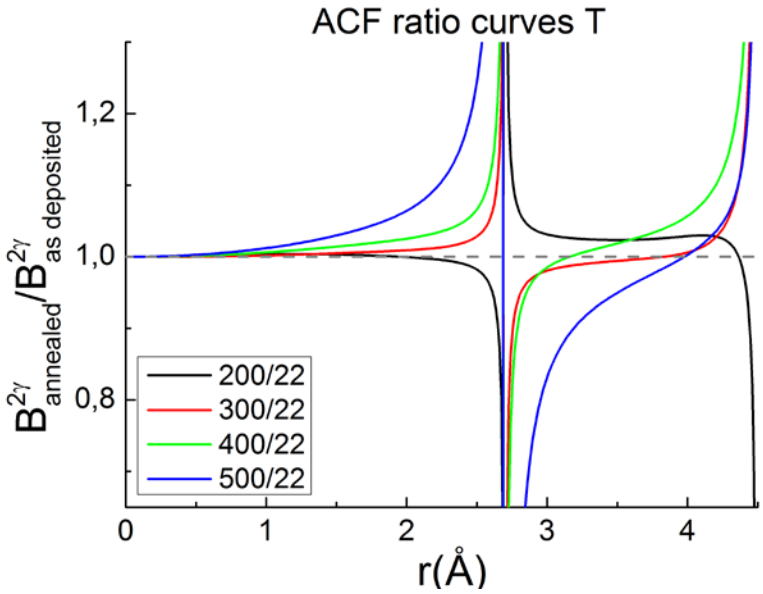

Figure 4-23. Quotient of the $B^{2\gamma}(r)$'s at various annealing temperatures w.r.t. the ACF at room temperature T_o.

The resulting graph is shown in Figure 4-23. The curves up to the first zero crossing are the most reliable parts of this graph. We thus consider here only the curves up to $r < 2.7\,\mathring{A}$ (1^{st} zero crossing) with a typical error of $\leq 2\%$. In this region we observe an increase of the ratio curves starting from 1 and going up.

Now, we expect to find a bigger binding energy E_B for a bigger average open volume defect size, since there will a bigger absence of positively charged nuclei for a bigger vacancy. This means that we divide in the exponent by the smallest binding energy, so we expect to see an exponential decay, for an increasing temperature.

An exponential decay is not what we see in Figure 4-23. This value of the quotient becomes higher for higher annealing temperatures and lies above 1.0. The reason for this trend lies in the shift of the zero crossings for different temperatures. The zero crossing positions are observed to shift to higher values with temperature, except for 200°C, where a zero crossing just before the zero crossing of room temperature was observed. This causes the graphs corresponding to 300, 400 and 500°C to reach increasing values above one, because the zero crossing gradually shifts from 2.70Å to 2.75Å.

The change in positron binding energy was also investigated for an increased hydrogen dilution, by dividing $B^{2\gamma}(r)$ for the diluted samples R=2.5 up to R=10 by $B^{2\gamma}(r)$ corresponding to the undiluted sample R=0, shown in Figure 4-24. This time it is expected that the quotient increases exponentially with increasing hydrogen dilution, seeing as the open volume size decreases for higher dilution. When we look at the domain prior to the 1st zero crossing, we see the opposite trend from what we saw for the temperature $B^{2\gamma}(r)$ quotient curves of Figure 4-23. This time, the quotient curves of Figure 4-24 are decreasing towards the 1st zero crossing. The curves decrease more rapidly for higher dilution. Again, this trend can be explained from the shift of the 1st zero crossing, now towards smaller values (for increased hydrogen

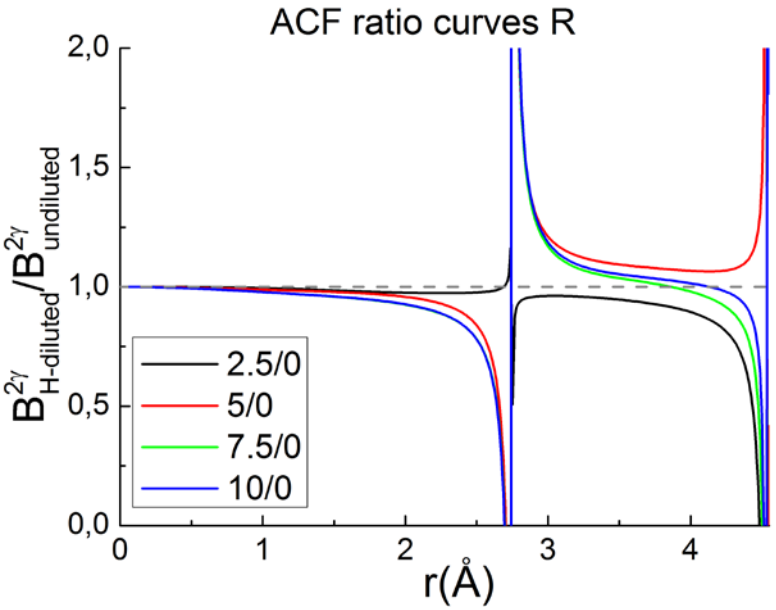

Figure 4-24. Same as figure 21, but now for various hydrogen to silane ratios R w.r.t. R=0.

dilution). The $B^{2\gamma}(r)$ of R=0 first reaches its 1st zero crossing, therefore just prior to the crossing, $B^{2\gamma}(r)$ of R=0 is higher than $B^{2\gamma}(r)$ of the diluted samples, leading to a quotient less than one.

It appears that the 1st zero crossing of the reference function $B^{2\gamma}(r)$ of sample R=0 lies too close together to the zero crossings of the other $B^{2\gamma}(r)$ functions. This makes the influence of the zero crossings too big to extract the positron binding energy. For Ho et al.[35] the difference in 1st zero crossing position was a few tenths of angstroms for $B^{2\gamma}_{E-center}$ and $B^{2\gamma}_{c-Si}$, as we saw in Figure 2-6, while in our case the differences were in the order of 0.01-0.05 Å, which is related here with the change in volume of the defect.

Summarizing, the binding energy E_B is expected to increase for a bigger average open volume defect size. Therefore an exponential decay is expected to be found in the case of an increasing temperature, and an exponential increase in the case of an increasing dilution. However the opposite behaviour is observed. It seems that the behaviour of the ratio curves is dominated by the zero crossing positions. But it might

be that for this material the positron binding energy is in fact decreasing for bigger open volume defects.

Some estimates

How much does the positron binding energy change for a decrease in average open volume (that is observed for increasing hydrogen dilution)? Assuming that the change in positron wavefunction leads to the changes in $B^{2\gamma}$ (Figure 4-24), the change in binding energy for R=10 with respect to R=0 will now be calculated to get an idea of the order of magnitude.

Suppose the positron binding energy E_B in our reference material would equal $E_B = 0.32eV$, the same as Ho et al. found by using formula (4.1) - assuming 0.22eV from their article is a typing error - with $\alpha = 0.29$ as the decay exponential. Squaring both sides of

$$\alpha + \Delta\alpha = \frac{1}{\hbar c}\sqrt{2mc^2(E_B + \Delta E_B)} \tag{4.2}$$

and neglecting the $(\Delta\alpha)^2$ term, we get for the change in binding energy

$$2\alpha\Delta\alpha = \frac{2m\Delta E_B}{\hbar^2} \tag{4.3}$$

Estimating $\Delta\alpha$ for $\frac{B^{2\gamma}_{R=10}}{B^{2\gamma}_{R=0}}$ from the slope of the graph in the region $0\,\mathring{A} < r < 1.5\,\mathring{A}$, using that $e^{-\alpha r} \approx 1-\alpha r$ for small α, we have $\Delta\alpha \approx 0.0228 \pm 0.0006 A^{-1}$. The positron effective mass was assumed to be equal to the electron rest mass; this has appeared to be a good approximation. Substituting all the numbers leads to an increase in binding energy of ΔE_B=0.050±0.002 eV. This is 6 times less than the binding energy of $E_B = 0.32eV$ that was experimentally found by Ho et al, but it is still a big effect from a change in α of less than 10%.

Now suppose that the change in decay exponent would be proportional to the relative shift in the measured 1st zero crossing position: $\Delta\alpha = \frac{0.05\,\mathring{A}}{2.75\,\mathring{A}} \cdot 0.29A^{-1} \approx 0.005A^{-1}$. Then, at the 1st zero crossings position, the decay curve $P(r)$ would take a value of $P(2.7) = e^{-0.005 \cdot 2.7} \approx 0.99$. A change of this order would be too small to measure using this method. These numbers correspond to a change in binding energy of $\Delta E_B = 0.01eV$. This gives an idea for the order of magnitude of the changes, which based on these calculations is on the order of 0.01-0.05eV.

Part II

4.3 Neutron reflectometry

Neutron reflectometry measurements are performed on the neutron sample series. The measured reflectivity profiles are fitted with Gustar using several models in order to find out which of the models best describes them. All models are summarized in Figure 4-24 and the fitting results including error margins can be found in Table 4-4. The fitted reflectometry profiles for all models can be found in Appendix A3-2.

Several models

All four samples R=0, R=10, R=50 and R=250 are first fitted assuming that the film consists of one film layer only (models 1d-4d of Table 4-4). For R=0 and R=10 good fits are obtained with least-square fitters χ^2 of 1.10 and 1.09 respectively. The R=50 and R=250 fits do have fairly low χ^2-values, of 1.29 and 1.43 respectively. However, after a few oscillations the fit curve is not in phase anymore with the oscillations of the data points. Therefore, the film is also modelled using two layers for those samples. This is also the simplest model for an inhomogeneous film. The two-layer approach is also interesting in light of the DB-PAS depth profiles that showed a difference in the microstructure of the top part of the film compared with the bulk (bottom) part of the film.

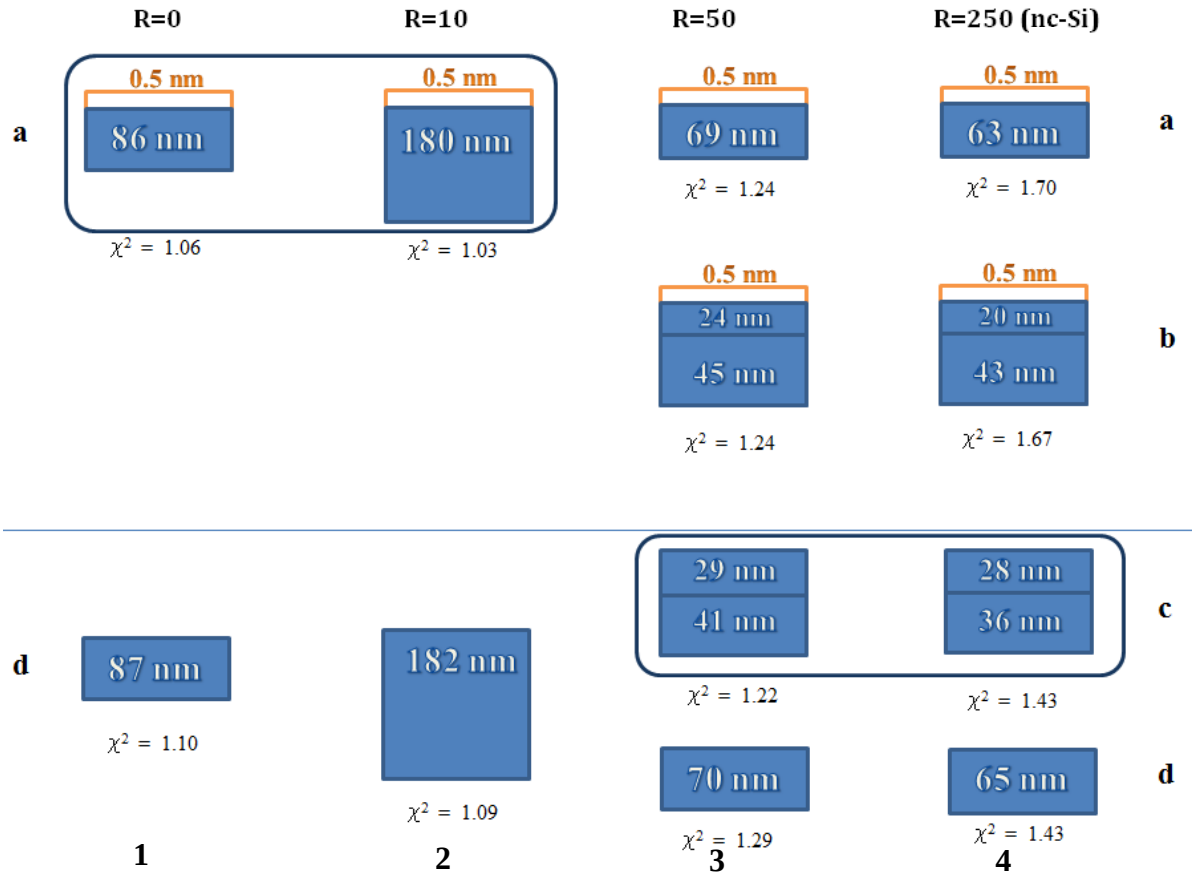

Figure 4-25. All the different models that were used for fitting the ROG-data, including the lowest χ^2-values reached with Gustar on this model. Blue layers are Si-film layers and orange layers are oxide layers.

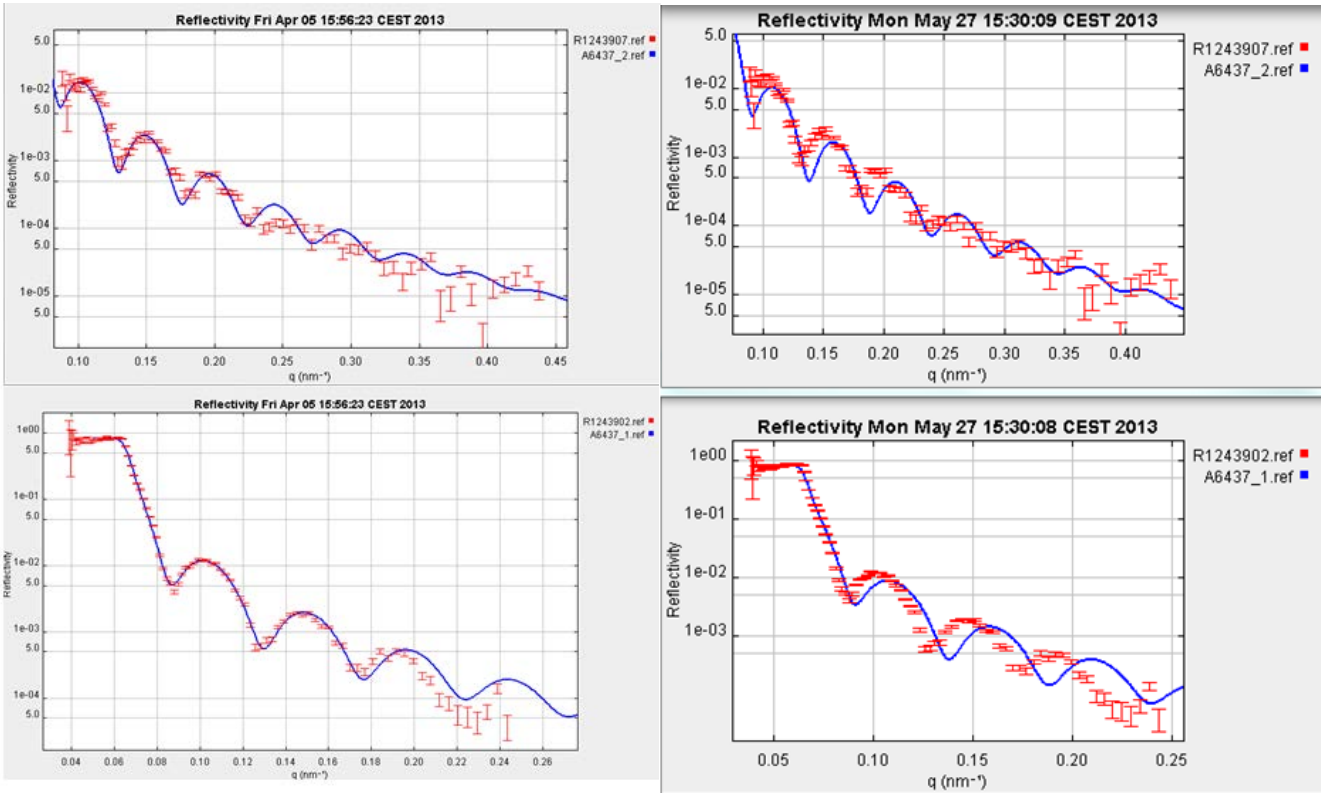

Figure 4-26. At the left model 4c and at the right model 4d. Both models have χ^2=1.43, but model 4c clearly gives a better fit. These fits can also be found in Appendix A.

For models 3c and 4c of R=50 and R=250 we observe that the two-layer approach leads to improved fitting results. For R=50 the χ^2 parameter is reduced from 1.29 to 1.22 and more importantly, the fitting oscillations are better in phase with the data points for both of the samples (see Figure 4-26).

Table 4-4. The main fit parameters of the models presented in Figure 4-24, including their fit errors. The thickness of layer 1 and 2 are called d_1 and d_2, the scattering-length densities belonging to those layers are Γ_1 and Γ_2. The least-square parameter χ^2 , indicating the goodness of the fit, is also listed.

Model	d_1	*error*	d_2	*error*	Γ_1	*error*	Γ_2	*error*	χ^2	In phase?
units	nm	nm	nm	nm	$10^{-2}nm^{-2}$	$10^{-2}nm^{-2}$	$10^{-2}nm^{-2}$	$10^{-2}nm^{-2}$	-	-
1a	86	4	-	-	0.23	0.05	-	-	1.06	Yes
1d	87	0.4	-	-	0.226	0.006	-	-	1.10	
2a	180.87	0.08	-	-	0.2188	0.0005	-	-	1.03	
2d	181.6	0.2	-	-	0.212	0.001	-	-	1.09	
3a	68.71	0.04	-	-	0.205	0.007	-	-	1.24	Up to the 2nd oscillation
3b	24.3	0.3	45.1	.3	0.22	0.02	0.201	0.008	1.24	
3c	29.91	0.05	39.86	.06	0.208	0.002	0.184	0.003	1.22	
3d	70.0	0.5	-	-	0.20	0.01	-	-	1.29	
4a	62.7	0.4	-	-	0.20	0.02	-	-	1.70	
4b	20.13	0.03	42.58	0.02	0.191	0.006	0.200	0.007	1.67	
4c	28.3	0.5	36.2	0.5	0.1988	0.0009	0.195	0.002	1.43	
4d	64.69	0.08	-	-	0.205	0.002	-	-	1.43	No

Oxide layer
For each model, an equivalent one with an additional oxide layer of approximately 0.5 nm on top was also fitted. These are the a- and b-models of Figure 4-25 and table 4-4.

Oxide layer- settings
In these models, the thickness of the oxide layer was allowed to vary between 0.4 and 1.0 nm and the scattering-length density of the layer was allowed to vary between $3.0 \cdot 10^{-3}$ nm^{-2} and $5.0 \cdot 10^{-3}$ nm^{-2}. For the film layers, various limitations on the thickness were used, and the scattering-length density was always allowed to vary between $1.5 \cdot 10^{-3}$ nm^{-2} and $3.5 \cdot 10^{-3}$ nm^{-2}.

Oxide layer - results
For R=0 and R=10, addition of the oxide layer to the model causes a decrease of χ^2 from 1.10 to 1.06 and from 1.09 to 1.03, indicating the presence of such an oxidized layer. However, something strange is going on with the error margins: for R=0 the errors on both the thickness and the SLD become very large, even the largest of all the fits listed in the table. On the other hand, the errors margins of the R=10 fit become smaller from adding an oxide layer. The increase in error margin can be explained by a bigger freedom in the fit due to an increase in the number of fitting parameters.

For R=250 adding an oxide layer to the model results in worse fits, no matter if the film layer is modelled with one or two layers. This is not an unexpected result when you look at the structure of this sample. The film layer is known to consist of microcrystalline grains which tend to oxidize much faster than amorphous material. As a result, the oxygen will be more spread throughout the film, residing also at the surfaces of the grains instead of staying on top.

For R=50 the fits with an oxide layer are comparable in quality with the fits that lack an oxide layer. The sample can best be fitted using two layers and no oxide layer. The corresponding χ^2 parameter is the lowest and so are the error margins on the SLD's.

Model choices
Concluding, the neutron reflectivity profiles for the samples with R=0 and R=10 can best be fitted using one film layer and an oxide layer on top (model 1a and 2a). It appears that for these samples the distribution of the elements is homogeneous. The neutron reflectivity profiles for the samples with R=50 and R=250 can best be fitted using models 3c and 4c, using two layers and no oxide layer. These models however do not always yield reflectivity curves which are in phase with the experimental curves, therefore it would be fruitful to investigate whether some other models would provide a better fit for these datasets.

Some ideas for further improvement of the fits are given here. To start, using a different fitting process might help. We now used a least-square method, which has the risk of getting the estimator stuck in a local minimum, depending on the chosen start values. The more layers a model has, the more complicated the "fitness landscape" looks, so the more risk there is to end up in a local minimum. Using the genetic algorithm (GA) method could avoid this problem. This is a fitting method

adopted from biophysics. The method works similar to evolution. Throughout the fitness landscape, starting parameters are picked and the best few of them are selected, and recombined/mutated to form new start parameter sets. The GA method has been programmed in Gustar as well, but is not working properly at the moment.

Another approach would be to investigate the effect of varying the roughness parameter for the different interfaces of the sample.

Hydrogen concentrations

Using the fitted scattering-length densities (SLDs), the hydrogen concentration in each film layer were calculated for all models, using (3.8) and assuming K=3 (the divacancy model). They are listed in Table 4-5. The minimum and maximum concentrations were also calculated, using the SLD fitting errors. The best models are selected and their hydrogen concentrations are displayed in Figure 4-27. In case of R=0, model 1d was used instead of model 1a, because χ^2 in that model is not much higher, while the error in hydrogen concentration is less.

Adding an oxide layer of only 0.5 nm leads to a significant change in estimated hydrogen concentration in the samples. In R=10 for example the hydrogen concentration is reduced by 1.5% from adding the oxide layer.

Table 4-5. Hydrogen concentrations as follows from the neutron reflectometry experiments. The concentrations are calculated using the fitted SLD-values assuming K=3 (divacancy model). Minimum and maximum concentrations were calculated using the fitting error. Sample 1 corresponds to R=0, etc. as shown in Figure 4-24.

Model	$c_{H,1}$ (at. %)	$c_{H,1,\min}$ (at. %)	$c_{H,1,\max}$ (at. %)	$c_{H,2}$ (at. %)	$c_{H,2,\min}$ (at. %)	$c_{H,2,\max}$ (at. %)
1a	9	- 5	20	--	--	--
1d	8.7	7.0	10.3	--	--	--
2a	10.8	10.7	10.9	--	--	--
2d	12.5	12.2	12.8	--	--	--
3a	14.6	14.4	14.7	--	--	--
3b	12	7	16	15	13	18
3c	13.7	13.2	14.1	19.7	19.0	20.3
3d	15	12	18	--	--	--
4a	17	12	21	--	--	--
4b	17.9	16.5	19.2	15.7	14.0	17.4
4c	16.1	15.8	16.3	17.0	16.6	17.5
4d	14.5	13.9	15.2	--	--	--

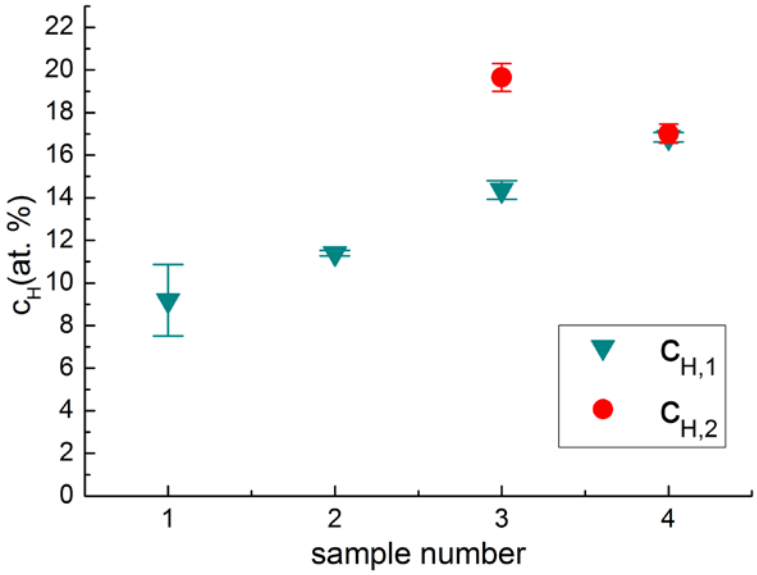

Figure 4-27. Hydrogen concentrations for each film layer. Calculated from the SLD-values obtained for the best Gustar fitting models. Hydrogen concentration for each film layer as calculated from the Γ-values obtained for the best Gustar fitting results. Formula (2.28) was used, with γ=2/3. For sample 1, the model 1d was used as the best model, because of the smaller fitting error bars.

From Figure 4-27 we observe that the computed hydrogen concentration increases with increasing hydrogen dilution. In order to check how accurate this model for calculation the hydrogen concentration is, we will now compare our data to measurements done using IR spectroscopy (FTIR). In Table 4-6 the estimated hydrogen concentrations of the films are given as computed using FTIR spectroscopy measurements. By measuring the absorption of infrared light in the wagging and stretching modes (600-660 cm^{-1} and 1980-2120 cm^{-1}) the fraction of different Si-H configurations in the sample can be determined and can be used to compute the hydrogen concentration bonded to Si-atoms.[16]

Table 4-6. FTIR, RT and Ellipsometry results on the same samples. Estimated hydrogen concentrations, Thicknesses and hydrogen concentrations (estimations). Fitting errors.

Sample	R	c_H	Film thickness Ellipsometry	Film Thickness Reflec/Transm
	-	at. %	nm	nm
M2671	0	9	85.2 ± 0.05	84.9 ± 0.50
M2676	10	11	186.2 ± 0.17	187.4 ± 1.00
A6443	50	12	70.4 ± 0.04	68.1 ± 0.40
A6437	250	4-6	64.6 ± 0.02	65.4 ± 0.40

For R=0 and R=10 the FTIR and neutron results are consistent: both calculations give 9% and 11% for those samples. For R=50 and R=250 the neutron measurements result in higher hydrogen concentrations than is detected by FTIR measurements. Instead of 4-6%, concentrations of at least 15.8% for the first layer and 16.6% for the second layer are computed for the neutron reflectometry for R=250. And for R=50,

instead of 12% we find c_H to be at least 13.2% for the first layer and at least 19.0% for the second layer.

The larger hydrogen concentrations seen by the neutrons can be explained by the presence of hydrogen that is not silicon bonded, such as molecular hydrogen or interstitial atomic hydrogen, and can therefore not be detected using FTIR. It is also possible that the FTIR hydrogen concentrations for R=50 and R=250 are not accurate. These samples are deposited in a different way and need a different proportionality constant to convert Si-H bond count into hydrogen concentration. This proportionality constant has not been determined accurately. Lastly, the spreading of the oxygen through the film that we mentioned before for sample R=250 can lead to a modified scattering-length density and an incorrect hydrogen concentration.

Layer thickness

The film layer thicknesses have been determined using three complementary techniques. The neutron reflectometry fitting results are listed in Table 4-6, and the results obtained by Ellipsometry (which also is a reflection technique, where polarized light is used) and RT measurements (where both the reflected and the transmitted spectra are measured) including their fitting errors can also be found in Table 4-6. All measured thicknesses are in very good agreement.

It is interesting to see that the neutron reflectivity profiles for the samples with R=0 and R=10 can be modelled using one layer while the neutron reflectivity profile for the samples with R=50 and R=250 is better described with a two layers (and possibly more).

Part III

4.4 Raman spectroscopy

Raman measurements are performed on several samples of the R-series and on the high pressure sample in order to try to detect the presence of molecular hydrogen in the films. This is done for as-deposited samples and for samples after annealing, using the same annealing procedures as before. The motivation to look for Raman peaks corresponding to H_2-vibrations and the results of these Raman measurements are discussed in this section. Secondly the degree of crystallization at various temperatures is discussed. All Raman measurements were performed at the KavliNanolab at the TU Delft, except when specified otherwise.

Possible presence of molecular hydrogen
Measurement results from two different experiments give rise to the question whether molecular hydrogen might be present in the a-Si:H films. These experiments are the H-effusion experiments that were done by Beyer, along with recent FTIR-measurements done by Melskens, both performed on the R-series and the high pressure sample.

The FTIR measurements revealed a sudden increase in density at 300°C (Figure 4-28). This is just where the Si-H bonds start breaking, but H-effusion has been proven not to start yet. A theory is that the material density increases because the freed hydrogen fills up the open volume deficiencies in the material. The density increase was higher for bigger hydrogen dilution: in the as-deposited state the density of the samples R=0-10 is ~2.24 g/cm^3. At 300°C the density increased to 2.30 g/cm^3 for R=0 and even up to 2.38 g/cm^3 for R=10. Since the samples diluted with more hydrogen also contain more hydrogen, there is a correlation between the amount of hydrogen present in the material and the intensity of the density-increase. A possible explanation for the density increase is therefore sought in the presence of molecular hydrogen in the open volumes.

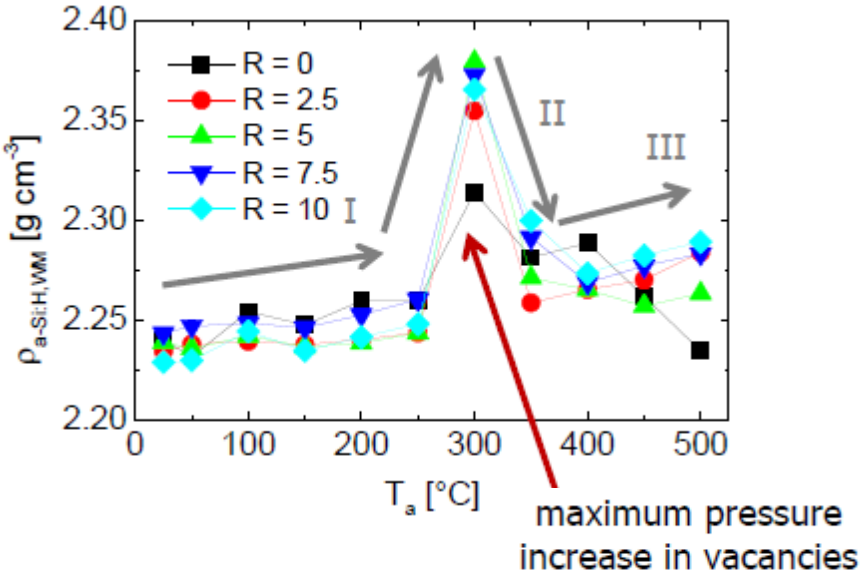

Figure 4-28. Material density as obtained from FTIR measurements, by Jimmy Melskens[27].

From the H-effusion measurements, two broad hydrogen effusion peaks were found. One at around 400°C and one at around 600°C. At the same time it is known from FTIR measurements that all Si-H bonds in the material are broken from 500°C.

When Si-H bonds in the material break, and no new bonds with Si are formed by the released hydrogen, either atomic or molecular hydrogen can be formed. The molecular hydrogen could either reside interstitially in the material, or could be staying in the (bigger) open volume deficiencies. The hydrogen molecules could be isolated from each other, or it might even be that a hydrogen gas is formed inside really big open volumes (which are not expected in these materials, based on TEM measurements on similar samples). The presence of molecular hydrogen inside open volumes can influence the momentum distribution: at very high pressures, on the order of a few 100 kbar, the S-parameter even reduces to 1, similar to the value for crystalline silicon.[2] On the other hand, in 1999 Fedders et al. found from a SEDOR-NMR experiment, that nearly 40% of the hydrogen in their PECVD-deposited a-Si:H material resided at tetragonal T-like sites, as isolated molecular hydrogen.[51]

Whether the hydrogen is in the neighbourhood of the other hydrogen atoms or not, results in different Raman vibrations. In 1999 Leitch et al.[26] measured the vibrational frequency of molecular hydrogen in c-Si. They measured 3601 cm^{-1} at room temperature for isolated molecular hydrogen situated at the tetragonal T-sites in the Si lattice. For gaseous H_2, they measured 4161 cm^{-1}, which is in the same range as the values that were reported by other groups, 4151-4161 cm^{-1}, as cited in Leitch's paper.

4.4.1 Same dilution, several annealing temperatures

Raman spectra were taken for samples with R=5 for various annealing temperatures to check for hydrogen content and for the degree of crystallization. The as-deposited and T=500°C spectra (stepwise annealed at the 2D-ACAR setup) were measured using sample M1583, and the T=300°C and T=800°C spectra (both stepwise annealed as

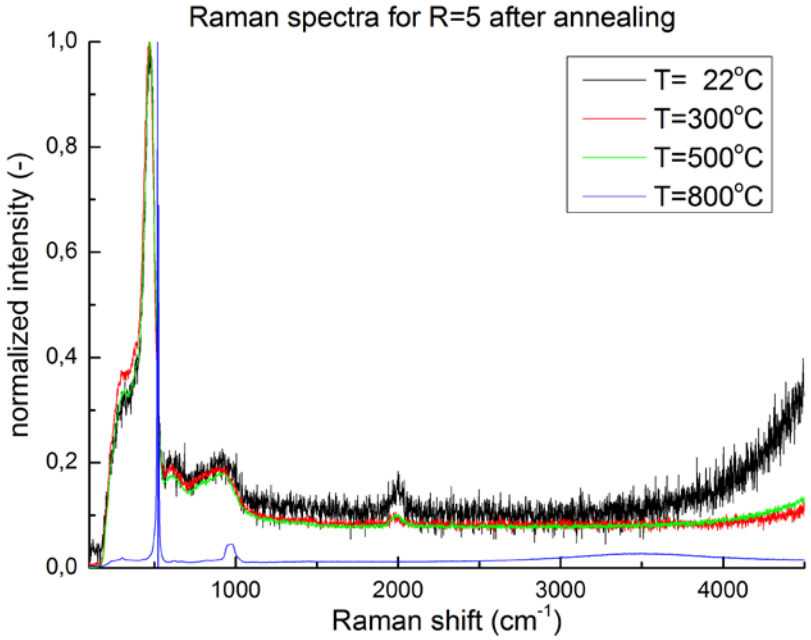

Figure 4-29. Raman spectra for R=5 at several annealing temperatures. For the as-deposited measurement and at T=500°C, sample M1583 was used and for the T=300°C and T=800°C measurements, sample M1584 was used.

described for the DB-PAS annealing experiments) were measured using sample M1584. The results are shown in Figure 4-29. Firstly, any peaks corresponding to molecular hydrogen should fall within the region of 3500cm^{-1} up to 4500cm^{-1}. For none of the samples any peaks are observed in this region.

Secondly, the spectra of T=22^{o}C, T=300^{o}C and T=500^{o}C show no signs of crystallization. The peaks near 300cm^{-1}, 600cm^{-1}, 965cm^{-1} and the broad peak near 490 cm^{-1} with shoulder near 380cm^{-1} are all attributed to wagging and bending modes of Si-Si bindings in a-Si:H, and are expected for amorphous silicon.
The spectrum of the sample annealed to 800^{o}C is entirely different. It is completely flat except for two peaks, one near 520cm^{-1} and one near 965 cm^{-1}, both characteristic for the Si-Si bonds in a crystallized material[52].

For the spectra of T=22^{o}C, T=300^{o}C and T=500^{o}C a peak near 2000 cm^{-1} is present that lacks after annealing to 800^{o}C. The peak corresponds to the stretching mode of Si-H bonds[53]. Somewhere between T=500^{o}C and T=800^{o}C, the Si-H bonds are broken. From FTIR measurements it appeared that no Si-H bonds are left at 500^{o}C. It is possible that the different circumstances for annealing have led to the presence of the Si-H peak for the current sample with 500^{o}C.

The peak near 520cm^{-1} shows a disturbance at the centre, this is attributed to saturation of the detector.

4.4.2 The spectra for R=0,5 and 10 after annealing to 800^{o}C

Subsequently spectra were also taken for the samples with R=0 and R=10 (M1096 and M1588) after annealing to 800^{o}C, as shown in Figure 4-30. The obtained spectra are similar to the one that was already measured for R=5. No sign of molecular hydrogen is found. All three samples have completely crystallized.

The same samples were also measured using the Raman setup at the PVMD group of

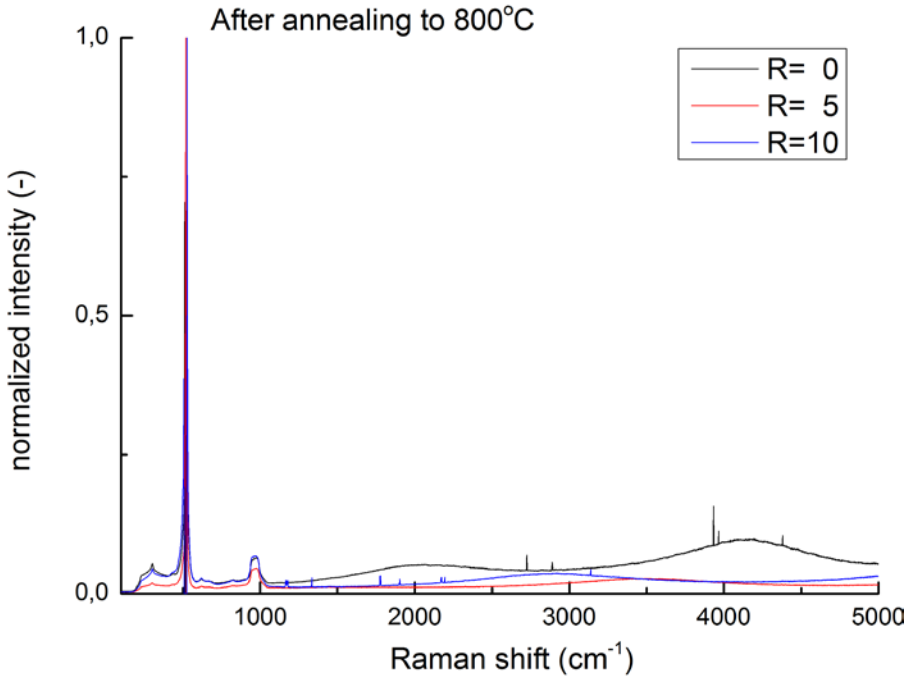

Figure 4-30. Raman spectra of samples with R=0;R=5 and R=10 after annealing to 800^{o}C.

the TU Delft. Small shifts in the peak positions were observed and therefore these peaks were fitted. A Lorentzian peak shape was assumed for the first peak near 520 cm^{-1}, and a Gaussian peak shape was assumed for the second peak, near 965 cm^{-1} (Figure 4-31). The fitted positions for the centres of the peaks including their fitting errors are shown in Table 4-7.

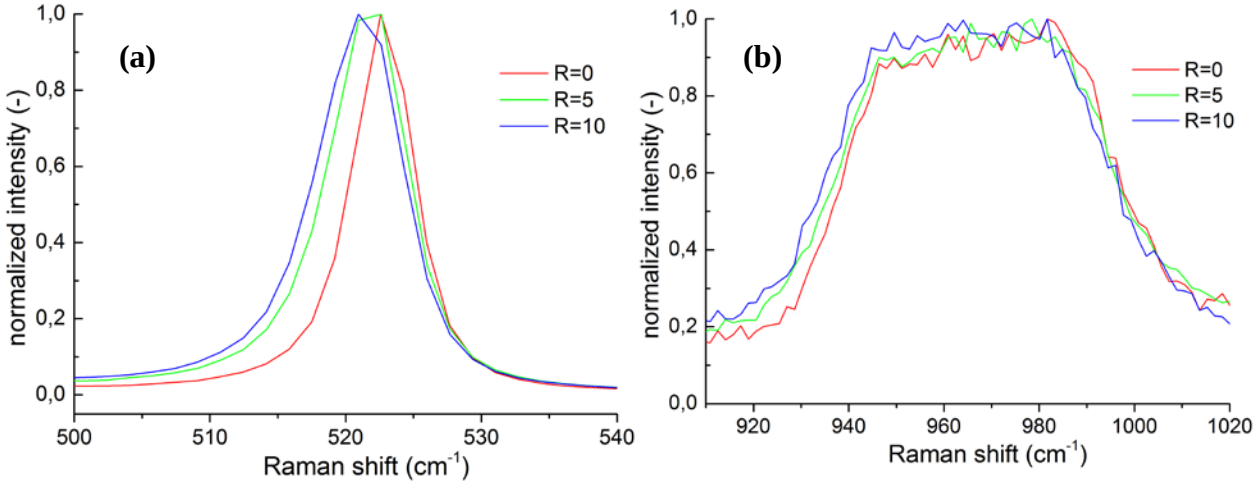

Figure 4-31. Characteristic Raman peaks for c-Si as found for samples with R=0, R=5 and R=10 after annealing to 800°C. (a) Lorentzian peak shape and (b) Gaussian peak shape.

Table 4-7. Fitted centres for the crystalline peak positions for samples R=0,R=5 and R=10 after annealing to 800°C including their fitting errors.

Sample	Gaussian peak position	Lorentzian peak position
	cm^{-1}	cm^{-1}
R=0	969.0±0.7	522.78±0.01
R=5	967.6±0.3	521.64±0.02
R=10	965.4±0.4	521.03±0.02

Both from the figure and the table it is visible that the peak positions show a small shift to lower Raman shifts for an increasing R. From the table it can be seen that the shift is significant. It is remarkable that after annealing there can still be observed differences between the samples that were prepared with different hydrogen dilutions. It is expected that most or all of the hydrogen, in all of its configurations, has effused out of the sample at a temperature of 800°C. The shift in peak position with increasing R has been associated with a decrease in compressive stress.[54]

4.4.3 The spectra of R=0 up to R=10 and the high pressure sample (T=300°C)

Based on the FTIR results presented above, it was decided to measure the Raman spectra of the samples R=0 up to R=10 as well as the high pressure sample after annealing them up to 300°C using the same annealing procedure as was used during the DB-PAS and FTIR annealing experiments (isochronous annealing during one hour, letting the samples cool down in between the annealing steps, 50°C per annealing step).

All obtained spectra looked similar to the spectrum of R=5 at 300°C that is shown in Figure 4-29. No hydrogen was detected for any of the samples and all of the samples were in the amorphous phase. For completeness these Raman spectra are given in Appendix A4-1.

5 Conclusions and recommendations

This chapter summarizes the main conclusions of this research and presents recommendations for future research projects.

5.1 Conclusions

5.1.1 Effects of H-dilution on the defect size

It was found from DB-PAS and 2D-ACAR experiments that the momentum distribution broadens with increasing hydrogen dilution. In addition, using 2D-ACAR it was found that the first zero crossing position of the positron-electron autocorrelation function $B^{2\gamma}(r)$ decreases with increasing dilution, from 2.70Å to 2.75Å. Both findings indicate a decrease in average open volume defect size in a-Si:H. This decrease can be either due to a decrease in average vacancy size, or due to an increased hydrogen content at the surface of, or inside, the vacancies.

In the first case, it could for example be that in samples with low H-dilution both di- and tri-vacancies are present, while in samples with high H-dilution only divacancies are present. In the (S,W) diagram saturation can be observed for higher dilution, possibly at the point where only divacancies are grown. It could also be that the average open volume per missing Si-atom decreases with hydrogen dilution, due to an increased pressure during deposition.

As for the alternative explanation that includes hydrogen inside the vacancies, it could be that for high hydrogen dilution, the additional hydrogen may occupy part of the open volume and reduce the average open volume size.

5.1.2 Effects of annealing on the defect size

DB-PAS annealing studies were performed on R=0,5 and 10 samples as well as on the high pressure sample. The films were investigated in terms of S and W. Some general trends were observed as well as some individual differences for the samples.

General trends

For each of the four samples initially, for temperatures up to 400^{o}C, S increases considerably and W decreases considerably, indicating an increase in the average open volume. This is ascribed to the *agglomeration of vacancies* into larger vacancies. From 300^{o}C on, hydrogen is known to be released, also from the vacancies, further increasing the open volume sizes.

Depending on the sample, somewhere between T=400^{o}C and T=550^{o}C the decrease in S and increase in W is started. These trends indicate a decrease in the average defect size, that is probably caused by the *release of* the larger *vacancies* at the surface. An increase in W could also indicate that more core states are measured, indicating the *release of hydrogen* from the sample.

And eventually, for each of the samples, S decreases and W increases. At the final annealing temperature of 800^{o}C, all samples end up *crystallized* (confirmed with

Raman spectroscopy). For some samples S<1 and W>1 even occurs, indicative of oxygen-related defects, that originate from the SiO_2-substrate, or from the oxidation layer that is initially on top of the film. Hydrogen gas inside voids can also reduce S and increase W, but not below a value of 1.

The (S,W) plots for each sample show that three different processes take place. This study indicates that these processes most likely correspond to: I vacancy agglomeration, II hydrogen effusion & release of vacancies at the surface and III crystallization.
For the high pressure sample, two processes (I&III) were observed.

Deposition-dependent trends
The DB-PAS results indicate that the divacancy is the dominant vacancy for the as-deposited films. The maximum vacancy size upon annealing increases with increasing hydrogen dilution. For the high pressure sample, the DB-PAS results even indicated the presence of nanosized voids (d≥1nm).

Between T=400^{o}C up to T=550^{o}C for higher H-dilution, a plateau in S is observed that could indicate an increased stability of the vacancies in the film.

From T=600^{o}C up to T=750^{o}C, the decrease in S and increase in W goes with an increased steepness for increasing hydrogen dilution. This might indicate that some hydrogen is still present in the sample, even though at 500^{o}C all Si-H bonds are broken (FTIR spectroscopy). That would be consistent with the H-effusion measurements, that show a broad HT-peak at around 600^{o}C. From this it is concluded that the hydrogen that is still present must be residing interstitially or inside voids, in the form of H or H_2. Using Raman spectroscopy it is researched whether all the hydrogen has effused out at 800^{o}C.

Annealing and 2D-ACAR
From 2D-ACAR & CDB annealing studies it was found that up to T=500^{o}C, the momentum distribution narrows, and the zero crossings position increases. These are clear indications that the average open-volume defect's size increases. In the step from T=400^{o}C to T=500^{o}C the increase and the narrowing are the strongest, and a decrease in overlap between the electron and positron wavefunctions are observed from $B^{2\gamma}(r)$, which is expected for a bigger open volume. This forms a strong indication of the occurrence of vacancy agglomeration. This time not based on the S/W parameters, but on the behaviour of the entire momentum distribution and corresponding spatial structure function $B^{2\gamma}(r)$.

Using $B^{2\gamma}(r)$ to calculate the positron binding energy
The method of Ho et al.[35] of using the measured $B^{2\gamma}(r)$ to calculate the positron binding energy E_B is employed in the present study for the estimation of the change in this energy ΔE_B with the change in open volume defect size. The change in positron binding energy with open volume defect size is estimated to be on the order of 0.01-0.05 eV, which is much smaller than the E-center binding energy of 0.29eV that was found by Ho et al.. While E_B is expected to increase with increasing defect size, the

relevant graphs rather indicate the opposite effect. Probably this behaviour is caused by the big influence of the shift in zero crossing position.

5.1.3 Relation between solar cell properties and nanostructure parameters

Using DB-PAS on the diode/triode samples, it was found that the solar cells with a lower degradation of the fill factor and of the efficiency also have a lower S-parameter for the as-deposited layers. This could indicate that a smaller average vacancy size leads to an increased stability. This also correlates with a lower deposition rate of the films. The smaller vacancy size may be therefore caused by a lower deposition rate and the resulting deposition of a denser film. The fact that the degradation in the efficiency and fill factor correlate with the S-parameter shows that also in this case open volume defects are an important factor for the efficiency. This forms another indication that the dangling-bond models do not suffice to describe the a-Si:H nanostructure and the volume deficiencies therein.

5.1.4 Detectability of hydrogen using neutron reflectometry

Neutron reflectometry demonstrated to be a useful tool for studying a-Si:H absorber layers. The technique is sensitive to all hydrogen inside the film, including atomic and molecular hydrogen (in contrast with FTIR). It can therefore be expected that the effusion out of the sample as a result of the temperature annealing process can be monitored as well.

A new model made by Dr. Ad van Well was used to compute the hydrogen concentration based on neutron reflectometry profile fitting results, under the assumption that all the hydrogen resides in completely H-passivated mono- and divacancies.

R-series

Good fits were obtained for samples with R=0 and R=10, assuming one homogeneous film layer. The computed hydrogen concentrations based on these fits of 9% and 11% respectively agree very well with FTIR results for the same samples. With FTIR the atomic and molecular hydrogen are not taken into account, so we can conclude that the concentration of non-Si-H bonded hydrogen is very low for these samples in the as-deposited state.

Reasonably good fits were obtained for the reflectivity profiles of a sample alike to the high pressure sample and for a nanocrystallite sample. Both these films appeared inhomogeneous. The computed hydrogen concentrations deviate from the FTIR results. This deviation is probably there because of invalid assumptions in the conversion of the FTIR parameters to hydrogen concentrations for these samples. The FTIR was calibrated for the samples with R=0 and R=10. It may further be due to deviations in the NR-modelling caused by an incomplete description of the layer structure, or because considerable amounts of atomic/molecular hydrogen (not chemically bonded to the Si atoms) are present in these samples. Better fitting of the NR and FTIR measurements would be useful to get a better estimate of the hydrogen concentration inside the film.

All the fits were good enough to obtain accurate layer thicknesses that are in very good agreement with FTIR and ellipsometry results.

5.1.5 Raman spectroscopy

At 500°C the films were completely in the amorphous phase and at 800°C they were completely crystallized.

No molecular hydrogen could be detected for the tested samples of the R-series. Various samples were tested for one or several of the following conditions: either in the as-deposited state, or after annealing at 300°C, 500°C and 800°C. It could not be determined where the hydrogen resides in the film after all the Si-H bonds are broken (at 500°C, from FTIR) and before a second effusion peak occurs (at 600°C, from H-effusion on similar samples). And it is also still unclear what causes the rise in film density at 300°C (FTIR result).

5.2 Recommendations

5.2.1 Defect structure

Clear trends were found for the open volume defect size as a function of temperature and hydrogen dilution. Several explanations are possible for what causes the change in open volume. It might be that:

1. The dominant vacancy type changes (one material contains mainly divacancies while the other material contains tri- or tetravacancies)
2. The volume per missing Si atom varies (for example the open volume is pressed together due to higher pressure during deposition)
3. The hydrogen content near or inside the vacancy varies (for example in high H-dilution material, more hydrogen resides in the vacancies).

In order find out which explanations apply here, more precise information about the spatial structure of the defects is highly desirable. An excellent candidate for providing additional information about the second and third points is $B^{2\gamma}(\vec{r})$, the positron-electron autocorrelation function. By performing ab-initio calculations of $B^{2\gamma}(\vec{r})$ for various defect structures of a-Si:H with different degrees of hydrogen-passivation, and comparing them to experimental results, more detailed insights into different local geometry and hydrogen surroundings structure of the defects could be obtained.

Further positron lifetime spectroscopy may aid to determine whether the first explanation is valid or not. With DB-PAS, 2D-ACAR and CDB we have acquired information about the *average* defect size. Lifetime spectroscopy on the same samples can be used to examine which (neutral and negatively charged) vacancy defect types occur. Perhaps also to obtain their respective concentrations.[30] For the diode/triode samples knowledge of the defect types and concentrations can also help in understanding the effect of a more dense material on the volume per missing atom in a vacancy.

5.2.2 Hydrogen

Neutron reflectometry could be used to obtain hydrogen depth profiles as a function of the annealing temperature. More insight could be gained in where the hydrogen resides in the material, also as a function of annealing temperature.

It is of special interest to investigate what happens between annealing temperatures of 500^{o}C and 600^{o}C, since it is unknown where the hydrogen goes after all Si-H bonds are broken but before it effuses out of the sample. In general, comparison with H-effusion measurements and FTIR annealing measurements are desirable.

In order to obtain more accurate hydrogen depth profiles required for this procedure, it is desirable to improve the fitting of the measured reflectivity profiles. Using the genetic algorithm function of the fitting program instead of the least-squares method may help, since with this method the influence of the starting parameters on the obtained fit is reduced.

5.2.3 Depth-dependence of hydrogen and vacancies

It will be useful to investigate which effects underlie the difference in the shape of the obtained DB-PAS depth profiles, when measuring with/without the oven. Understanding the mechanisms responsible for the change in depth profiles can help to extract a reliable shape for the full depth profile. Then one can completely deduce the defect size as a function of film depth during in-situ annealing. Combining hydrogen depth profiles and defect size distribution depth profiles, and studying both as a function of temperature, can lead to more detailed knowledge about the 3 annealing processes that were observed.

5.2.4 High pressure sample

A DB-PAS annealing experiment for a series of high pressure samples is recommended to better interpret the different behaviour of the high pressure sample in comparison to the R-series. In particular it is interesting to see whether the behaviour at annealing temperatures in the range of 400^{o}C and 450^{o}C would be reproduced, both in absolute and relative sense: are nanosized voids as maximum defect sizes a trend for high pressure samples? And is the steepness of process II in the (S,W) plot repeated for other high pressure samples with (slightly) different deposition conditions? In order to study the agglomeration of vacancies in this sample an ACAR and PALS (positron annihilation lifetime spectroscopy) annealing study can also help to find out whether the initial open volume size and the increase in size are bigger for this sample.

5.2.5 Raman

By measuring samples of the R-series at annealing temperatures of T=550^{o}C up to 750^{o}C it can be investigated at which temperature the crystallization starts and finishes and at which temperature all Si-H bonds are broken. This can help in interpreting the DB-PAS annealing results for the same temperature range.

To obtain upper boundaries for the amount of molecular hydrogen present in the films, reference samples with known H_2-content could be used and their Raman spectra could be compared to the spectra of the studied a-Si:H films.

Appendices

Contents

Appendix 1: 2D-ACAR

A1-1 Dilution series: count rates

Table A1-1. Coincident count events for the hydrogen dilution series as detected with 2D-ACAR.

Sample name	Annealing temperature	Coincident count events
M1580	0	$7.6 \cdot 10^6$
M1582	2.5 (batch 1)	$3.7 \cdot 10^6$
M1584	5	$1.1 \cdot 10^7$
M1586	7.5	$1.8 \cdot 10^7$
M1588	10	$1.8 \cdot 10^7$
M3459	2.5 (batch 2)	$4.6 \cdot 10^7$

A1-2 Temperature series: count rates & error analysis on $B^{2\gamma}$

Table A1-2. Coincident count events for sample M1583 as detected with 2D-ACAR. The table also lists the first zero crossings that were determined from the measured $B^{2\gamma}$ function. The errors on the zero crossing were estimated using figure A1-1.

Annealing temperature	Coincident count events	1st zero crossing	Estimated error on the 1st zero crossing
°C	-	Å	Å
22	$7.5 \cdot 10^6$	2.699	0.01
200	$5.0 \cdot 10^6$	2.694	0.015
300	$8.0 \cdot 10^6$	2.705	0.01
400	$7.3 \cdot 10^6$	2.709	0.01
500	$1.0 \cdot 10^7$	2.749	0.007

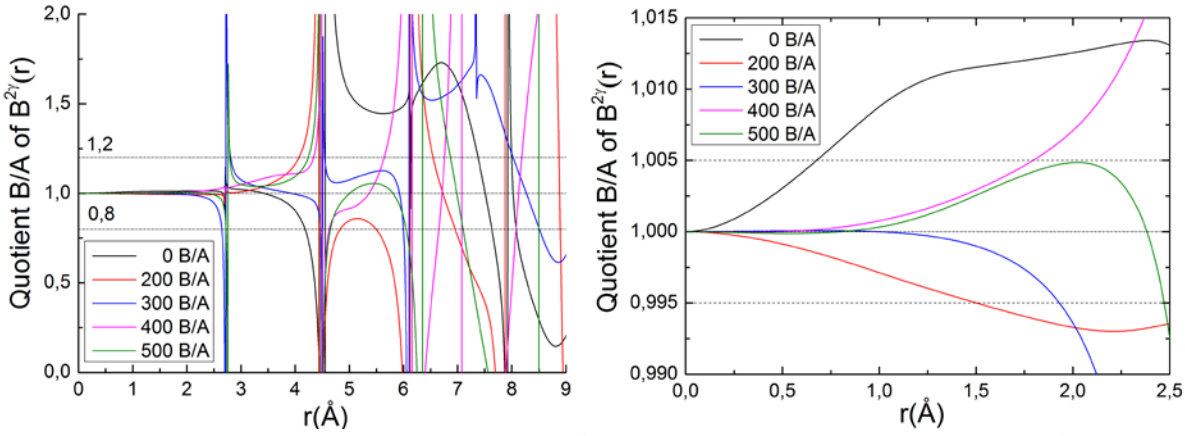

Figure A1-1. Research the accurateness of $B^{2\gamma}$. Figure shows the quotient of the $B^{2\gamma}$ function computed from the two halves of the data. The count rate in this experiment was lower than the count rate with the R series, therefore the error of the ACF is bigger in this case. At the right, the same figure is shown, zoomed in.

Appendix 2: DB-PAS

A2-1 Effect of measuring using the oven

In this appendix section we show the effect on the S&W parameters of measuring with oven in the VEP setup.

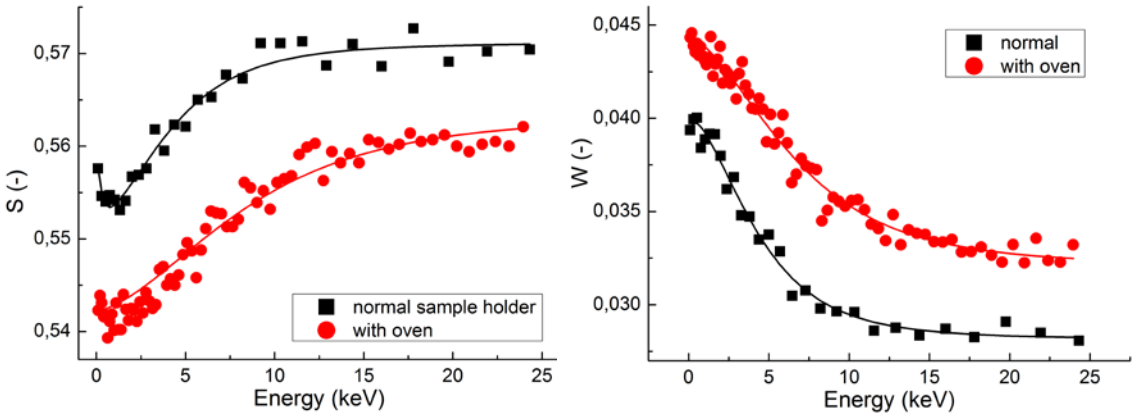

Figure A2-1. DB-PAS S&W Depth profiles of c-Si reference sample using the oven sample holder and the normal sample holder.

It has appeared that measuring with or without oven inside the DB-PAS set-up gives rise to different S- and W-values. An example of this for c-Si is shown in Figure A2-1. The c-Si sample used as a reference for the measurement of the high pressure sample was measured both with and without the oven inside the set-up. See also Figure 3-5 for pictures of the oven with sample holder. The most important differences between the measurements are, that in case of the oven, all the determined S-parameters show a shift down along the entire depth profile. The opposite effect occurs for W. Furthermore there are also some changes in shape of the depth profiles. During fitting it appeared that the positron diffusion length increases beyond the maximum diffusion length for positrons in c-Si.

Some explanations for the effect of using the oven on the measured depth profile are given below. The explanations are sought in the small distance between sample and oven. An effect that has been known to occur is the Compton effect. Gamma rays emitted from the sample reach the oven material, where they have an inelastic collision with an electron. A gamma ray of lower energy is re-emitted from the oven. As a result the entire Doppler distribution shifts to the left (lower energies), which leads to a decrease (increase) of S (W).

It is also possible that Positronium (Ps), a hydrogen-like molecule consisting of a positron and an electron, is formed at the surface of the sample. Back-diffusion of positrons towards the surface that have some kinetic energy left are candidates for Ps-formation at the surface. Ps-molecules are neutral and therefore they are not influenced so much by the axial magnetic field that focusses the positrons. This makes it possible for them to escape the extension of the positron bundle line and diffuse towards the oven wand. Once arrived at the wand, the Ps-molecule annihilates, resulting in (undesirable) gamma rays. This back-diffusion effect changes in severity with the positron implantation profile, since only positrons close to the surface can diffuse back.

For a-Si:H the positron diffusion length is much smaller, and this is one of the reasons why the changes in the depth profiles caused by the presence of the oven are expected to be different. Figure A2-2 shows normalized Doppler depth profiles for samples with R=5 and R=10 in the as-deposited state. The measurements performed in the setup with the oven are normalized using S/W obtained for reference measurements with c-Si samples measured in the oven setup. The corresponding normalization parameters are given in Table A2-1.

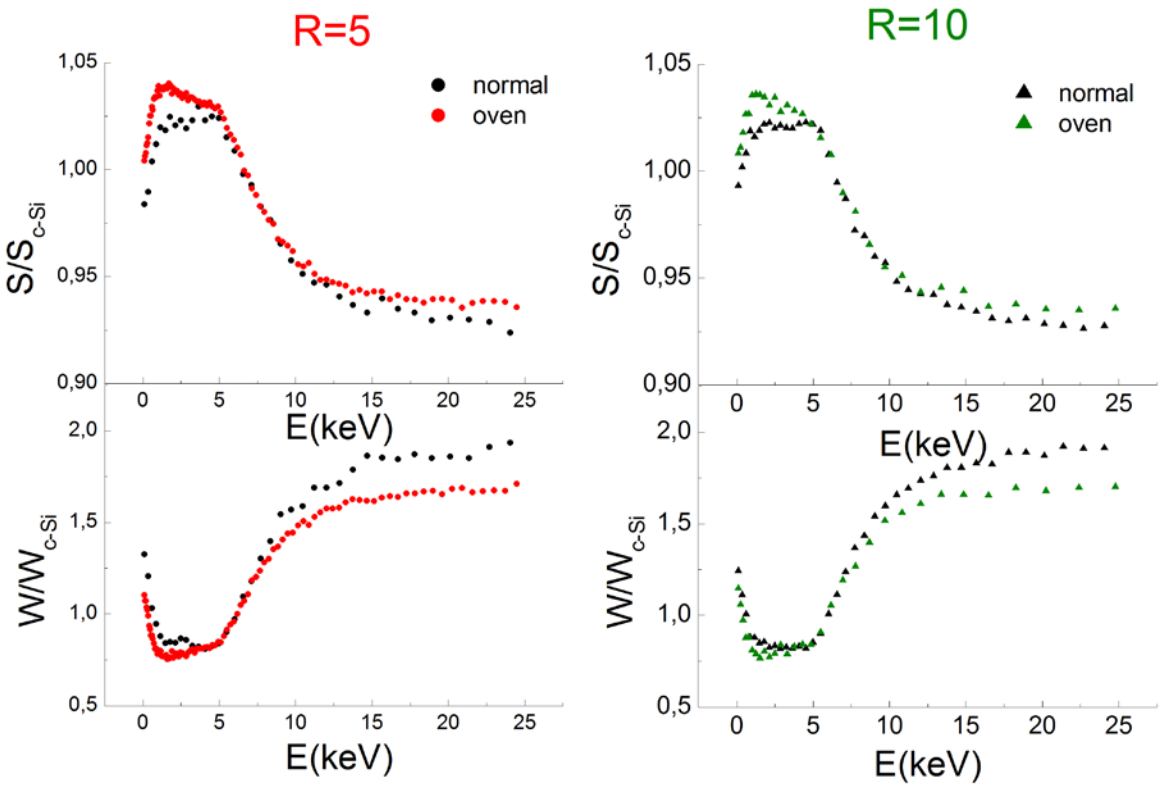

Figure A2-2. Normalized DB-PAS depth profiles for samples with R=5 and R=10 in the as-deposited state. The measurement including the oven was normalized with the S/W parameters obtained from c-Si measurements including the oven.

After normalization, the difference between the S-parameters is very big at the top-layer of the film (around 1-2 keV). For the bulk layer of the film the parameters match better. For the W-parameters there is a good agreement at the bulk-layer, and at the top-layer the W-value corresponding to the oven is slightly lower. In the region from 20-25 keV, corresponding to the glass substrate, S is higher and W is lower when measured using the oven. Together these differences indicate that a more detailed investigation is needed in order to extract a reliable shape for the full depth profile.

Sample	Setup	S	W
R=5 (M1584)	Normal	0.57208	0.2797
	Oven	0.55970	0.0329
R=10 (M1588)	Normal	0.57208	0.2797
	Oven	0.56065	0.03242

Table A2-1. Normalization parameters used to normalize the depth profiles shown in Figure A2-2.

A2-2 VEPFIT diode/triode samples

Figure A2-3a and b show that the obtained one-layer fits for the diode/triode DB-PAS depth profiles agree well with the experimental data.

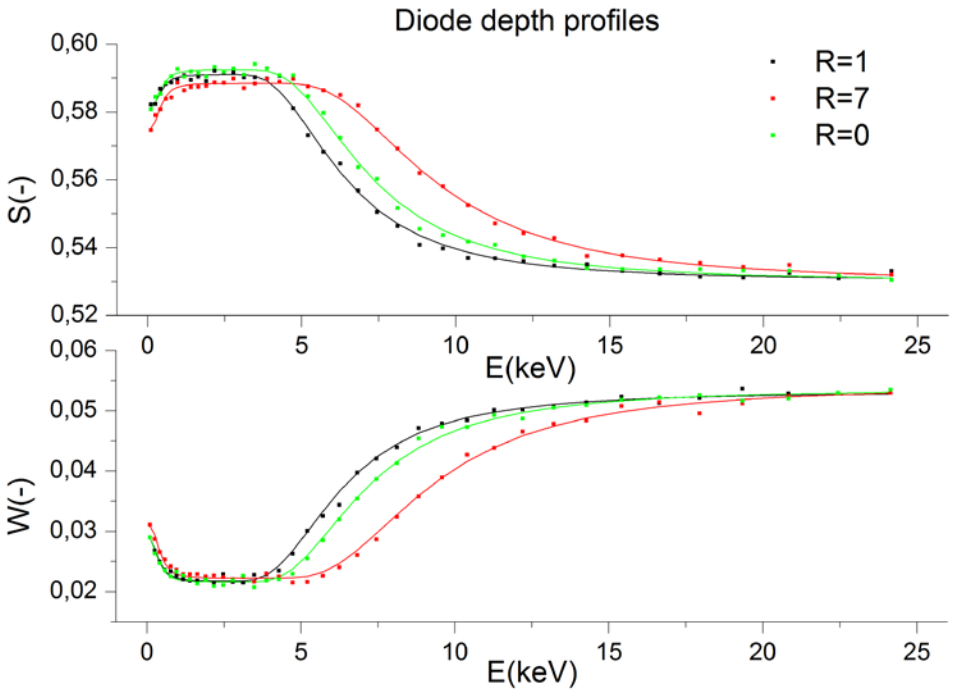

Figure A2-3a. DB-PAS depth profiles of the measured diode samples. The profiles were fitted using a one-layer model.

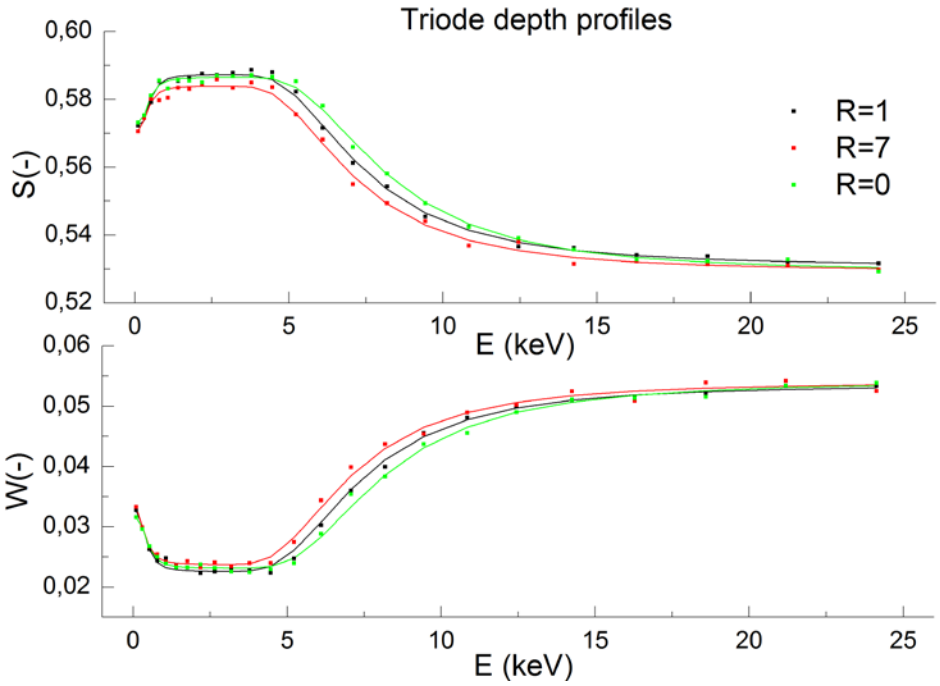

Figure A2-3b. DB-PAS depth profiles of the measured triode samples. The profiles were fitted using a one-layer model.

Appendix 3: Neutron reflectometry

A3-1 Hydrogen concentration model

Here follows the model that was used for computing the hydrogen concentration based on the fitted neutron reflectometry profiles. The model has been developed by Dr. Ad van Well. Here follows his description of the model

Amorphous hydrogenated silicon

Mono- and di-vacancy model

Starting from amorphous silicon (a-Si), with mass density ρ_{a-Si} and number density N_{a-Si}, amorphous hydrogenated silicon (a-Si:H) is modelled by replacing 1 Si atom by 4 H atoms (mono-vacancy model, $K=4$) or 2 Si atom by 6 H atoms (di-vacancy model, $K=3$), and keeping the Si density of the matrix unchanged.

Relation between mass density and number density is given by $\rho=\frac{NM}{N_A}$, with M the molar mass and N_A Avogadro's number. We consider a volume of 1 m^3 and define

N_{Si} : number of Si atoms in a-Si

N'_{Si} : number of Si atoms in a-Si:H

N'_H : number of H atoms in a-Si:H

If we define the hydrogen content by c (molar fraction), then a-Si:H can be represented by
$a\text{-}Si_{1-c}H_c$, yielding

$$N'_H=\frac{c}{1-c}N'_{Si}$$

In our model $N_{Si}-N'_{Si}$ Si atoms are replaced by $N'_H=K\left(N_{Si}-N'_{Si}\right)$ H atoms, resulting in

$$N'_H=\frac{c}{1-c}N'_{Si}=K\left(N_{Si}-N'_{Si}\right)$$

leading to

$$N'_{Si}=\frac{1-c}{1-\gamma c}N_{Si}$$

$$N'_H=\frac{c}{1-\gamma c}N_{Si} \qquad (1)$$

$$\gamma=1-\frac{1}{K}$$

Results are given in Fig.1.

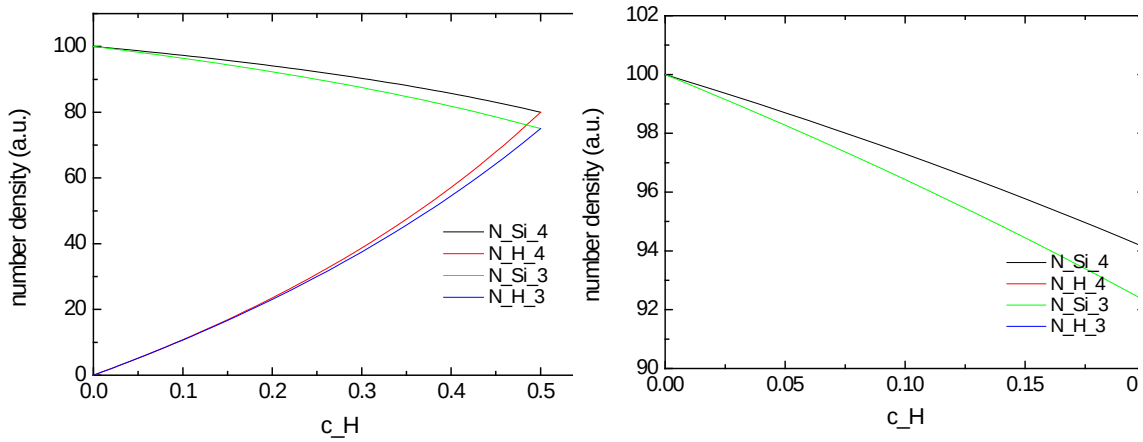

Figure 1.
Relative number density of both Si and H atoms as a function of the hydrogen mol fraction c. Black and red lines represent N'_{Si} and N'_H, respectively, for $K = 4$. Green and blue lines are for $K = 3$.
An a-Si mass density of 2.287 gcm^{-3} [2] corresponds with $N_{Si} = 49.0\,\text{nm}^{-3}$

The mass density of a-$Si_{1-c}H_c$ is then given by

$$\rho_{a-Si:H} = \frac{N'_{Si}M_{Si} + N'_H M_H}{N_A} = \rho_{a-Si}\left(\frac{1-c}{1-\gamma c} + \frac{c}{1-\gamma c}\frac{M_H}{M_{Si}}\right) \qquad (2)$$

with $M_{Si} = 28.09$ g/mol, $M_H = 1.008$ g/mol, and $N_A = 6.022 \cdot 10^{23}\,\text{mol}^{-1}$.
In Ref. [1], Eq. (2), the following expression for this density is used:

$$\rho_{a-Si:H} = \rho_{a-Si} - \left(\frac{\rho_{a-Si}}{K}\rho_{a-Si} - \rho_H\right)c \qquad (3)$$

Using $\rho_H = (M_H/M_{Si})\rho_{Si}$ and $\rho_{a-Si} = 2.287\,\text{gcm}^{-3}$ [2], both expressions are displayed in Fig.2.

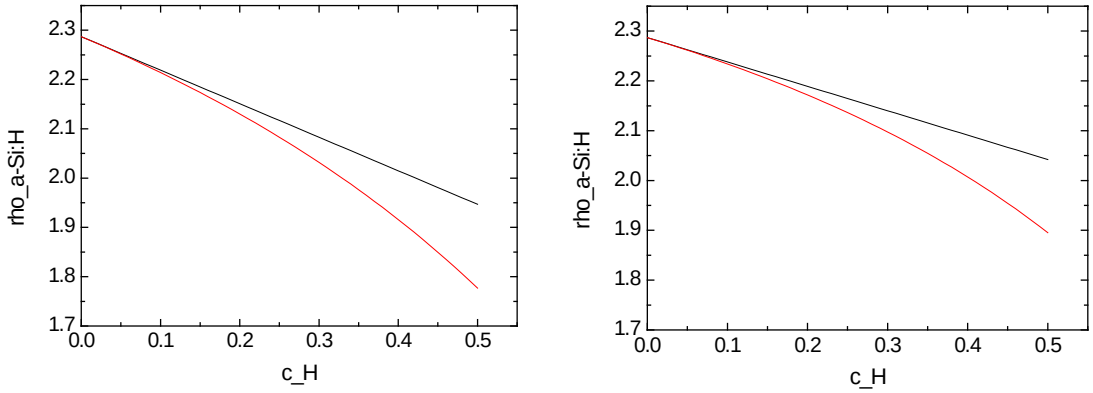

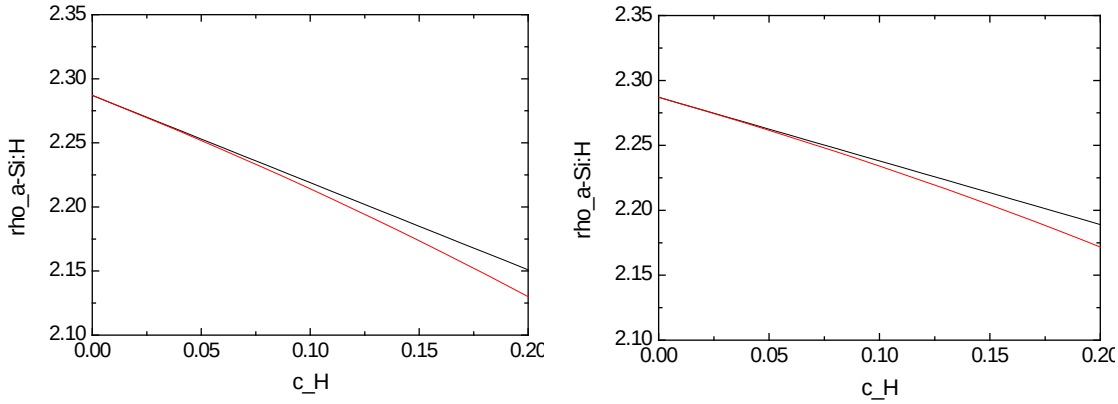

Figure 2.
Mass density $\rho_{a-Si:H}$ of amorphous hydrogenated silicon as a function the hydrogen mol fraction c, according to Eq.(2) (red) and Eq.(3) (black) for $K = 4$ (left panels) and $K = 3$ (right panels)

Scattering-length densities

The neutron scattering-length density for neutrons of a:Si:H is given by

$$\zeta_n = N'_{Si} b_{n,Si} + N'_H b_{n,H} \qquad (4)$$

and the X-ray scattering-length density by

$$\zeta_x = N'_{Si} b_{x,Si} + N'_H b_{x,H} \qquad (5)$$

The neutron coherent scattering length b_n is element and isotope specific and can be found in Ref [3]. The X-ray scattering length b_x is proportional to the electron density and can be approximated by $b_x = Zr_0$, with $r_0 = 2.818$ fm the classical electron radius. Numerical values are given in Table I. The neutron and X-ray scattering length density according to Eqs.(1,4-5) are displayed in Fig. 3.

	Z	M	b_n	b_x
		g mol^{-1}	fm	fm
H	1	1.008	-3.739	2.818
Si	14	28.09	4.149	39.45
O	8	16.00	5.803	22.54

Table I. Neutron and X-ray scattering length for hydrogen, silicon, and oxygen.

Eqs.(1) and (4) lead to

$$c = \frac{N_{Si} b_{n,Si} - \zeta_n}{N_{Si}\left(b_{n,Si} - b_{n,H}\right) - \gamma\zeta_n} \qquad (6)$$

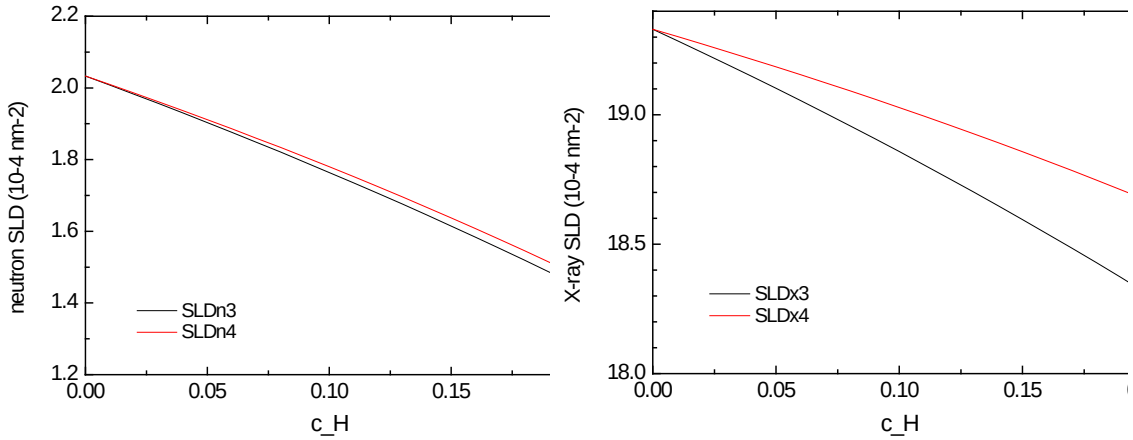

Figure 3.
Neutron scattering-length density ζ_n (left) and X-ray scattering-length density ζ_x (right) cf. Eqs.(1,4-5) with Si number density of amorphous silicon $N_{Si} = 49.0\,\mathrm{nm}^{-3}$, as a function of the molar hydrogen concentration c_H. Black: $K = 3$; red: $K = 4$.

In the neutron and X-ray reflection experiments quartz is used as a substrate. According to the supplier its mass density is $\rho_{sub} = 2.203\,\mathrm{gcm}^{-3}$, yielding a number density $N_{SiO2} = 22.1\,\mathrm{nm}^{-3}$ and scattering-length densities $\zeta_{n,SiO2} = 3.48 \cdot 10^{-4}\,\mathrm{nm}^{-2}$ and $\zeta_{x,SiO2} = 1.87 \cdot 10^{-3}\,\mathrm{nm}^{-2}$.

References

[1] A.H.M. Smets et al., Appl. Phys. Lett. 82 (2003) 1547
[2] Z. Remes et al., Phys. Rev. B 56 (1997) R12 710
[3] www.ncnr.nist.gov/resources/n-lengths

A3-2 Neutron reflectometry fits Gustar

R=0 models

Model 1a

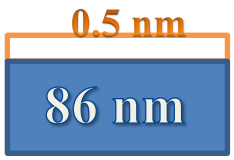

χ^2 = 1.06

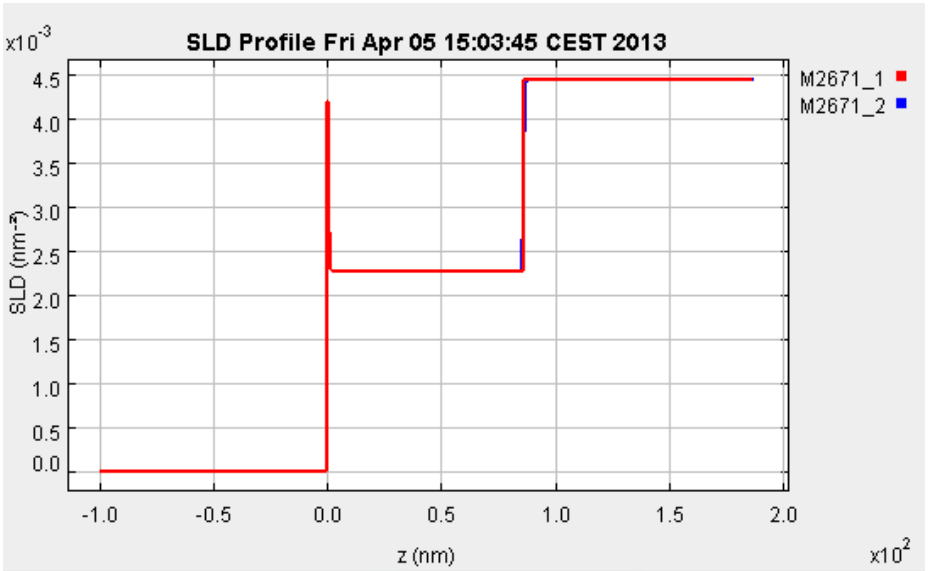

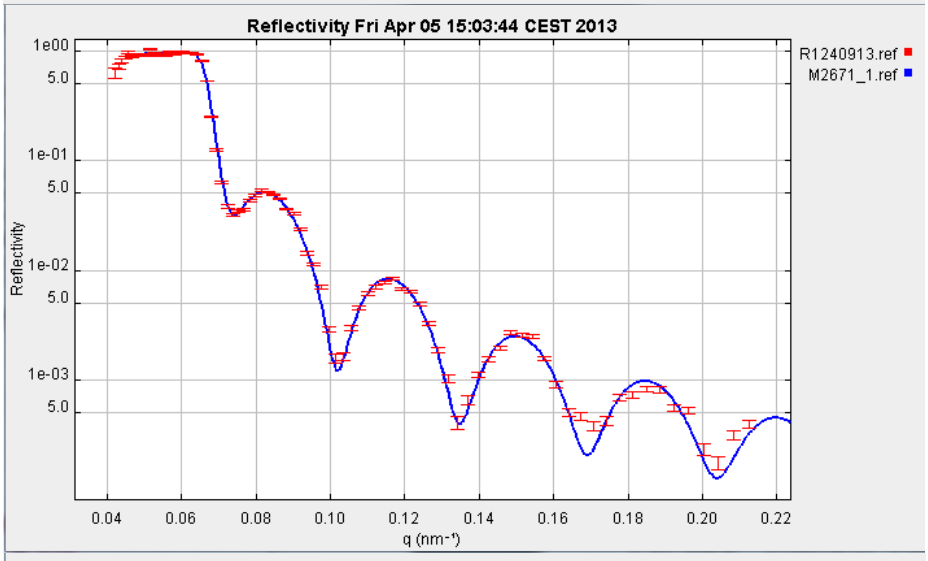

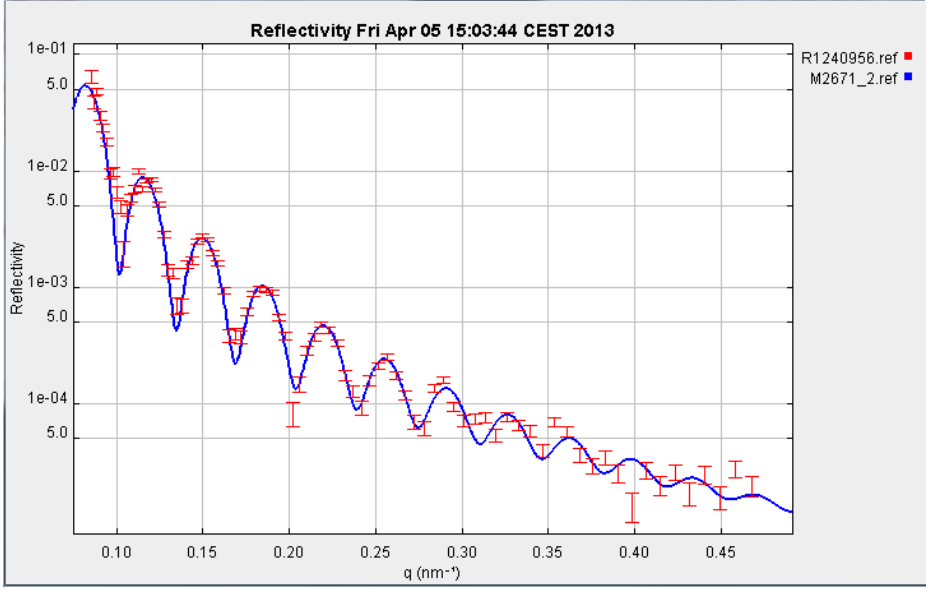

Model 1d

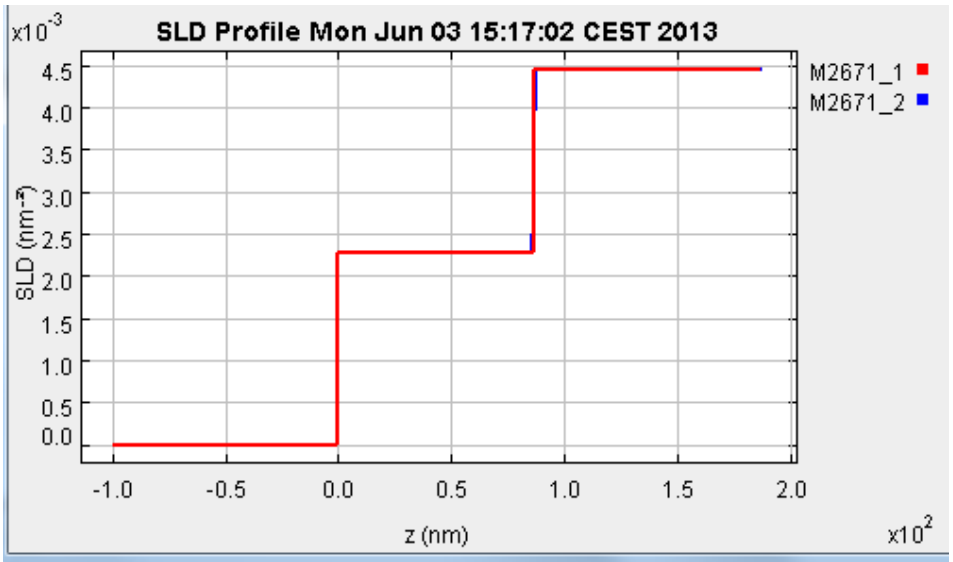

87 nm

χ^2 = 1.10

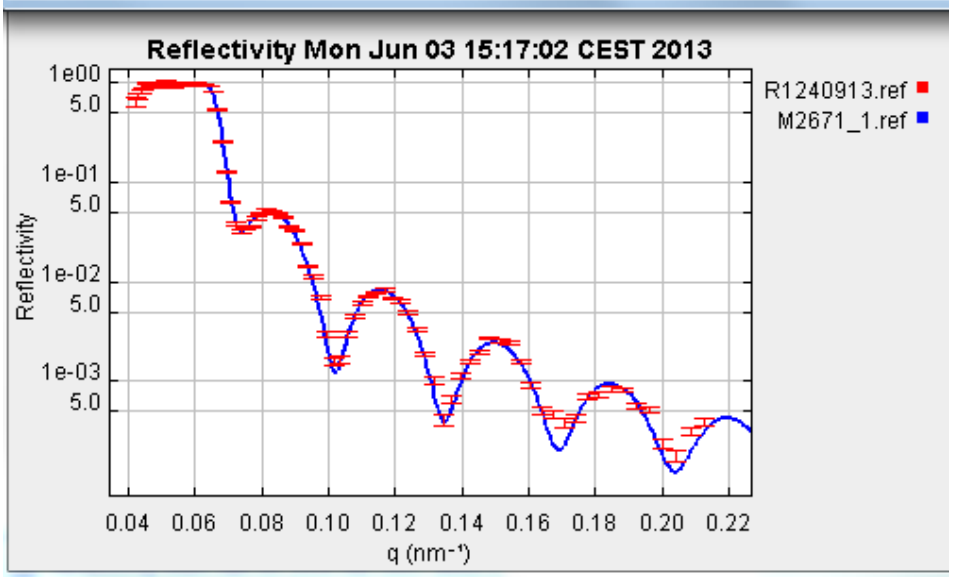

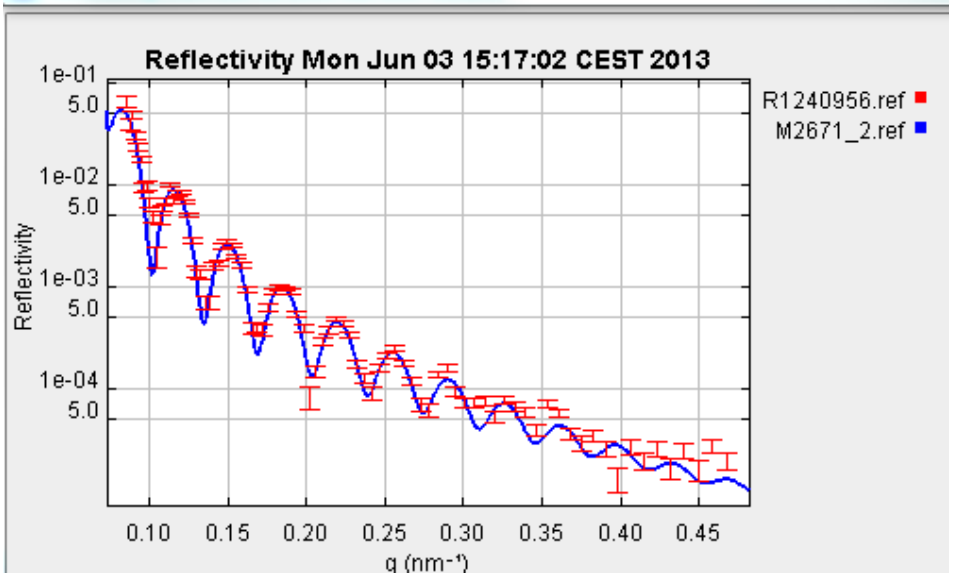

R=10

Model 2a

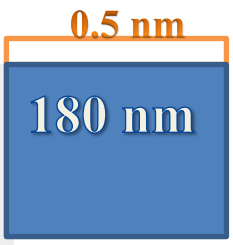

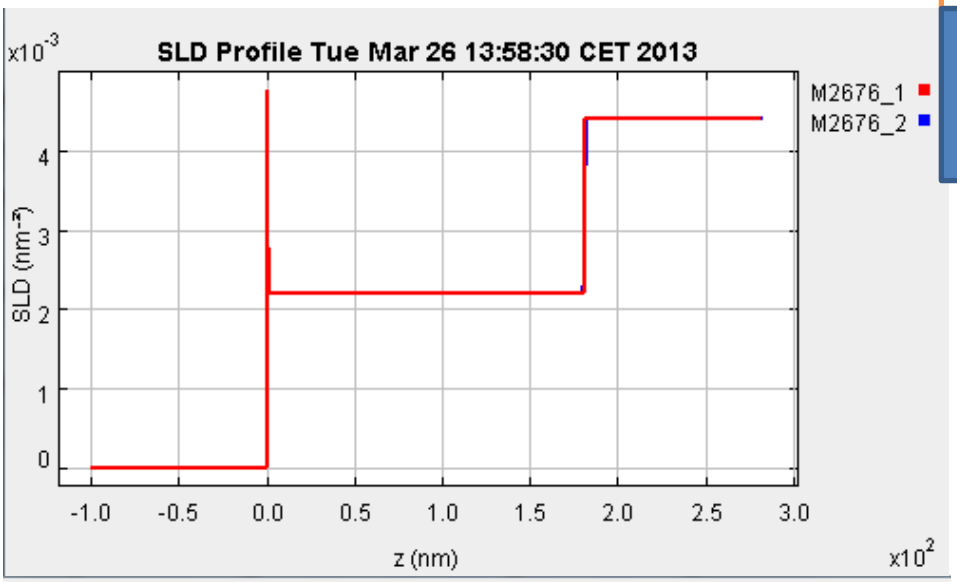

χ^2 = 1.03

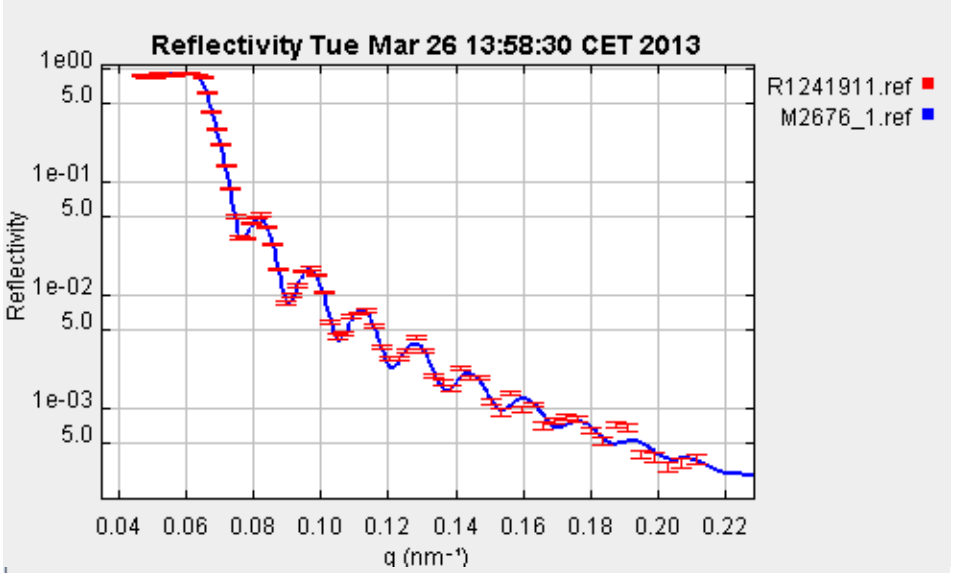

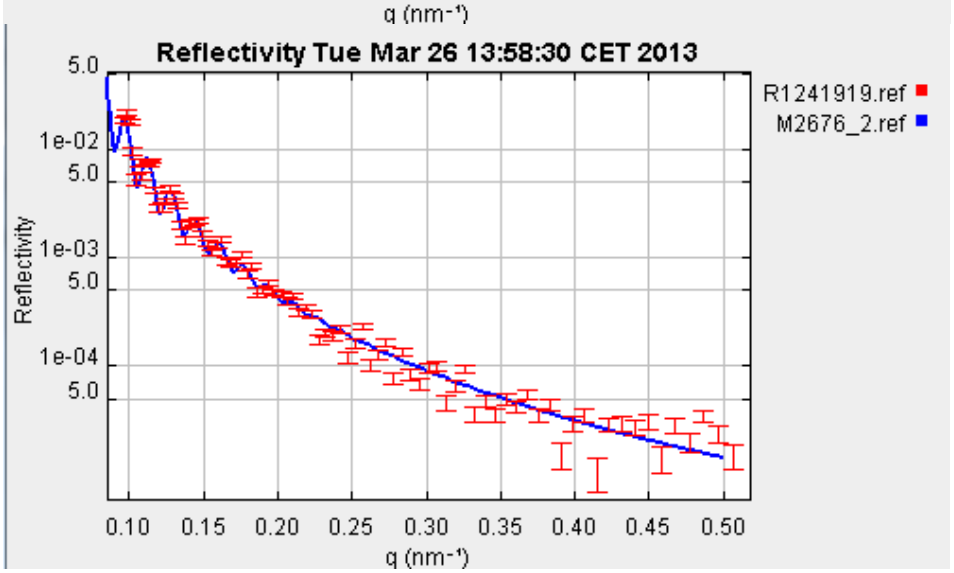

Model 2b

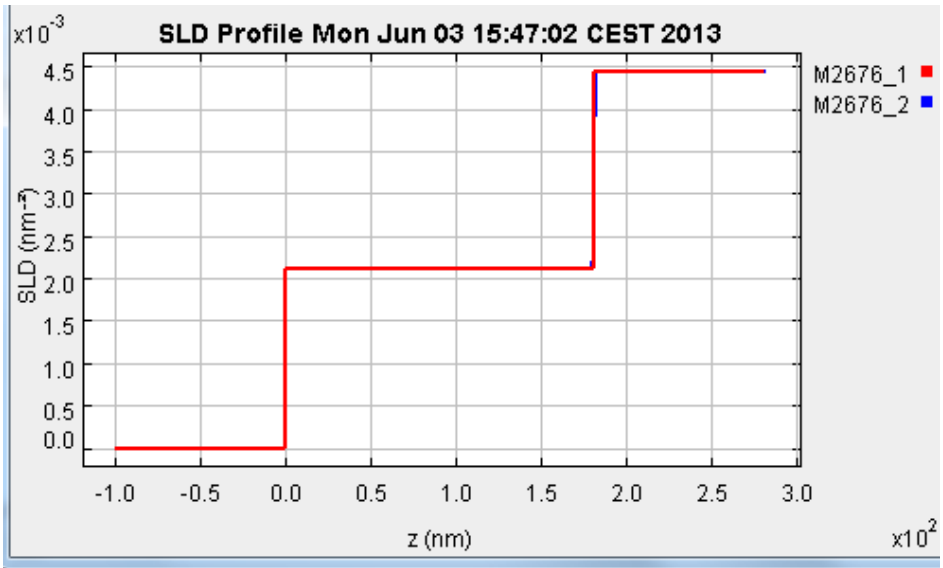

182 nm

χ^2 = 1.09

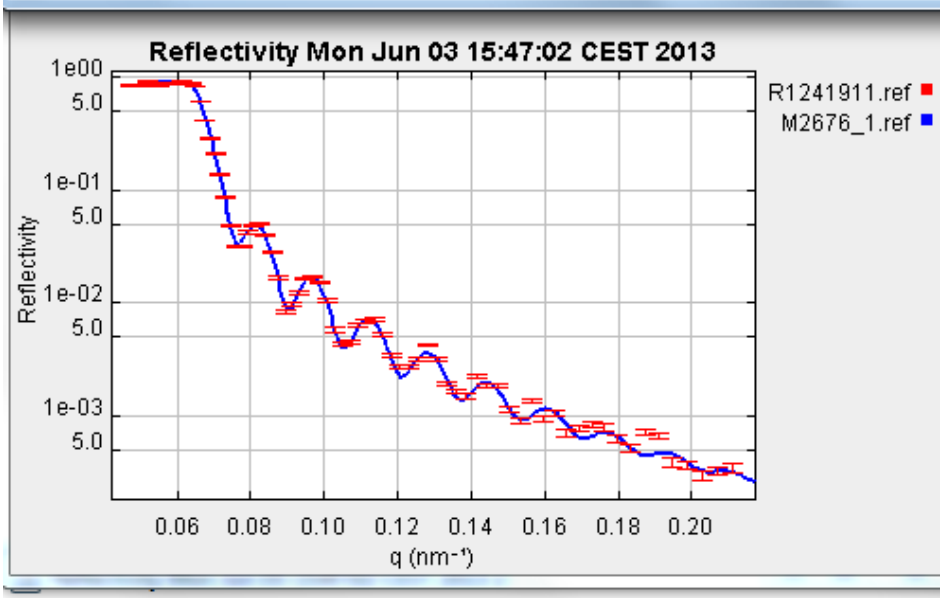

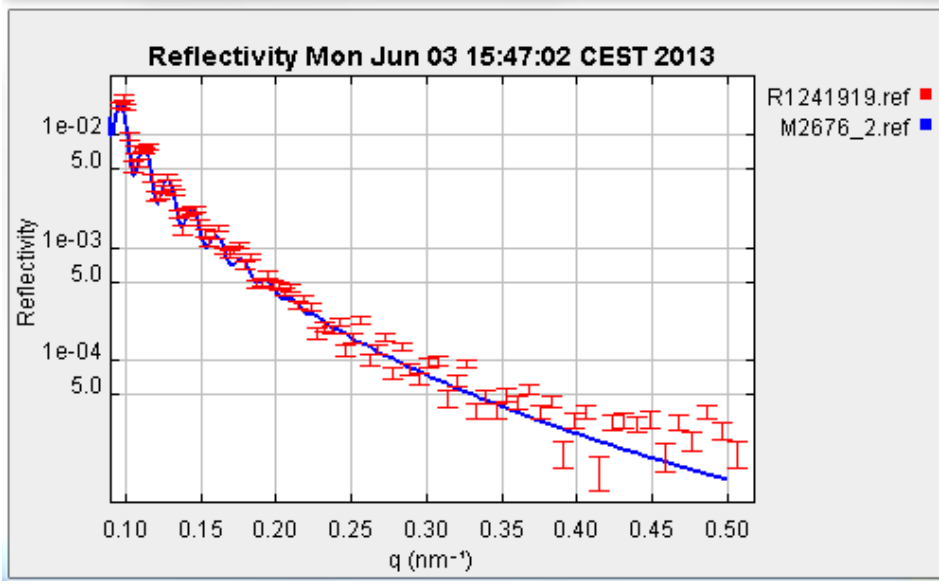

R=50

Model 3a

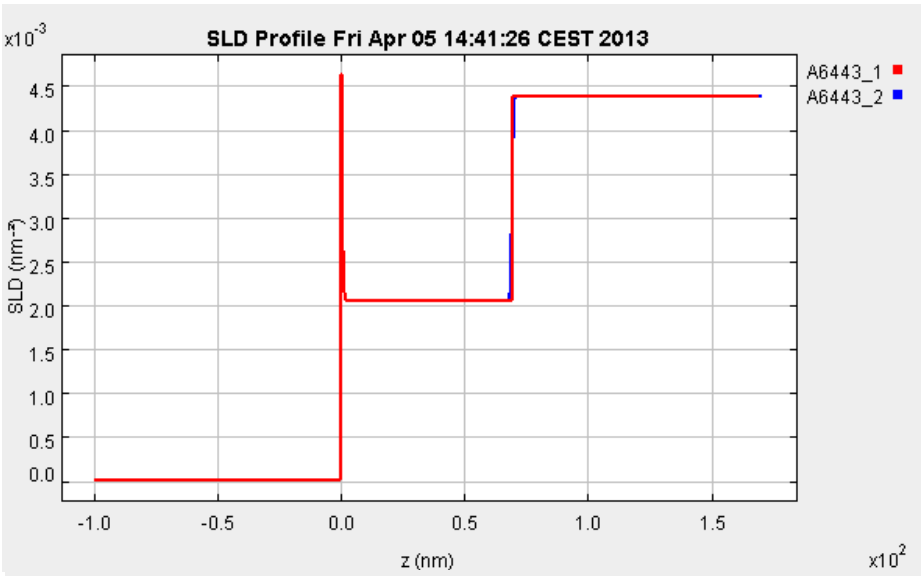

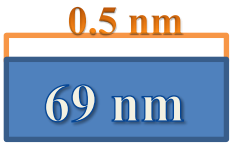

χ^2 = 1.24

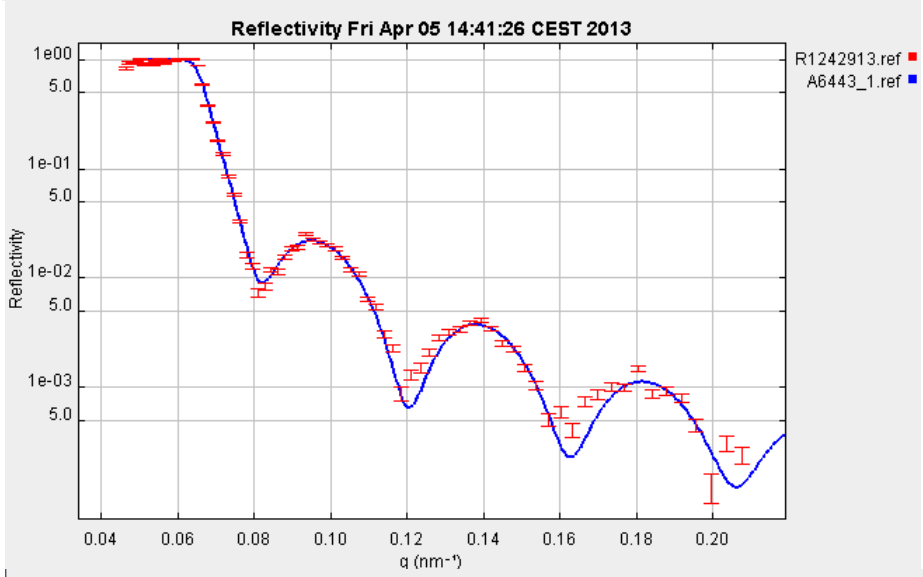

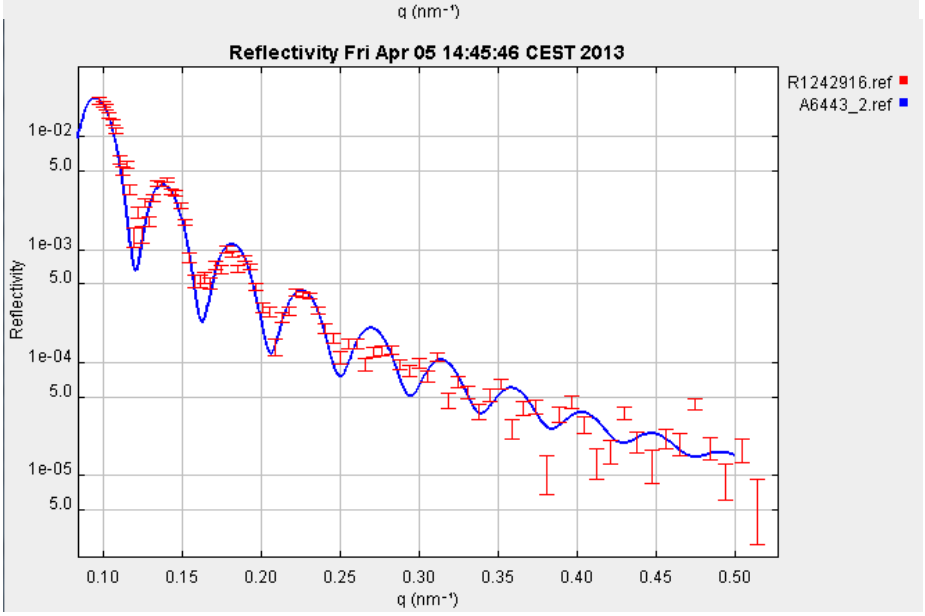

Model 3b

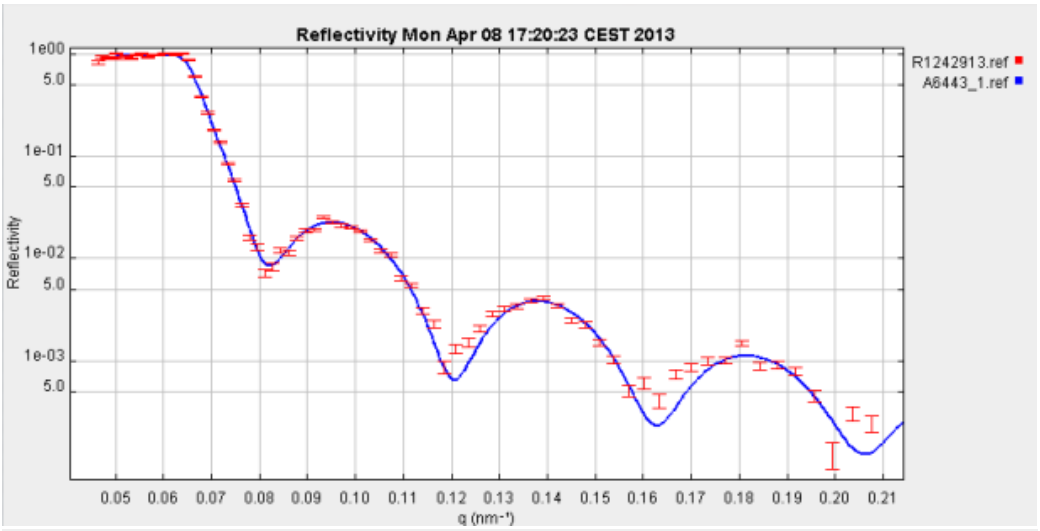

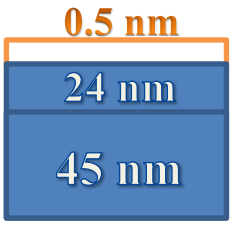

χ^2 = 1.24

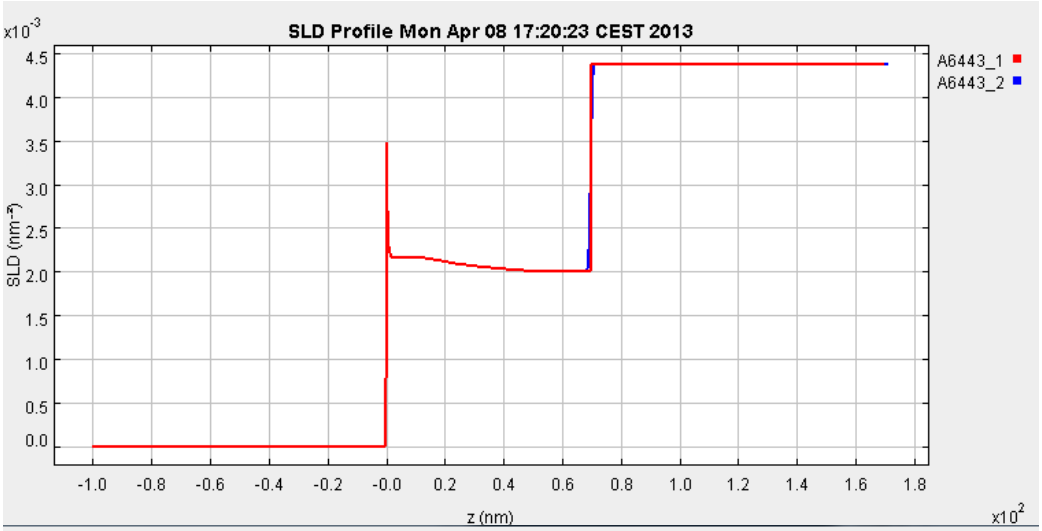

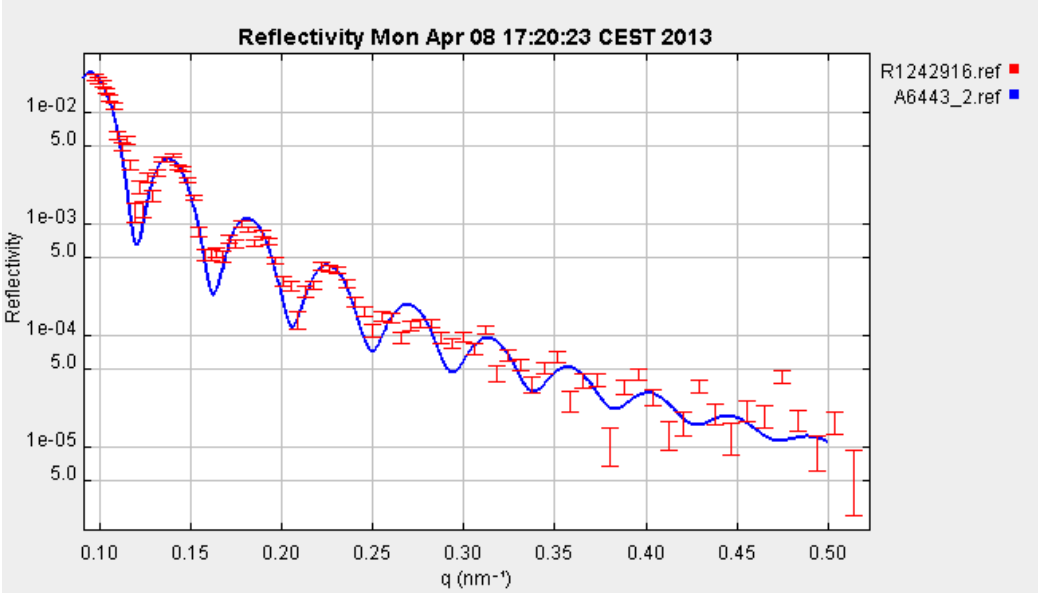

Model 3c

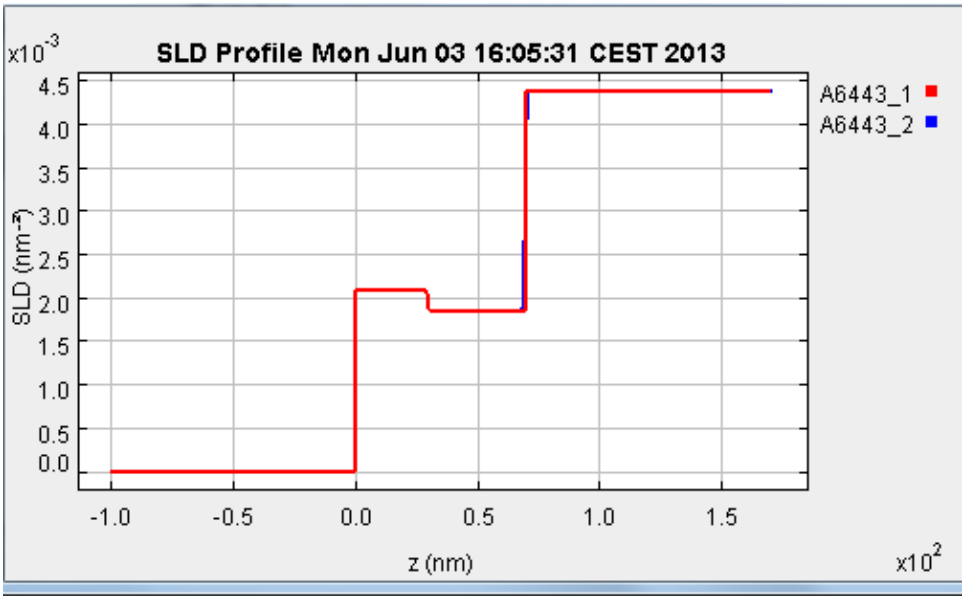

29 nm

41 nm

χ^2 = 1.22

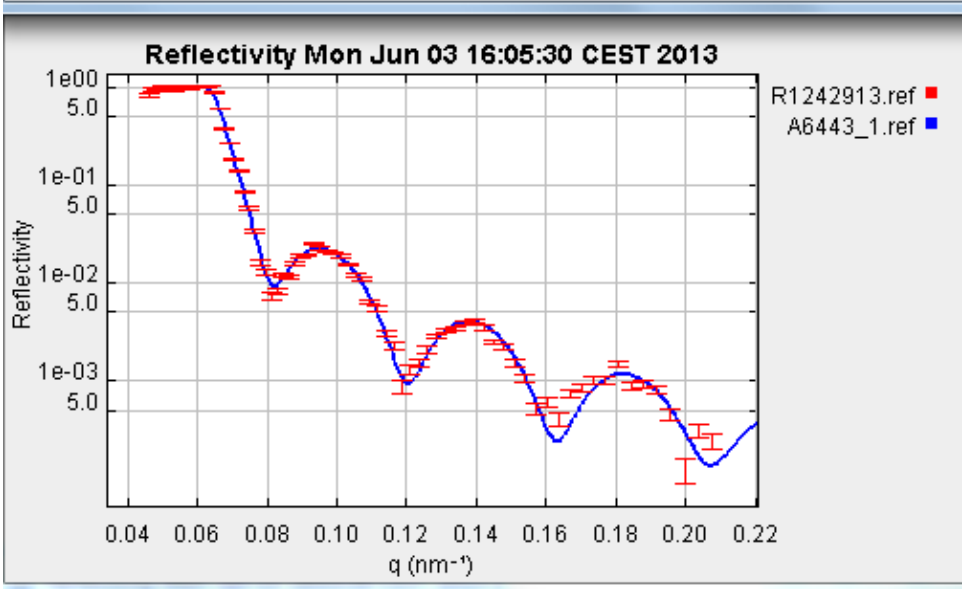

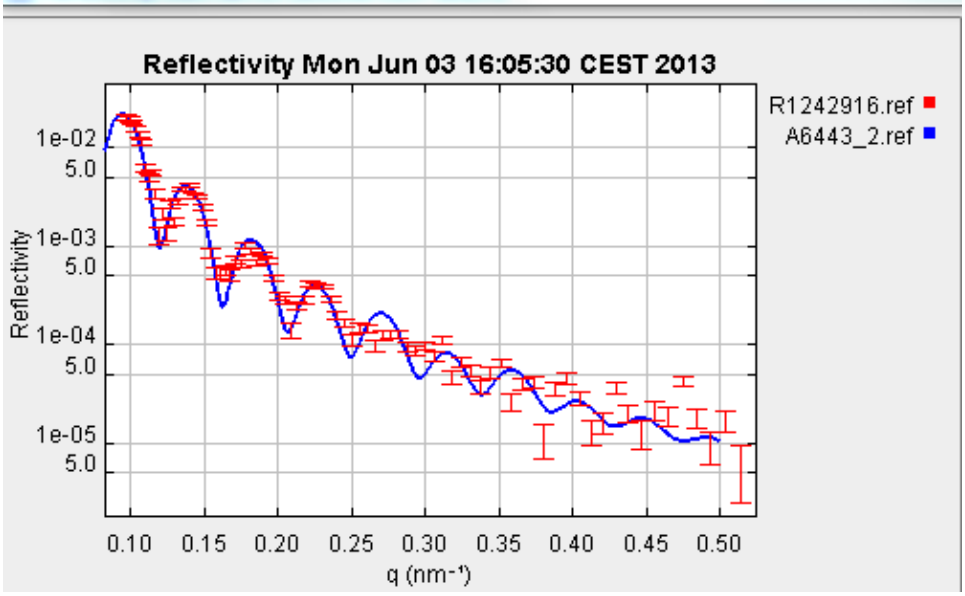

Model 3d

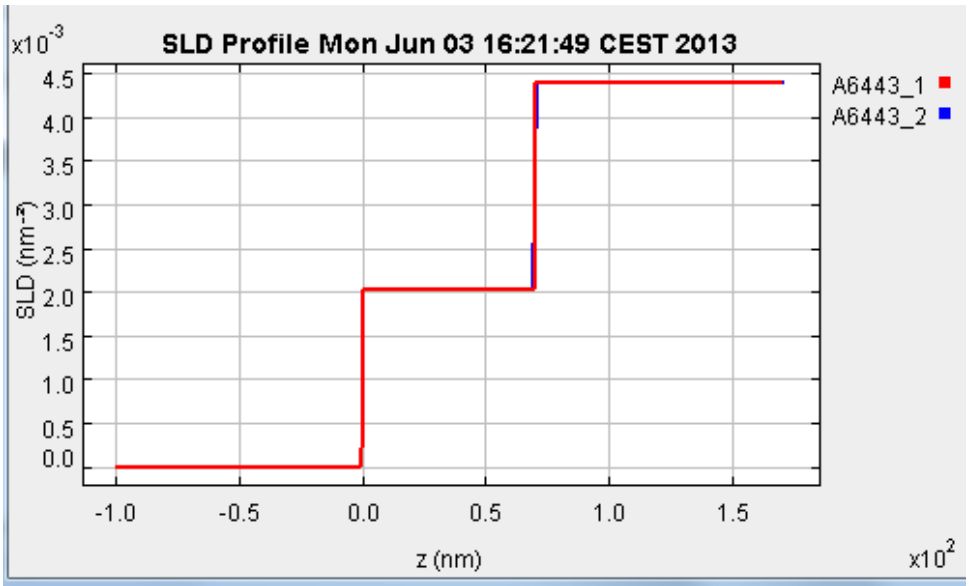

70 nm

χ^2 = 1.29

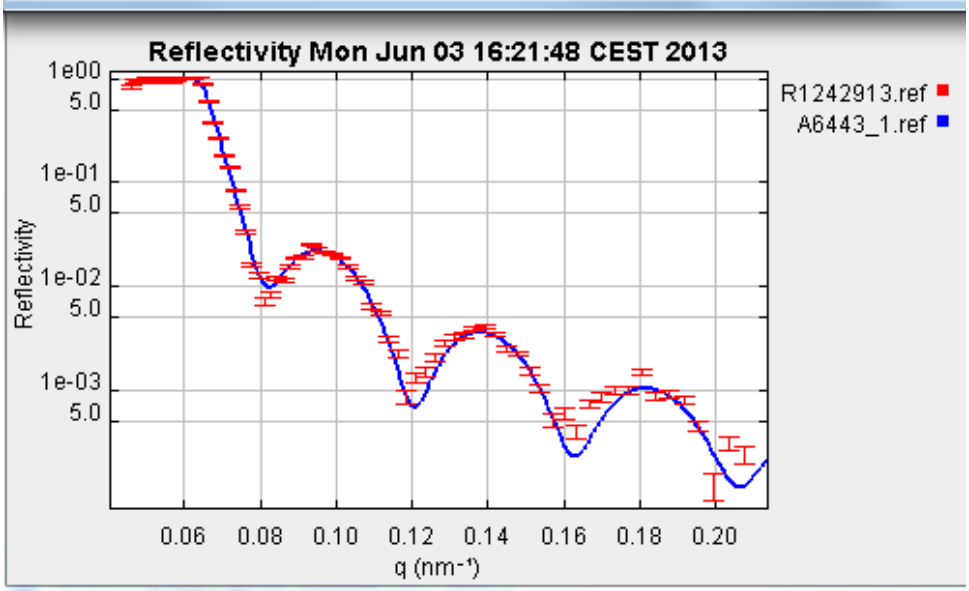

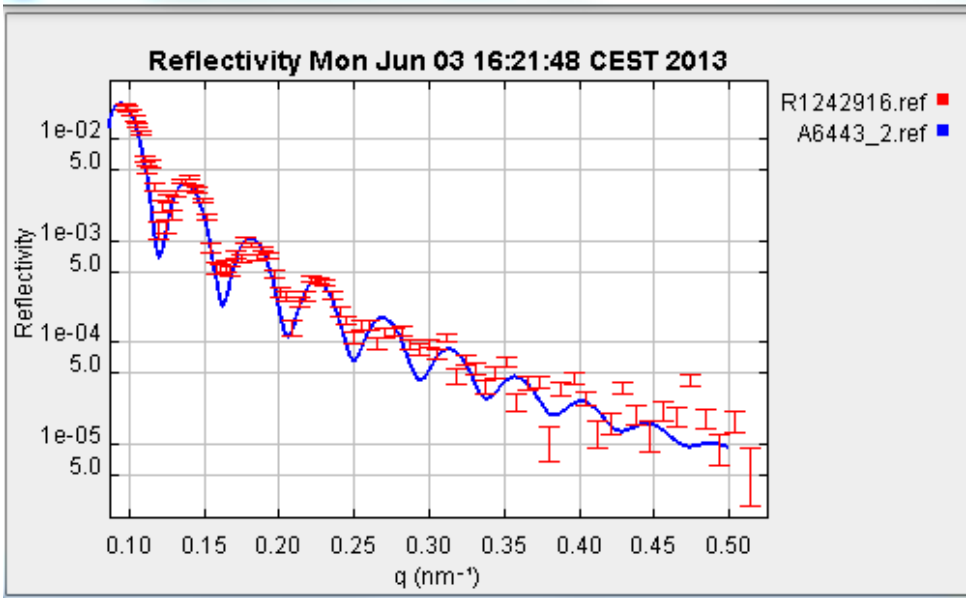

R=250

Model 4a

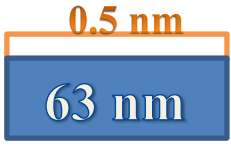

χ^2 = 1.69

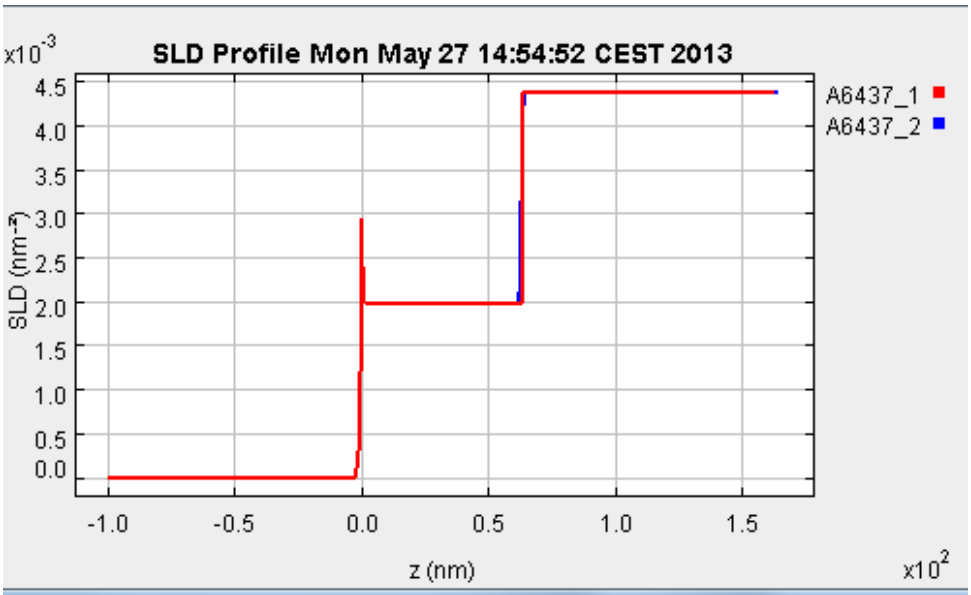

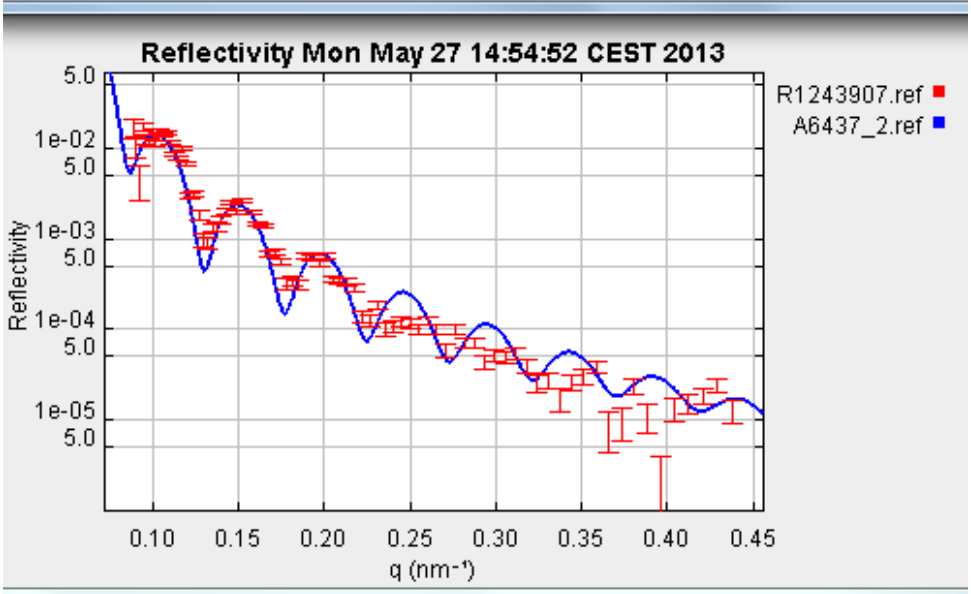

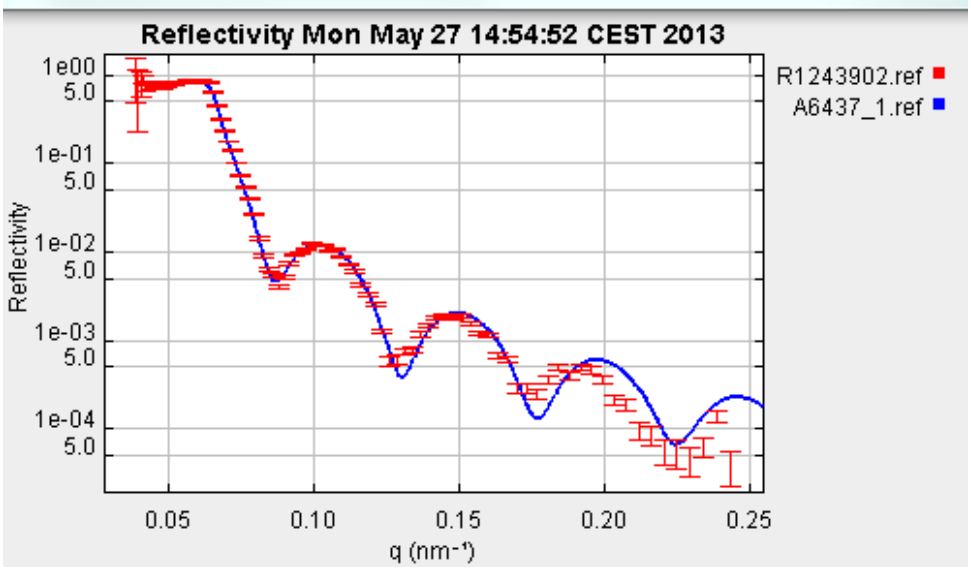

Model 4b

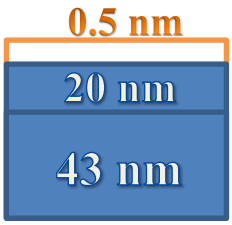

χ^2 = 1.67

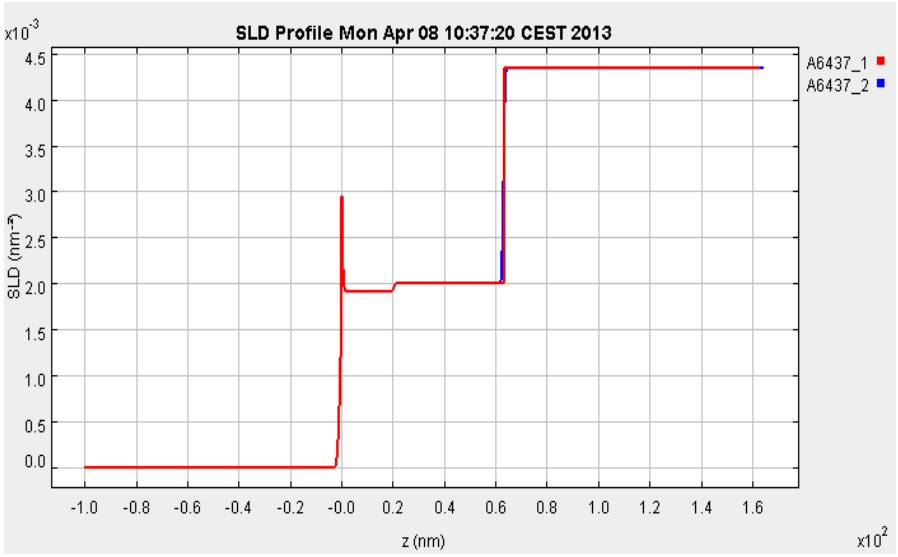

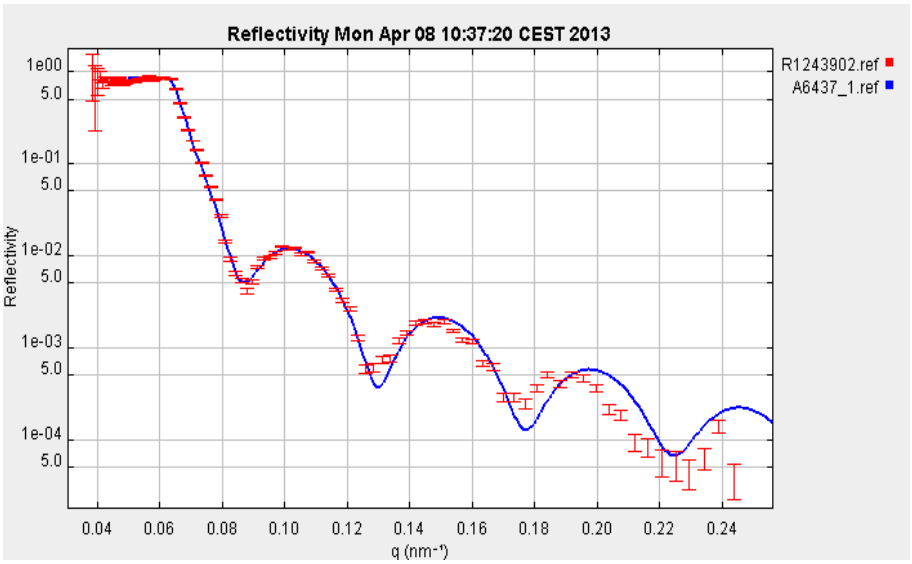

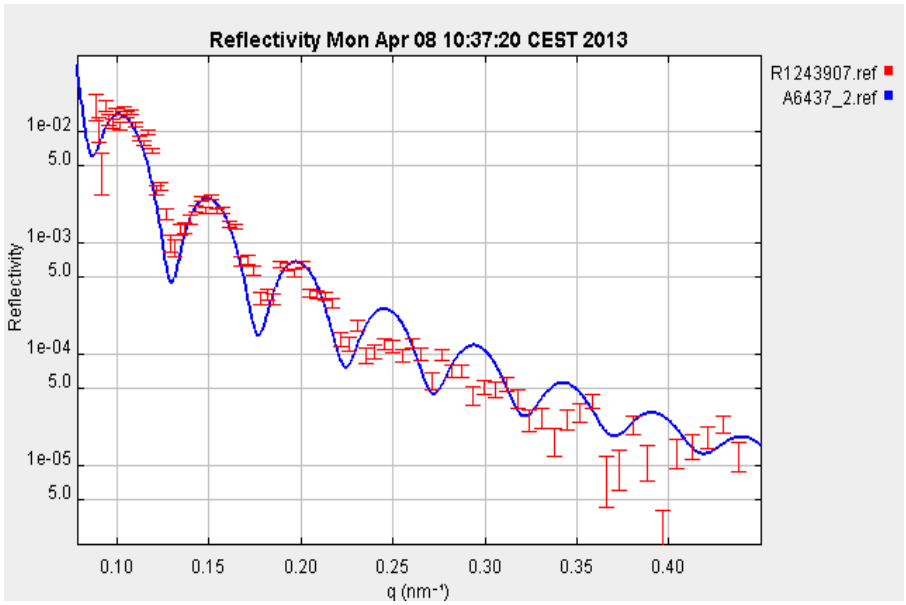

Model 4c

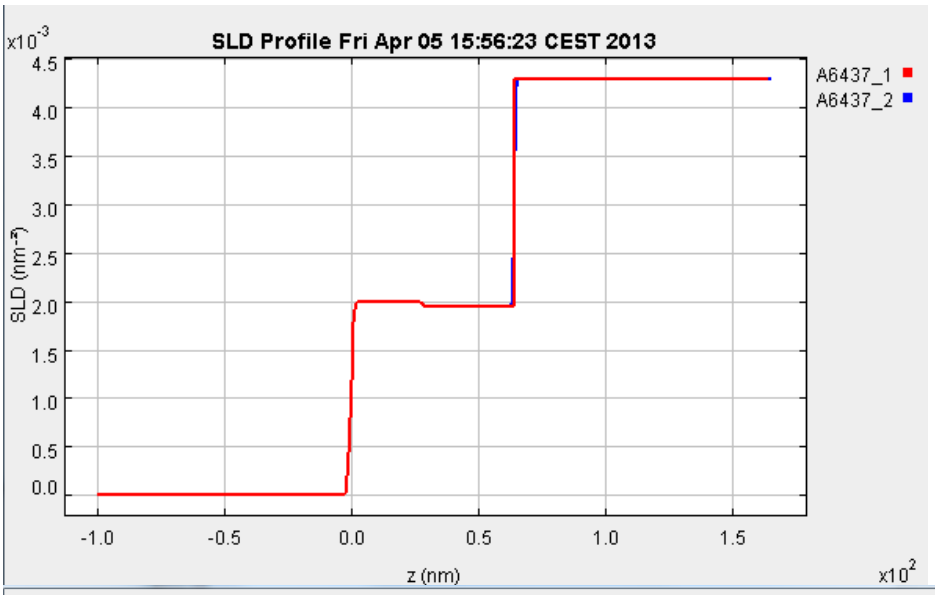

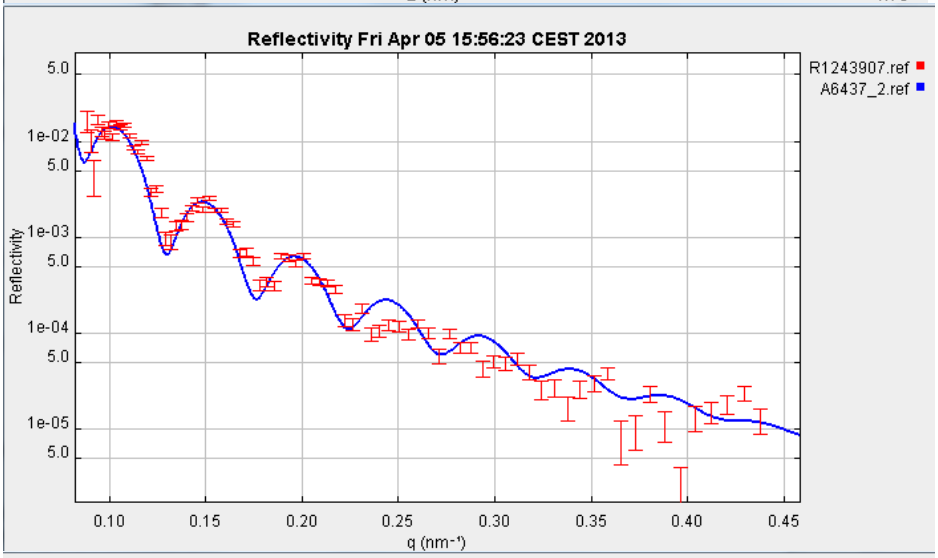

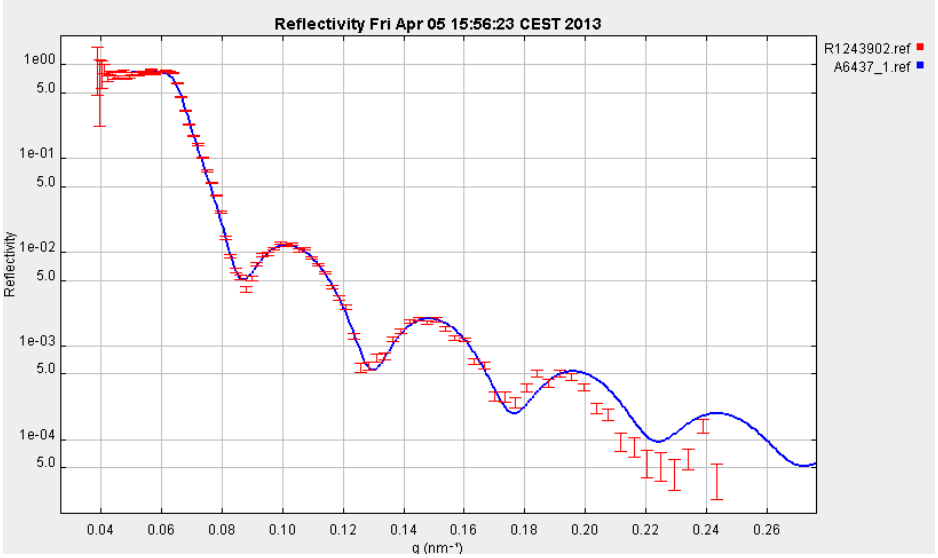

28 nm

36 nm

χ^2 = 1.43

Model 4d

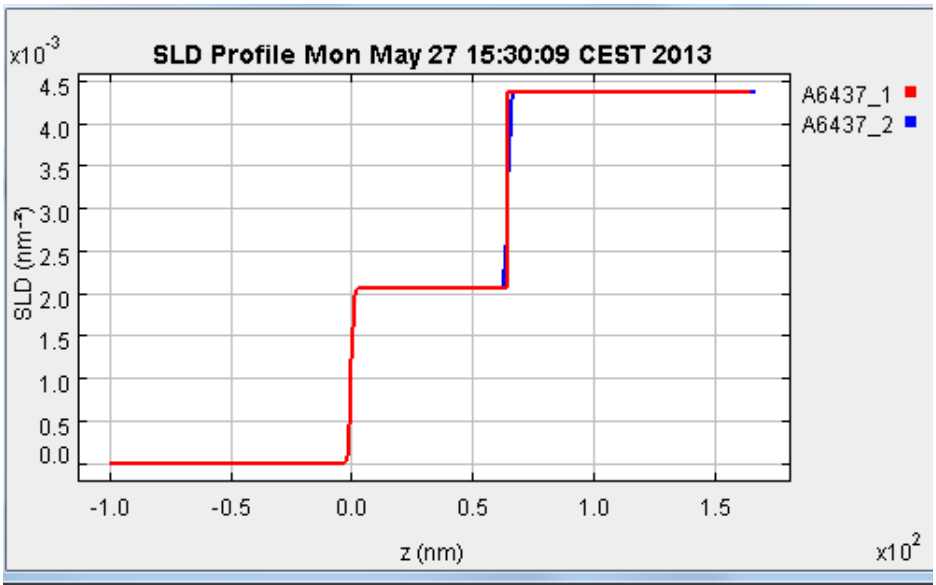

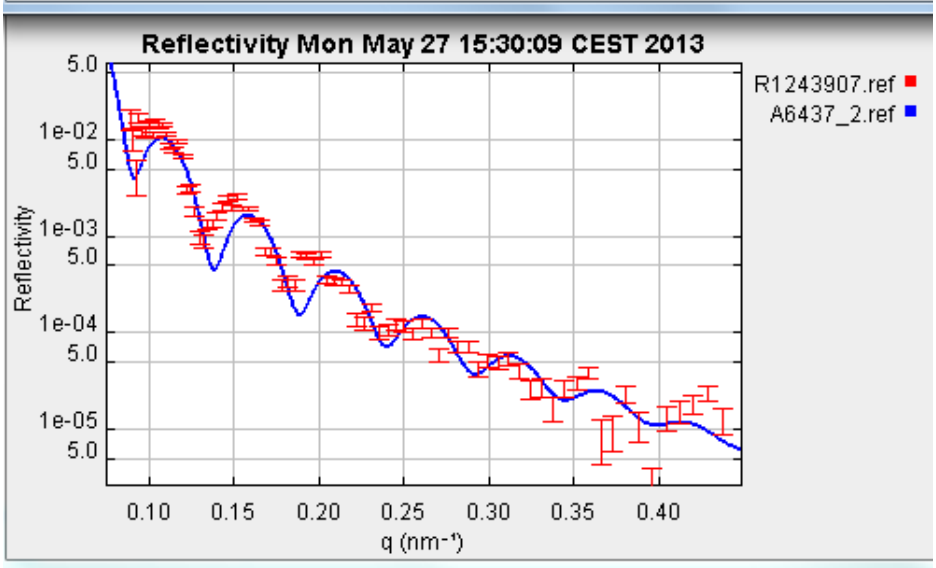

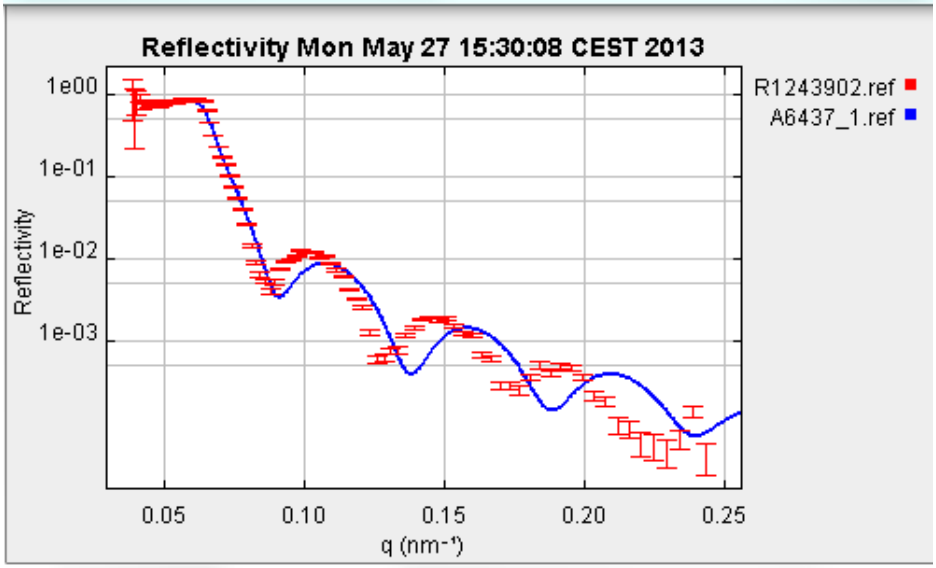

65 nm

χ^2 = 1.43

Appendix 4: Raman

A4-1 Spectra after annealing to 300°C

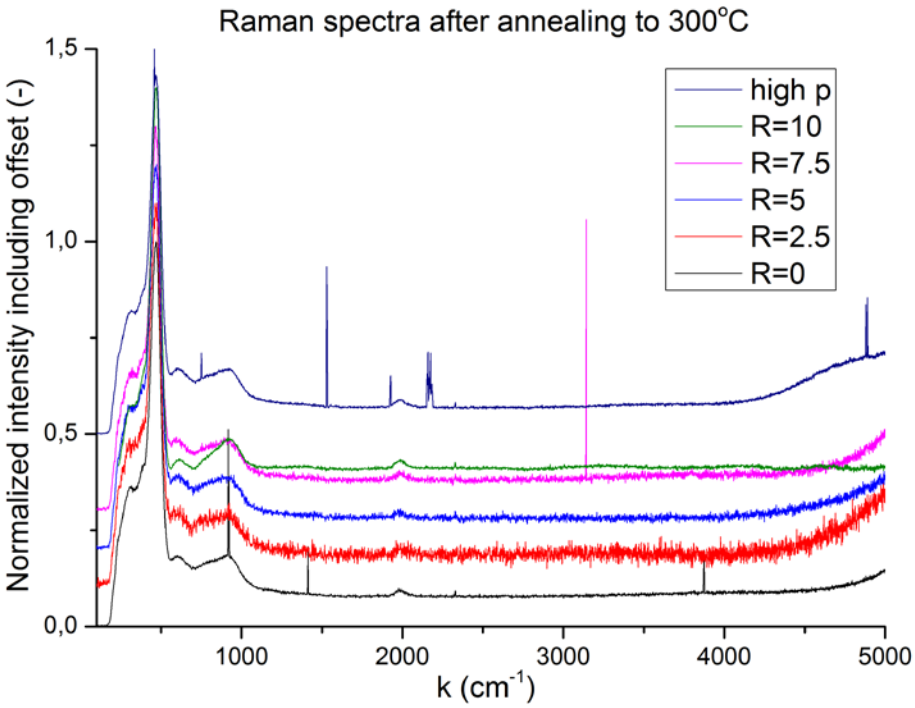

Figure A4-1. Raman spectra for samples R=0 up to R=10 and the high pressure sample. All samples have undergone an annealing treatment up to T=300°C.

References

[1] Ginley, David, Martin A. Green, and Reuben Collins. "Solar energy conversion toward 1 terawatt." *Mrs Bulletin* 33.04 (2008): 355-364.

[2] Hakvoort, Rudi Albert. "Applications of positron depth profiling." (1993).

[3] Street, Robert A. *Hydrogenated amorphous silicon*. Cambridge University Press, 2005.

[4] Poortmans, Jef, and Vladimir Arkhipov, eds. *Thin film solar cells: fabrication, characterization and applications*. Vol. 5. John Wiley & Sons, 2006. H5 Advanced Amorphous Silicon Solar Cell Technologies by Zeman, M.

[5] Kolodziej, A. "Staebler-Wronski effect in amorphous silicon and its alloys." *Opto-electronics review* 12.1 (2004): 21-32.

[6] Staebler, D. L., and C. R. Wronski. "Reversible conductivity changes in discharge-produced amorphous Si." *Applied Physics Letters* 31 (1977): 292.

[7] Stutzmann, M., W. B. Jackson, and C. C. Tsai. "Light-induced metastable defects in hydrogenated amorphous silicon: A systematic study." *Physical Review B* 32.1 (1985): 23.

[8] Branz, Howard M. "Hydrogen collision model: Quantitative description of metastability in amorphous silicon." *Physical Review B* 59.8 (1999): 5498.

[9] Powell, M. J., and S. C. Deane. "Defect-pool model and the hydrogen density of states in hydrogenated amorphous silicon." *Physical Review B* 53.15 (1996): 10121.

[10] Fritzsche, Hellmut. "Development in understanding and controlling the Staebler-Wronski effect in a-Si: H." *Annual Review of Materials Research* 31.1 (2001): 47-79.

[11] David Cohen, J., and Daewon Kwon. "Identification of the dominant electron deep trap in amorphous silicon from ESR and modulated photocurrent measurements: implications for defect models." *Journal of non-crystalline solids* 227 (1998): 348-352.

[12] Polk, D. E. "Structural model for amorphous silicon and germanium." *Journal of Non-Crystalline Solids* 5.5 (1971): 365-376.

[13] Smets, A. H. M., W. M. M. Kessels, and M. C. M. Van de Sanden. "Vacancies and voids in hydrogenated amorphous silicon." *Applied physics letters* 82.10 (2003): 1547-1549.

[14] Zafar, Sufi, and E. A. Schiff. "Hydrogen-mediated model for defect metastability in hydrogenated amorphous silicon." *Physical Review B* 40.7 (1989): 5235.

[15] Zhang, S. B., and Howard M. Branz. "Hydrogen above saturation at silicon vacancies: H-pair reservoirs and metastability sites." *Physical Review Letters* 87.10 (2001): 105503.

[16] Melskens, Jimmy, et al. "New Insights in the Nanostructure and Defect States of Hydrogenated Amorphous Silicon Obtained by Annealing." *IEEE J. of Photovoltaics* 3, 65-71 (2013).

[17] Smets, A. H. M., et al. "The hydride stretching modes of hydrogenated vacancies in amorphous and nanocrystalline silicon: A helpful tool for material characterization." *Photovoltaic Specialists Conference (PVSC), 2009 34th IEEE*. IEEE, 2009.

[18] Smets, Arno HM. "The Staebler-Wronski effect: new physical approaches and insights as a route to reveal its origin." *Proc. Mater. Res. Soc. Symp*. Vol. 1245. 2010.

[19] Beyer, W. "Diffusion and evolution of hydrogen in hydrogenated amorphous and microcrystalline silicon." *Solar energy materials and solar cells* 78.1 (2003): 235-267.

[20] Wikipedia "Theory of solar cells". http://en.wikipedia.org/wiki/ Theory_of_solar_cells. Retrieved 18th of June, 2013.

[21] http://www.ni.com/white-paper/7230/en/. Retrieved 18th of June, 2013.

[22] http://www.thenakedscientists.com/HTML/articles/article/catching-energy-from-the-sun/ Retrieved 2th of July 2013.

[23] http://en.wikipedia.org/wiki/Shockley%E2%80%93Queisser_limit. Retrieved 2th of July 2013.

[24] Shockley, William, and Hans J. Queisser. "Detailed balance limit of efficiency of p-n junction solar cells." *Journal of applied physics* 32.3 (1961): 510-519.

[25] Schut, H. “A variable energy positron beam facility with applications in materials science.” (1990). PhD-thesis.

[26] Valkealahti, S., and R. M. Nieminen. "Monte Carlo calculations of keV electron and positron slowing down in solids. II." Applied Physics A 35.1 (1984): 51-59.

[27] Melskens, J. et al. “A systematic annealing study of the nanostructure and defect states of various types of intrinsic hydrogenated amorphous silicon.” MRS poster, spring 2013.

[28] Hautojärvi, P., et al. "The effect of microvoid size on positron annihilation characteristics and residual resistivity in metals." *Philosophical magazine* 35.4 (1977): 973-981.

[29] Kruseman, Abraham Cornelis. "Two-dimensional ACAR and low-background DBAR studies on materials with defects." (1999).

[30] Krause-Rehberg, Reinhard, and Hartmut S. Leipner. *Positron annihilation in semiconductors: defect studies*. Vol. 127. Springer, 1999.

[31] Szpala, S., et al. "Defect identification using the core-electron contribution in Doppler-broadening spectroscopy of positron-annihilation radiation." *Physical Review, B: Condensed Matter* 54.7 (1996).

[32] He, Y. J., et al. "Positron-annihilation study of voids in a-Si and a-Si: H." *Physical Review B* 33.8 (1986): 5924.

[33] Ho, King-fung. *Some Positron Annihilation Studies on Highly Doped and Supersaturated N-type Silicon*. Diss. University of Hong Kong, 2005.

[34] Beling, C. D., et al. "On the possible identification of defects using the autocorrelation function approach in double Doppler broadening of annihilation radiation spectroscopy." *Journal of Physics: Condensed Matter* 10.46 (1998): 10475.

[35] Ho, K. F., et al. "Positron–electron autocorrelation function study of E-center in silicon." *Journal of applied physics* 94.9 (2003): 5549-5555.

[36] Kobayasi, T. "Coupling of Positron Annihilation and Compton Scattering: A Theoretical Possibility to Analyze Positron Distribution Through Atom-like Local Patterns Appearing in Positron Annihilation A (r)-and Compton Scattering B (r)-Functions." *Materials Science Forum*. Vol. 363. 2001.

[37] Van Well, A. A., V-O. De Haan, and H. Fredrikze. "ROG, the new neutron reflectometer at IRI, Delft." *Physica B: Condensed Matter* 198.1 (1994): 217-219.

[38] *Neutron data booklet*. Philadelphia: Old City, 2003.

[39] Ricciardi, Paola. *Raman spectroscopy for the non-destructive characterization of ancient pottery, porcelain and mosaic glass*. Diss. Università degli studi di Firenze, 2008.

[40] http://www.timkelf.com/Research/ResearchSERS.html. Picture retrieved 3rd of July, 2013.

[41] van Schaarenburg, L. “Positron Analysis on Solar Cell Nanocrystals” MSc-thesis, 2009.

[42] http://psd11.tnw.tudelft.nl/positrons.html. Retrieved 15th of June, 2013.

[43] http://www.renishaw.com/en/new-raman-spectroscopy-agent-for-romania--14407. Picture retrieved 3rd of July, 2013.

[44] Vullers, A. “Thin film solar cell materials studied with X-ray diffraction and positron annihilation.” (august 2012). BSc-report.

[45] Eijt, S. W. H., et al. "Positron annihilation depth-profiling as a promising tool for the structural analysis of light-soaked a-Si: H absorber layers." *physica status solidi (c)* 7.3-4 (2010): 632-635.

[46] Zeman, Miro, et al. "Structural properties of amorphous silicon prepared from hydrogen-diluted silane." *Philosophical Magazine* 89.28-30 (2009): 2435-2448.

[47] Smets, A.H.M. Review paper, to be published.

[48] Melskens, J., et al. "The nanostructural analysis of hydrogenated silicon films based on positron annihilation studies." *Journal of Non-Crystalline Solids* 358.17 (2012): 2015-2018.

[49] Dannefaer, S., and D. Kerr. "Oxygen in silicon: A positron annihilation investigation." *Journal of applied physics* 60.4 (1986): 1313-1321.

[50] Britton, D. T., et al. "Local structure reconstruction in hydrogenated amorphous silicon from angular correlation and synchrotron diffraction studies." *Applied surface science* 252.9 (2006): 3194-3200.

[51] Fedders, P. A., et al. "Molecular hydrogen in a-Si: H." *Physical review letters* 85.2 (2000): 401.

[52] Kawata, M., et al. "Characterization of stress in doped and undoped polycrystalline silicon before and after annealing or oxidation with laser raman spectroscopy." *Journal of electronic materials* 19.5 (1990): 407-411.

[53] Smets, A. H. M., et al. "The hydride stretching modes of hydrogenated vacancies in amorphous and nanocrystalline silicon: A helpful tool for material characterization." *Photovoltaic Specialists Conference (PVSC), 2009 34th IEEE*. IEEE, 2009.

[54] De Wolf, Ingrid. "Micro-Raman spectroscopy to study local mechanical stress in silicon integrated circuits." *Semiconductor Science and Technology* 11.2 (1996): 139.